

Probing the Corona in Active Galactic Nuclei Using Broadband X-ray Spectroscopy

Thesis by
Nikita Kamraj

In Partial Fulfillment of the Requirements for the
Degree of
Doctor of Philosophy

The logo for the California Institute of Technology (Caltech), featuring the word "Caltech" in a bold, orange, sans-serif font.

CALIFORNIA INSTITUTE OF TECHNOLOGY
Pasadena, California

2022
Defended 16 September 2021

© 2022

Nikita Kamraj

ORCID: 0000-0002-3233-2451

All rights reserved

ACKNOWLEDGEMENTS

First and foremost, I would like to thank my Ph. D. advisor Prof. Fiona Harrison for all her support throughout graduate school. Fiona truly went above and beyond to ensure that I could complete my graduate studies safely and successfully. She is an amazing human being, both professionally and personally. I am grateful to have had the opportunity to work under her guidance and greatly appreciate her efforts to help me through very difficult personal circumstances during the COVID-19 pandemic.

I am grateful to my parents for being supportive of my academic interests and encouraging my interest in Astronomy from a young age. I am humbled by all the sacrifices they made so that I could achieve my goals. I would like to thank my mother in particular for her unwavering dedication, determination and commitment in raising me, for always being there for me no matter how alone I was, and striving to create the best life for me.

I would like to thank the *NuSTAR* team at Caltech for all their help and input into my research work, from technical troubleshooting to insightful discussions and feedback on my research papers. I extend special thanks to Dr. Murray Brightman, Dr. Mislav Baloković, and Dr. Daniel Stern for their mentorship and guidance throughout my Ph. D. I also thank Prof. Evan Kirby for serving as chair of my thesis committee and checking in on me during my final year of my Ph. D.

Lastly, I thank Austin, all my friends, and staff at Caltech who have helped me through very tumultuous times and have been a great support network for me, particularly during the lock-downs of the COVID-19 pandemic. They have taught me that family is not forged from blood but from people that care and look out for you. I also extend my gratitude to the Astronomy graduate student community at Caltech for being a cohesive, fun, and welcoming group of people that have enriched my graduate school experience. I have crossed paths with many incredible people and created lifelong connections during my time at Caltech, for which I am forever grateful.

ABSTRACT

Active Galactic Nuclei (AGN) are some of the most luminous sources in our known universe, powered by large-scale accretion onto a supermassive black hole. Supermassive black holes are known to co-evolve with their host galaxies, with AGN playing an important role in regulating feedback in galaxies by depositing large amounts of energy through outflows and jets. While studies of AGN have dated back to the 1960's when the first quasar was discovered, much is still unknown about the key source powering the X-ray emission in AGN, i.e. the corona. In my thesis, I present detailed investigations of the properties of AGN coronae using broadband X-ray spectroscopic techniques. This work utilizes spectroscopic data taken with the *NuSTAR* telescope, which has revolutionized studies of the corona. Being the first focusing high energy X-ray telescope in orbit, *NuSTAR*'s high sensitivity at hard X-ray energies (> 10 keV) has enabled robust measurements of fundamental properties of the corona, such as its temperature, from single epoch observations of AGN for the first time. In the first study presented in this thesis, I performed measurements of coronal temperature in a sample of 46 *NuSTAR*-observed AGN through fitting X-ray spectral models for each object. My analysis showed the temperature of the corona to be regulated by electron-positron pair production and annihilation processes. From this sample, I identified an AGN with an unusually low coronal temperature, 2MASX J19301380+3410495. I modeled the broadband X-ray spectrum of this object in detail using multi-epoch X-ray observations taken with the *Swift*, *XMM-Newton*, and *NuSTAR* telescopes, and found the object to also belong to a rare class of X-ray obscured but optically unobscured AGN. Using multi-wavelength information, I elucidated the nature of the complex obscuration present in 2MASX J19301380+3410495. In recent work presented in this thesis, I compiled one of the largest samples of unobscured AGN with high quality *NuSTAR* X-ray spectra in order to characterize how the physical properties of the corona relate to fundamental accretion parameters in AGN, such as the Eddington ratio and mass of the supermassive black hole. Finally, I discuss possible future work directed at investigating other enigmatic AGN similar to 2MASX J19301380+3410495 that have conflicting optical and X-ray classifications. Using techniques such as multi-wavelength spectropolarimetry in addition to X-ray spectroscopy, it may be possible to unveil the mechanisms of obscuration within these exotic sources that challenge classical pictures of AGN structure.

PUBLISHED CONTENT AND CONTRIBUTIONS

N. Kamraj, F. A. Harrison, M. Brightman, M. Baloković, C. Ricci, D. Stern, J. A. García, Michael J. Koss, J. E. Mejía-Restrepo, Kyuseok Oh, M. C. Powell, and C. M. Urry. X-ray Coronal Properties of *Swift*/BAT-Selected Seyfert 1 Active Galactic Nuclei. *The Astrophysical Journal*, accepted.

N. K. participated in the conception of the project, analyzed all X-ray data, and wrote the manuscript.

N. Kamraj, F. A. Harrison, M. Baloković, A. Lohfink, and M. Brightman. Coronal Properties of *Swift*/BAT-Selected Seyfert 1 AGNs Observed with NuSTAR. *The Astrophysical Journal*, 866:124, 2018. doi: 10.3847/1538-4357/aadd0d.

N. K. participated in the conception of the project, analyzed all X-ray data, and wrote the manuscript.

N. Kamraj, M. Baloković, M. Brightman, D. Stern, F. A. Harrison, R. J. Assef, M. J. Koss, K. Oh, and D. J. Walton. The Broadband X-Ray Spectrum of the X-Ray-obscured Type 1 AGN 2MASX J193013.80+341049.5. *The Astrophysical Journal*, 887(2):255, 2019a. doi: 10.3847/1538-4357/ab57fc.

N. K. participated in the conception of the project, analyzed all X-ray data, and wrote the manuscript.

N. Kamraj, A. Fabian, A. Lohfink, M. Baloković, C. Ricci, and K. Madsen. Probing the Physical Properties of the Corona in Accreting Black Holes. *Bulletins of the American Astronomical Society*, 51(3):126, 2019b.

N. K. led the conception of the white paper, and participated in the writing of the manuscript.

TABLE OF CONTENTS

Acknowledgements	iii
Abstract	iv
Published Content and Contributions	v
Table of Contents	v
List of Illustrations	viii
List of Tables	xiv
Chapter I: Introduction	1
1.1 A Brief History of Active Galactic Nuclei (AGN)	1
1.2 The Classical Unified Model of AGN	2
1.3 Modern Picture of the Anatomy of an AGN	5
1.4 The Nature of the Corona in AGN	8
1.5 Broadband X-ray Spectral Modeling as a Tool to Study AGN	10
1.6 Outline of this Thesis Work	13
Chapter II: Coronal Properties of Swift/BAT-selected Seyfert 1 AGN Observed with NuSTAR	16
2.1 Introduction	17
2.2 Sample, Data Reduction, and Analysis	19
2.3 Results and Discussion	24
2.4 Future Observations	29
2.5 Summary	31
2.6 Acknowledgements	32
2.7 Appendix	32
Chapter III: The Broadband X-Ray Spectrum of the X-Ray-obscured Type 1 AGN 2MASX J193013.80+341049.5	35
3.1 Introduction	36
3.2 X-ray Observations and Data Reduction	38
3.3 X-ray Spectral Modeling	39
3.4 Multi-wavelength Analysis	46
3.5 Summary	54
3.6 Acknowledgements	55
Chapter IV: X-ray Coronal Properties of <i>Swift</i> /BAT-Selected Seyfert 1 Active Galactic Nuclei	57
4.1 Introduction	58
4.2 Sample, Observations, and Data Reduction	60
4.3 X-ray Spectral Modeling	62
4.4 Results and Discussion	65
4.5 Summary	80
4.6 Acknowledgments	81
Chapter V: Future Studies	83

5.1	Studies of X-ray Obscured Type 1 AGN in the <i>Swift</i> /BAT Survey . .	83
5.2	Spectropolarimetry of X-ray Obscured Type 1 AGN	84
5.3	Future X-ray Missions and Prospects for Studies of AGN Coronae . .	87
Chapter VI: Summary and Conclusions		91
Bibliography		93

LIST OF ILLUSTRATIONS

<i>Number</i>	<i>Page</i>
1.1 Illustration of the basic components of an AGN under the classical unified paradigm. Figure taken from Urry & Padovani (1995).	4
1.2 Illustration depicting a modern representation of the key structures comprising an AGN, as viewed along the equatorial and polar directions. Figure taken from Ramos Almeida & Ricci (2017). Different colored clumps correspond to different compositions/structures; green and blue shaded regions mark the inner and outer ionization cones.	7
1.3 Schematic diagram describing radiation-regulated feedback, where λ_{Edd} refers to the Eddington ratio. Shaded grey regions correspond to different ranges of obscuring column density N_{H} . Figure taken from Ricci et al. (2017a).	7
1.4 Plot of the $l - \theta$ plane, showing boundaries for runaway pair production, electron-electron coupling, electron-proton coupling, and the line where Compton cooling dominates over Bremsstrahlung cooling ($t_B = t_C$). The solid red and blue lines correspond to pair lines for a slab corona and isolated cloud corona, respectively. Figure taken from Fabian et al. (2015).	9
1.5 An example X-ray spectrum of a Type 1 AGN from Risaliti & Elvis (2004), showing the main reflection features such as the 6.4 keV Fe $K\alpha$ line and CRH. Also shown in magenta is absorption at soft (< 10 keV) energies by warm gas and ‘soft excess’ emission that is possibly attributed to line blending or thermal emission of a warm plasma with $kT \sim 0.1 - 1$ keV.	11
2.1 Redshift-luminosity distribution for <i>NuSTAR</i> -observed Sy1 AGN selected from the <i>Swift</i> /BAT 70-month hard X-ray catalogue.	20
2.2 Distributions of redshifts, <i>Swift</i> /BAT 70-month X-ray catalogue luminosities and fluxes for both our sample and the Sy1 classified sources from the <i>Swift</i> /BAT catalogue. For clarity, sources with $L_{\text{BAT}} < 10^{40}$ erg s^{-1} and $F_{\text{BAT}} > 1 \times 10^{-10}$ erg $\text{s}^{-1} \text{cm}^{-2}$ were omitted from the plots. 21	21

2.3	<p><i>NuSTAR</i> hard X-ray spectrum of a candidate low cutoff AGN 2MASX J19301380+3410495 (a), alongside fit residuals for (b) an absorbed power-law model ($\chi^2/\text{dof} = 155.1/161$), (c) absorbed power-law model with a high-energy cutoff ($\chi^2/\text{dof} = 144.4/160$), and (d) absorbed cutoff power-law with reflection modeled via <i>pexrav</i> ($\chi^2/\text{dof} = 138/160$). Black points correspond to FPMA data while points in red correspond to FPMB.</p>	23
2.4	<p>Distribution of lower limits on E_{cut} for our Sy1 AGN sample from modeling <i>NuSTAR</i> data.</p>	24
2.5	<p>E_{cut} vs photon index Γ for our sample. Points in red denote candidate sources with low coronal high-energy cutoffs for which both upper and lower limits on E_{cut} were measured. The purple line corresponds to theoretical constraints from Petrucci et al. (2001) for $\tau = 6$.</p>	26
2.6	<p>$E_{\text{cut}}-\Gamma$ contour plots for <i>NuSTAR</i> observations of the candidate low cutoff Sy1s (a) 2MASX J19301380+3410495 (b) 1RXS J034704.9-302409. The solid purple, green, and yellow contours correspond to the 68, 90, and 99 % confidence levels, respectively. The black cross represents the best fit values of the parameters from applying the relevant model given in Table 2.3.</p>	27
2.7	<p>The $\theta - l$ plane for <i>NuSTAR</i>-observed Sy1 AGN. Solid lines correspond to pair lines for different coronal geometries. Circled points are candidate low cutoff sources for which both upper and lower limits on E_{cut} were measured. Triangles denote sources with a best-fit value and lower limit on E_{cut}. Squares denote sources with only lower limits on E_{cut}. Blue points indicate sources for which the black hole mass was taken to be the median black hole mass of the type 1 AGN in the BAT AGN Spectroscopic Survey (BASS) (Koss et al., 2017).</p>	28
2.8	<p>Distributions of E_{cut} values for 5000 simulations of the <i>NuSTAR</i> spectrum of a candidate low cutoff AGN, 2MASX J19301380+3410495. Dotted lines denote the input E_{cut} value assumed for simulated spectra. Simulations were performed for exposure times of (a) 50 ks and (b) 100 ks.</p>	31

3.1	<i>NuSTAR</i> light curves of 2MASX J193013.80+341049.5 in the 3–50 keV band, where (a) is the light curve of the ~ 20 ks observation taken in 2016 and (b) the deeper ~ 50 ks observation taken in 2017. Gaps in data are due to Earth occultation events. There is no evidence for strong X-ray variability in this source.	40
3.2	Broadband X-ray spectrum of 2MASX J19301380+3410495 (a), alongside fit residuals for (b) an absorbed cutoff power law model ($\chi^2/\text{dof} = 1409/811$), (c) absorbed cutoff power law with an Fe $K\alpha$ line, scattered power law, and a reflection component incorporated using the <i>pexrav</i> model ($\chi^2/\text{dof} = 826/798$), (d) absorbed cutoff power law with a variable iron abundance absorber and reflection modeled with <i>pexmon</i> ($\chi^2/\text{dof} = 816/798$), and (e) <i>borus</i> model ($\chi^2/\text{dof} = 808/795$).	42
3.3	Broadband X-ray spectrum of 2MASX J193013.80+341049.5 unfolded through the <i>borus02</i> model (Model 3). Solid lines represent total model while dashed lines depict individual model components.	46
3.4	$E_{\text{cut}}-\Gamma$ contour plot from the <i>borus02</i> model fit (Model 3) to broadband X-ray data of 2MASX J193013.80+341049.5. The solid purple, green, and yellow contours correspond to the 68, 90, and 99 % confidence levels, respectively. The black cross represents the best-fit values of the parameters from applying the <i>borus02</i> model.	47
3.5	Optical spectra of 2MASX J193013.80+341049.5 taken at Orzale (2006), KPNO (2007), and Palomar Observatory (2016, 2018, 2019). The fluxes have been normalized by the emission in a line-free region (4760 - 4780 Å). Left and right panels show the velocity centered on the $H\beta$ and $H\alpha$ line profiles, respectively.	49
3.6	Rest-frame 2–10 keV X-ray luminosity against rest-frame 6 μm mid-infrared luminosity for 2MASX J193013.80+341049.5 (black point) along with published relations from Fiore et al. (2009) and Stern (2015).	50
3.7	Spectral energy distribution (SED) of 2MASX J193013.80+341049.5. The best-fit SED model (black line) consists of an AGN component (blue line), a young stellar population (cyan line), and an old stellar population (red line). Solid red points are observed flux densities used for the SED fit, obtained from publicly available data from the <i>Vizier</i> catalog and PanSTARRS DR2.	52

3.8	Rest-frame monochromatic 2 keV luminosity $L_{2\text{keV}}$, against rest-frame 2500 Å luminosity L_{2500} for 2MASX J193013.80+341049.5 (black star). Also plotted are literature relations from Lusso et al. (2010) and Lusso & Risaliti (2016). The shaded regions represent the 3σ dispersion in the fitted relations.	53
3.9	E_{B-V}/N_{H} ratio vs. intrinsic 2–10 keV X-ray luminosity for 2MASX J193013.80+341049.5 (blue star), and for sources from the sample of Maiolino et al. (2001) (black points). The reddening E_{B-V} is estimated assuming a Galactic standard extinction curve. The column density N_{H} is determined from fitting X-ray spectra. Dashed black line represents the Galactic standard value of E_{B-V}/N_{H}	55
4.1	Broadband X-ray spectrum of IC4329A (top) alongside fit residuals for an absorbed cutoff power law model (bottom). Blue points represents <i>Swift</i> /XRT data while black and red points correspond to <i>NuSTAR</i> FPMA and FPMB data, respectively. Data points are re-binned for plotting clarity.	63
4.2	Distributions of the goodness-of-fit for the χ^2 and Cash statistics (C-stat) for an absorbed power law model fit (Model 1) to the broadband X-ray data for our entire sample.	65
4.3	Distributions of the high energy cutoff E_{cut} for the χ^2 and Cash statistics (C-stat) for an absorbed power law model fit (Model 1) to the broadband X-ray data for our entire sample. We note that the model limit for the value of E_{cut} is 500 keV.	66
4.4	Distributions of the best-fit values and lower bounds of the high energy cutoff, E_{cut} , and coronal temperature, kT_e , for the different spectral models applied to the broadband X-ray data for our entire sample, using C-stat. Mean best-fit values of the coronal cutoff for the different spectral models, as determined from the purple histograms, are as follows: (a) $E_{\text{cut}} = 137 \pm 12$ keV, (b) $E_{\text{cut}} = 156 \pm 13$ keV, (c) $kT_e = 84 \pm 9$ keV.	68
4.5	Lower bounds of E_{cut} and kT_e versus the Eddington ratio L/L_{Edd} for different X-ray spectral models applied to our entire sample, using C-stat. Solid horizontal lines represent mean values of E_{cut} or kT_e for different intervals of L/L_{Edd}	71

4.6	Lower bounds of E_{cut} and kT_e versus SMBH mass M_{BH} for different X-ray spectral models applied to our entire sample, using C-stat. Solid horizontal lines represent mean values of E_{cut} or kT_e for different intervals of M_{BH}	72
4.7	The $\Gamma - L/L_{\text{Edd}}$ relation for our full sample. Solid lines show linear fits to the data for the three different X-ray spectral models applied in this work. Marked in purple are mean values of Γ for different bins of Eddington ratio for the XILLVER reflection model.	75
4.8	Compactness–Temperature ($l - \theta$) diagrams for our full sample, with θ determined using kT_e values from the XILLVER model fit to data. Solid lines correspond to pair production lines for different coronal geometries. The dashed lines in the top panel correspond to boundaries where regions are dominated by electron-electron and electron-proton coupling processes. Data points in the bottom panel plot are color coded by SMBH mass.	76
4.9	kT_e and Γ values obtained from the XILLVER spectral model fit to the data. Solid colored lines correspond to theoretical constraints from Petrucci et al. (2001) for different values of coronal plasma optical depth τ	79
4.10	Coronal plasma optical depth τ versus the Eddington ratio L/L_{Edd} for our entire sample. Optical depth was derived from kT_e and Γ values obtained from the XILLVER spectral model fit to the data. Horizontal purple lines correspond to mean values of τ for different bins of Eddington ratio. Data points are color-coded by their corresponding kT_e value found from X-ray spectral fitting.	80
5.1	$H\alpha$ line width (FWHM) vs. Hydrogen column density (N_{H}), for AGN from the BASS survey (Koss et al., 2017). Colors represent the Osterbrock classification of AGN. Circled are some of the outlier Sy 1-1.8 sources in the sample (red triangles), that have high X-ray obscuration ($N_{\text{H}} \gtrsim 10^{23} \text{ cm}^{-2}$). Sources clustered along $N_{\text{H}} = 10^{20} \text{ cm}^{-2}$ correspond to upper limits on the column density.	84
5.2	X-ray absorbing column density (N_{H}) vs optical extinction (A_V) for Sy1 - 1.9 AGN in the BASS survey, taken from Shimizu et al. (2018). The gray shaded line corresponds to the expected relation for Galactic dust-to-gas ratios. The black dashed line indicates the dividing line between X-ray obscured and unobscured AGN.	85

- 5.3 Simulated *XRISM* spectrum of the core of M87 for a 100 ks exposure, where data is shown in black and best-fit model in red. Figure taken from Kitayama et al. (2014). 88
- 5.4 *Top*: Simulated *HEX-P* spectrum of a typical AGN with a 2–10 keV luminosity of 10^{-11} erg s⁻¹ cm⁻², compared against a *NuSTAR* spectrum of the same source. *Bottom*: Simulated *HEX-P* contour plot of the same AGN in the Γ – E_{cut} plane, compared against *NuSTAR*. Figure credit: Kristin K. Madsen (2020). 89

LIST OF TABLES

<i>Number</i>	<i>Page</i>
2.1 Mean values of the high-energy cutoff, its lower and upper limits from simulated <i>NuSTAR</i> spectra, for <i>Swift</i> /BAT-selected Sy1 AGN . . .	30
2.2 <i>NuSTAR</i> Observation Details for <i>Swift</i> /BAT–selected Sy1 AGN . . .	33
2.3 Redshifts, black hole masses, and best-fit spectral parameters from fitting <i>NuSTAR</i> data for our <i>Swift</i> /BAT-selected Sy1 AGN sample . . .	34
3.1 Details of the <i>NuSTAR</i> and <i>XMM-Newton</i> observations of 2MASX J193013.80+341049.5 considered in this work.	37
3.2 Best-fit parameter values from modeling the broadband X-ray spectrum of 2MASX J193013.80+341049.5	44
3.3 Observation details of the optical spectra of 2MASX J193013.80+341049.5 considered in this work.	48
3.4 Flux details and selected line-width properties of the optical spectra of 2MASX J193013.80+341049.5 considered in this work.	48
4.1 Redshifts, black hole masses and best-fit spectral parameters from fitting broadband X-ray data for select sources from our sample of <i>Swift</i> /BAT-selected Sy1s.	69
5.1 List of X-ray obscured Type 1 AGN observed with the WIRC+Pol near-IR spectropolarimeter (J and H bands) at Palomar Observatory during 2019–2020. These exposure times do not include reference star exposures or overheads.	86

Chapter 1

INTRODUCTION

1.1 A Brief History of Active Galactic Nuclei (AGN)

The universe is filled with incredibly energetic objects and phenomena, with Active Galactic Nuclei (AGN) being one of the most luminous sources of persistent electromagnetic radiation known to date. These objects reside at the centers of so-called active galaxies and are powered by large-scale accretion of matter onto a supermassive black hole (SMBH).

While emission lines originating from the centers of galaxies were discovered as early as the 20th century, it took more than half a century to identify the nature of such sources as what we call Active Galactic Nuclei today. Seyfert (1943) began systematically studying galaxies with nuclear emission lines, leading to the coining of "Seyfert galaxies." However, many years passed before the true nature of these sources was established. The early 1950's brought about substantive developments in radio astronomy, which carved the way for renewed focus on AGN. Many radio sources were discovered in this period with several dedicated radio surveys launched, such as the Cambridge 3C survey (Edge et al., 1959). Synchrotron radiation became widely established as a mechanism powering the radio emission from extragalactic discrete sources, leading to predictions of enormous energies contained within radio galaxies (Burbidge et al., 1959).

In the 1960's, a major breakthrough was made by Caltech's own Maarten Schmidt, who began the quest of finding optical classifications and redshifts of radio galaxies. Schmidt, along with other astronomers such as Allan Sandage, identified several star-like objects with broad optical emission lines coincident with radio sources; these objects were referred to as quasi-stellar radio sources, or "quasars." In 1963, Schmidt published the groundbreaking measurement of the redshift of the quasar 3C 273 (Schmidt, 1963), where he noted that if the object was indeed extragalactic, the large redshift implied that the emission originated in a nuclear region less than 1 kpc in diameter with a total radiated energy of at least 10^{59} ergs.

Not long after the discovery of quasars, Sandage (1965) reported the existence of a population of radio quiet quasars. By this stage, the cosmological nature of these quasi-stellar objects (QSOs) was established and parallels were drawn between

Seyfert galaxies at lower redshifts and more distant QSOs. Investigations into the nature of the energy source powering these objects eventually led to the proposal that accretion of matter onto a supermassive black hole was the central engine, capable of producing the energies observed from the most luminous QSOs from a reasonable SMBH mass (Salpeter, 1964; Zel'dovich, 1964). Physical theories of accretion via a thin disk developed by Shakura & Sunyaev (1973) became widely adopted as a common model for describing accretion flow onto compact objects such as black holes.

The advent of X-ray astronomy in the 1960's and 1970's opened the door for building a more complete picture of the nature of AGN. Giacconi et al. (1962) led the launch of the first rocket to detect an extrasolar X-ray source in the constellation Scorpius. In 1970, *Uhuru*, the first satellite dedicated to systematically exploring the X-ray sky was launched, with detections made of X-rays from Seyfert galaxies. Elvis et al. (1978) then established strong X-ray emission to be a characteristic of Seyfert galaxies and by the 1980's, the launch of more X-ray satellites confirmed strong X-ray emission to be ubiquitous in all types of AGN and could act as a valuable diagnostic tool to probe the inner regions of AGN.

1.2 The Classical Unified Model of AGN

Multi-wavelength studies of AGN, particularly at optical wavelengths, revealed a broad diversity in the types of AGN present. Osterbrock (1978) developed a classification system for AGN based on broad and narrow emission line characteristics in AGN optical spectra that continues to be used in the present day. In this classification system, Type 1 AGN contain both broad and narrow emission line features in their optical spectra, whereas Type 2 AGN exhibit only narrow emission lines. While a broad division was made between radio-loud and radio-quiet AGN, a question was raised of whether the diversity of AGN classes could be attributed to an observational viewing angle effect. A major observational breakthrough came with spectropolarimetric measurements made of the Seyfert galaxy NGC 1068 by Antonucci & Miller (1985), which revealed a Type 1 optical spectrum in polarized light, despite the AGN being classified as a prototypical Type 2 AGN. Such an observation was interpreted in terms of a broad-line region (BLR) and central continuum source that was obscured from the observer by a dusty torus surrounding the SMBH. Nuclear emission was scattered into the observer's line of sight by material in the BLR, thereby polarizing the photons.

Antonucci (1993) proposed the formalism for the basic unified model of AGN, in which differences between observational classes of AGN are attributed to an orientation effect where the SMBH and torus are viewed along different angles along the observer's line of sight. Within this classical unified model, there are several key components of an AGN, illustrated in Figure 1.1 and described as follows:

- Supermassive black hole (SMBH): located at the center of an AGN, powering the luminous emission via gravitational infall of matter. Its mass can range from $\sim 10^6$ – $10^{10} M_{\odot}$. The Schwarzschild radius, corresponding to the black hole event horizon, ranges in size from 10^{-7} pc for a $10^6 M_{\odot}$ black hole, to 10^{-3} pc for a $10^{10} M_{\odot}$ black hole.
- Accretion disk: commonly modeled as a geometrically thin, optically thick structure that is formed from material rotating in the vicinity of the SMBH. Matter loses angular momentum as it spirals inwards and is accreted onto the SMBH, resulting in gravitational energy being converted to thermal blackbody radiation.
- Corona: a hot plasma located close to the SMBH producing the bulk of the continuum X-ray emission via inverse-Compton scattering of optical/UV photons from the accretion disk by electrons within the plasma.
- Broad-line region (BLR): composed of high-density, dust-free, partially ionized gas clouds moving at velocities $> 1000 \text{ km s}^{-1}$ from which broad, permitted emission lines are observed. Located ~ 0.01 – 1 pc from the SMBH.
- Obscuring torus: an axisymmetric structure composed of dusty gas that obscures radiation from the central regions of the AGN and emits radiation in the infrared band. Its radial extent ranges from ~ 0.1 – 10 pc.
- Narrow-line region (NLR): a region of low-density gas moving at lower velocities ($< 1000 \text{ km s}^{-1}$) compared to the BLR residing beyond the torus at \sim kpc distances. This gas emits narrow permitted and forbidden emission lines.
- Relativistic jet: usually bi-polar, collimated, energetic outflows of particles moving at relativistic velocities perpendicular to the accretion disk. Found in some AGN and can extend up to Mpc scales for particularly strong jets. The jets radiate non-thermal emission via synchrotron and inverse-Compton scattering processes.

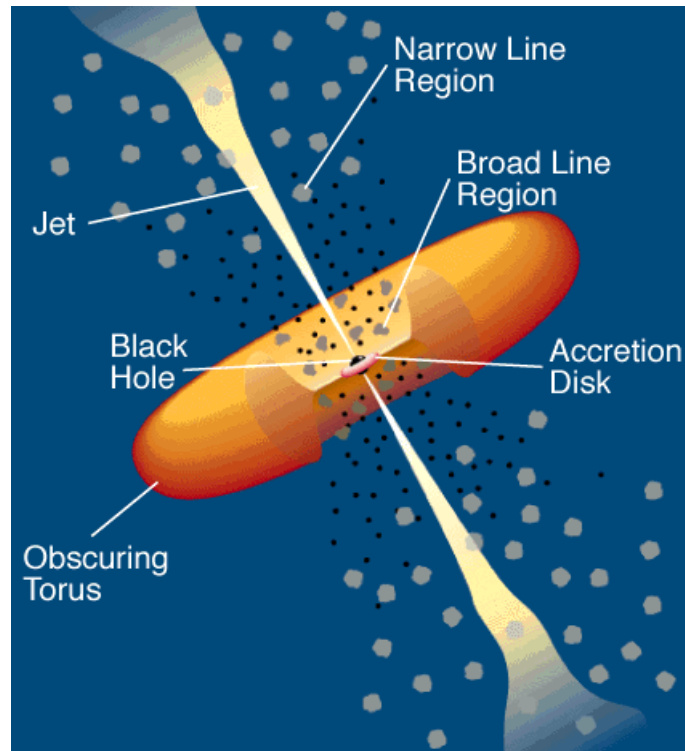


Figure 1.1: Illustration of the basic components of an AGN under the classical unified paradigm. Figure taken from Urry & Padovani (1995).

The basic unified model accounts for the narrow emission lines observed in both Type 1 and 2 AGN and the absence of broad emission lines in the optical spectra of Type 2 AGN, since the BLR is obscured by the torus in Type 2 AGN which are typically viewed at edge-on inclinations. In Type 1 AGN, the torus is viewed at face-on angles with a direct, unobscured view of the BLR.

Evidence for a dusty toroidal structure has been found in recent years through mid-infrared imaging and interferometric observations of AGN (e.g., Packham et al., 2005; Burtscher et al., 2013). Early X-ray studies also generally showed most Type 1 AGN to be unobscured while Type 2 AGN were obscured (e.g., Awaki et al., 1991). Other observations such as the orientation of relativistic radio jets (e.g., Zensus et al., 1990), the bi-conical structure of the NLR (e.g., Storchi-Bergmann et al., 1992), and position angle of polarized photons (e.g., Evans et al., 1991) broadly supported the unified AGN paradigm. However, this unification picture still remains an oversimplification, with a growing number of AGN exhibiting properties that cannot be reconciled by the basic unified paradigm. This has led to the development of different variants of unification models that more accurately capture the diversity of AGN phenomena observed.

1.3 Modern Picture of the Anatomy of an AGN

The picture of a uniform, single density torus is clearly a simplified approximation, with the modern view of the torus and associated structures being more complex and dynamic. Rather than being a homogeneous, smooth toroidal structure, it is likely to be clumpy in nature, composed of many optically thick clouds (e.g., Krolik & Begelman, 1988a). Evidence for a clumpy or filamentary dust structure within the torus has been found in recent years through infrared interferometric observations (e.g., Tristram et al., 2007; López-Gonzaga et al., 2016) and short timescale variability of the line-of-sight column density in some AGN (e.g., Marinucci et al., 2016). Such a picture of a clumpy torus can also generally explain transitions within an AGN between Type 1 and Type 2 observed in a number of sources (e.g., Aretxaga et al., 1999; Piconcelli et al., 2007), as clumps passing along the observer’s line of sight can cause a temporary increase in column density and obscure the central region, leading to a Type 2 classification.

Not only can cloud obscuration along the observer’s line of sight blur the border between Type 1 and Type 2 AGN, leading to misclassifications, but there are a growing number of AGN with conflicting X-ray and optical classifications, which further challenges the unified model. X-ray classification of AGN is typically based on measurements of the hydrogen column density (N_{H}), with the approximate dividing line above which an AGN is considered to be obscured at $N_{\text{H}} > 10^{22} \text{ cm}^{-2}$ (Ricci et al., 2017b). However, a number of exotic sources have been identified that show disagreement between their optical and X-ray classification. Some narrow line Type 2 AGN are X-ray unabsorbed, and there is much debate on whether they represent a class of AGN lacking a BLR (Panessa & Bassani, 2002; Tran et al., 2011; Merloni et al., 2014). Many of these X-ray unabsorbed Type 2 AGN exhibit low rates of accretion, and thus are unable to sustain dynamic structures such as the BLR and torus (Elitzur & Ho, 2009).

The opposite case of AGN misclassification—optically classified Type 1 AGN that are shown to be X-ray absorbed ($N_{\text{H}} > 10^{22} \text{ cm}^{-2}$)—also exist. In this thesis work, I identified such a misclassified AGN and performed a detailed broadband X-ray spectroscopic analysis of the source in addition to examining multi-wavelength data in order to probe the possible mechanism of complex obscuration present (Kamraj et al., 2019). Whilst previous studies have found Type 1 AGN with large X-ray absorbing column densities (e.g., Shimizu et al., 2018), explanations for the existence of such objects have varied widely. One explanation that is consistent with

the unified model is that our line of sight grazes the edge of the obscuring torus where the cloud distribution is less dense, but still provides significant X-ray absorption. If we model the torus to have a clumpy distribution, then another possibility is that a clump has entered our line of sight during the X-ray observation, causing a temporary increase in N_{H} . Another possible idea is that the BLR itself provides extra X-ray obscuration towards the corona (Davies et al., 2015) and consists of neutral, dust-free gas that is an inner extension of the dusty molecular torus.

Various studies have also shown the level of nuclear obscuration to be correlated with AGN luminosity, with a decrease in the amount of circumnuclear material in more luminous AGN (e.g., Fabian et al., 2006; Ueda et al., 2014; Ricci et al., 2017a). The covering factor, defined as the fraction of sky covered by the obscuring material as seen from the SMBH, has been shown through studies at multiple wavelengths to be negatively correlated with accretion rate (e.g., Treister et al., 2008; Lusso et al., 2013; Stalevski et al., 2016). Processes such as AGN-driven outflows and radiative-driven feedback can clear away circumnuclear gas and dust, leading to the observed trends (e.g., Hopkins & Elvis, 2010; Ricci et al., 2017a). These results have led to the development of *radiation-regulated unification* models, wherein the probability of an AGN being obscured and thus classified as Type 2 is driven by the accretion rate, which is characterised by the Eddington ratio (Ricci et al., 2017a). The Eddington ratio is defined as L/L_{Edd} , where L is the bolometric AGN luminosity and L_{Edd} is the Eddington luminosity. The Eddington luminosity for a SMBH of mass M_{BH} is defined by the following equation:

$$L_{\text{Edd}} = \frac{4\pi G M_{\text{BH}} m_p c}{\sigma_T} \quad (1.1)$$

where G is the gravitational constant, m_p is the proton mass, c is the speed of light, and σ_T is the Thompson scattering cross section. Radiation-regulated feedback can be a cyclical process, in which accretion is triggered in an initially quiescent SMBH. As material accumulates around the SMBH, the covering factor increases and the source becomes obscured. Meanwhile the Eddington ratio gradually increases as accretion proceeds. Eventually the accretion luminosity becomes high enough that radiation pressure expels circumnuclear material, resulting in an unobscured AGN. Once the remaining reservoir of material has been accreted, the AGN luminosity drops and the cycle is repeated (see Figure 1.3 for a graphical illustration of this process)

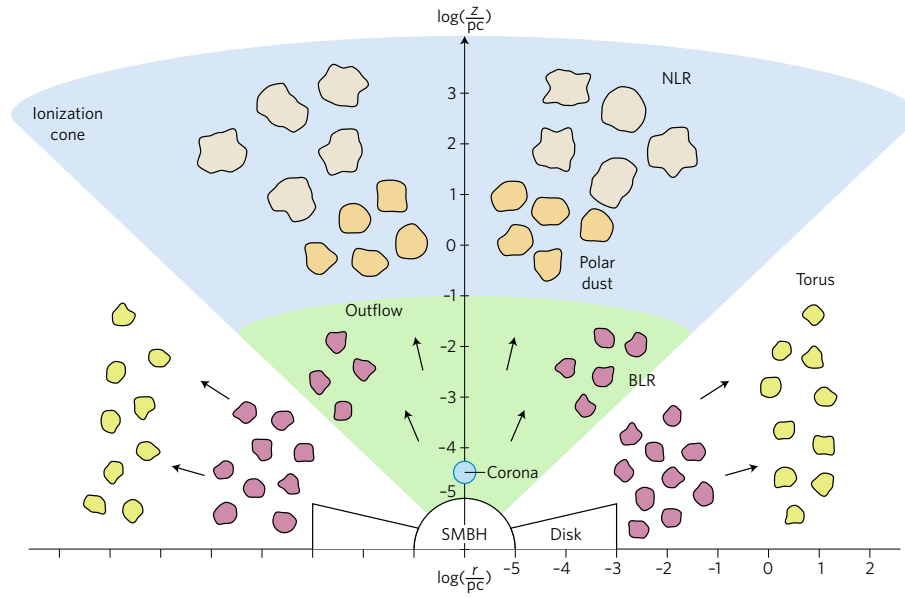


Figure 1.2: Illustration depicting a modern representation of the key structures comprising an AGN, as viewed along the equatorial and polar directions. Figure taken from Ramos Almeida & Ricci (2017). Different colored clumps correspond to different compositions/structures; green and blue shaded regions mark the inner and outer ionization cones.

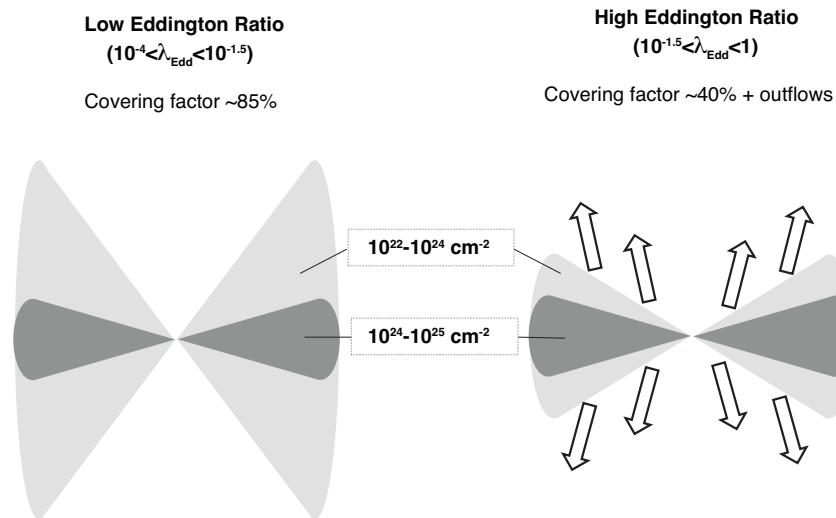


Figure 1.3: Schematic diagram describing radiation-regulated feedback, where λ_{Edd} refers to the Eddington ratio. Shaded grey regions correspond to different ranges of obscuring column density N_{H} . Figure taken from Ricci et al. (2017a).

1.4 The Nature of the Corona in AGN

One of the most important components of an AGN is the corona, which is responsible for powering the luminous X-ray continuum emission that is observed. It is generally considered that the corona is composed of a hot cloud of plasma located close to the accretion disk (e.g., Haardt & Maraschi, 1993; Merloni & Fabian, 2001). Within the corona, electrons Compton upscatter optical and UV photons from the accretion disk up to X-ray energies (Rybicki & Lightman, 1979). Despite the corona being an integral component of AGN, much is still unknown about its nature, such as its geometry, location, and its physical properties.

While many of the properties of the corona are a mystery, it has been established to be a compact structure. The observed rapid variability of the 2–10 keV X-ray emission seen in many AGN, combined with X-ray spectral timing and reverberation mapping, strongly indicate that the corona is physically compact, of the order 3–10 gravitational radii ($r_g = GM_{BH}/c^2$) in radius and height above the SMBH (e.g., McHardy et al., 2005; Fabian et al., 2009; Emmanoulopoulos et al., 2014; Uttley et al., 2014). Observations of microlensing in quasars also indicate compact X-ray emitting regions (Chartas et al., 2016).

In addition to being physically small, the corona can also be radiatively compact, meaning that interactions involving significant energy exchange between particles and photons are commonplace within the source, leading to a large ratio of coronal luminosity to radius (Fabian et al., 2015). This radiative compactness can be characterized by a dimensionless parameter l (Guilbert et al., 1983), defined as:

$$l = 4\pi \frac{m_p}{m_e} \frac{R_g}{R} \frac{L_X}{L_E} \quad (1.2)$$

where m_p and m_e are the proton and electron mass, respectively, R_g is the gravitational radius, R is the coronal radius, L_X is the coronal luminosity, and L_E is the Eddington luminosity. A value of $l \sim 1$ corresponds to a particle losing significant energy in traversing the corona; values of $l \gg 1$ are considerably radiatively compact (Fabian et al., 2015). As the density of high-energy photons ($\gtrsim 1$ MeV) is increased, photon-photon collisions can lead to electron-positron pair production. Increasing energy supplied to the corona thus has the effect of producing more particle pairs to share the available energy. In this way, pair production can become a runaway process that exceeds particle annihilation, thereby limiting any further

rise in the temperature of the corona, acting as an l -dependent thermostat (e.g., Svensson, 1984; Zdziarski, 1985; Stern et al., 1995).

The coronal temperature, kT_e , can also be characterized by a dimensionless parameter $\theta = kT_e/m_e c^2$, where k is the Boltzmann constant. The simplest thermalization process within the corona consists of two-body collisions between particles. There is a longstanding problem of how energy is supplied to heat the corona, since sources generally have a cooling timescale that is shorter than the light crossing timescale (e.g., Ghisellini et al., 1993; Merloni & Fabian, 2001; Fabian et al., 2015). A popular theory is that the corona is powered by magnetic fields originating from the strong differential rotation of the accretion disk (e.g., Merloni & Fabian, 2001). The thermostat behavior of the corona defines a pair production line in the $l - \theta$ plane to the right of which a static physical corona cannot exist. The exact position of the pair line depends on factors such as the coronal geometry and nature of the soft photon field present. Figure 1.4 illustrates the location of some pair lines for different geometries, along with particle coupling lines, taken from Fabian et al. (2015).

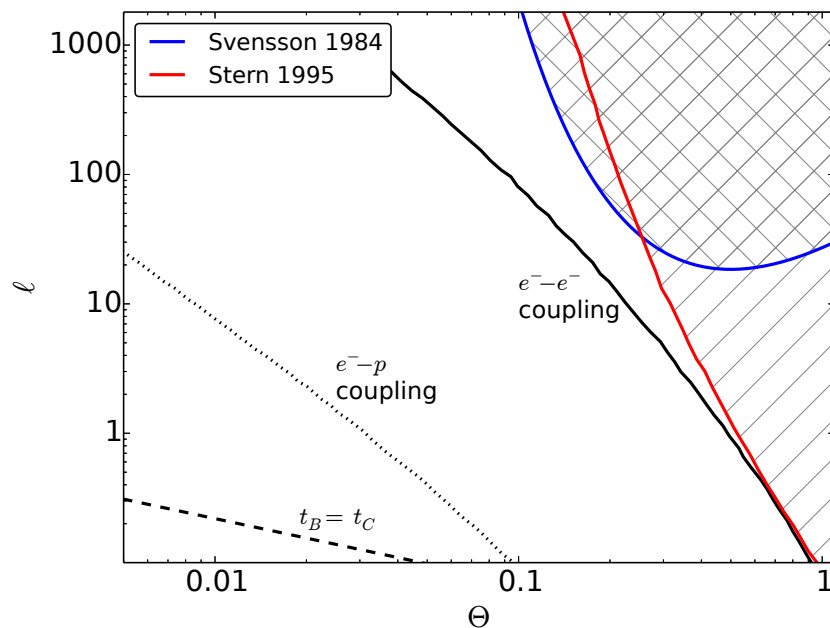


Figure 1.4: Plot of the $l - \theta$ plane, showing boundaries for runaway pair production, electron-electron coupling, electron-proton coupling, and the line where Compton cooling dominates over Bremsstrahlung cooling ($t_B = t_C$). The solid red and blue lines correspond to pair lines for a slab corona and isolated cloud corona, respectively. Figure taken from Fabian et al. (2015).

Stern et al. (1995) computed the pair production line for a slab-like coronal geometry, shown in red in Figure 1.4. Svensson (1984) treated the corona as an isolated cloud and calculated the pair production line to have an analytical form $l \sim 10\theta^{5/2} \exp^{1/\theta}$, shown in blue.

1.5 Broadband X-ray Spectral Modeling as a Tool to Study AGN

Modeling of the broadband X-ray spectra of AGN is a powerful tool to probe the inner regions of the accretion disk and elucidate the nature of the circumnuclear material and corona. The shape of the primary X-ray coronal continuum is sensitive to various physical conditions within the plasma such as coronal temperature (kT_e) and optical depth (τ) (e.g., Haardt & Maraschi, 1993; Titarchuk, 1994), in addition to properties such as the geometry of the corona and the nature of the seed photon spectrum. The flux of this Comptonized continuum is often approximated to have a power law form with an exponential cutoff at high energies $\propto E^{-\Gamma} e^{-E/E_{\text{cut}}}$, where E is the photon energy, Γ is the continuum photon index and E_{cut} is the high-energy cutoff (e.g., Rothschild et al., 1983; Titarchuk & Lyubarskij, 1995). Parameters obtained from fitting spectral models to broadband X-ray data thus correspond to physical properties of the corona, with the temperature related to the cutoff energy via $E_{\text{cut}} \sim 2-3 kT_e$, assuming a slab-like coronal geometry (Petrucci et al., 2001).

Illumination of the coronal continuum onto the accretion disk and torus gives rise to characteristic reprocessing features, producing an X-ray reflection spectrum. Most notably, is a neutral Fe $K\alpha$ fluorescence line at 6.4 keV and a Compton reflection hump (CRH) feature broadly peaking at 20-30 keV, produced from Compton down-scattering of hard X-rays (> 10 keV) and absorption of soft X-ray photons originating from the corona by dense material in the accretion disk or torus (see Figure 1.5). While other weaker emission lines may be observed, such as from Fe $K\beta$ or Ni transitions, the Fe $K\alpha$ line is most prominent due to the high relative abundance of Fe and the high yield of the fluorescent $K\alpha$ line transition. The shape of the Fe line profile can also be used to map the innermost regions of the SMBH, with effects such as Doppler shifts and gravitational redshifts smearing out and broadening the line profile (e.g., Fabian et al., 1989).

In addition to reprocessing signatures, absorption features are commonly present in AGN X-ray spectra. Most of the circumnuclear absorbing material is neutral in nature, though the BLR is partially ionized and regions very close to the SMBH may contain strongly ionized matter. In the soft X-ray band (< 10 keV), absorption from

warm ionized gas along the line of sight is often observed. These warm absorbers may also travel at high velocities in the form of an ultra-fast outflow, leading to broad absorption trough signatures in X-ray spectra (e.g., Tombesi et al., 2012). Below ~ 1 keV, various weak ionized emission lines from elements such as C, N, O, Ni, and Fe may be observed, with line blending possibly resulting in a "soft excess" spectral component (e.g., Ballantyne et al., 2002). The nature of the soft excess emission is still not established, with multiple theories proposed for its origin. Apart from line blending, some other possible models include a warm (~ 0.1 – 1 keV) and optically thick Comptonizing corona or relativistically blurred ionized reflection as the source of the soft excess emission (e.g., García et al., 2019).

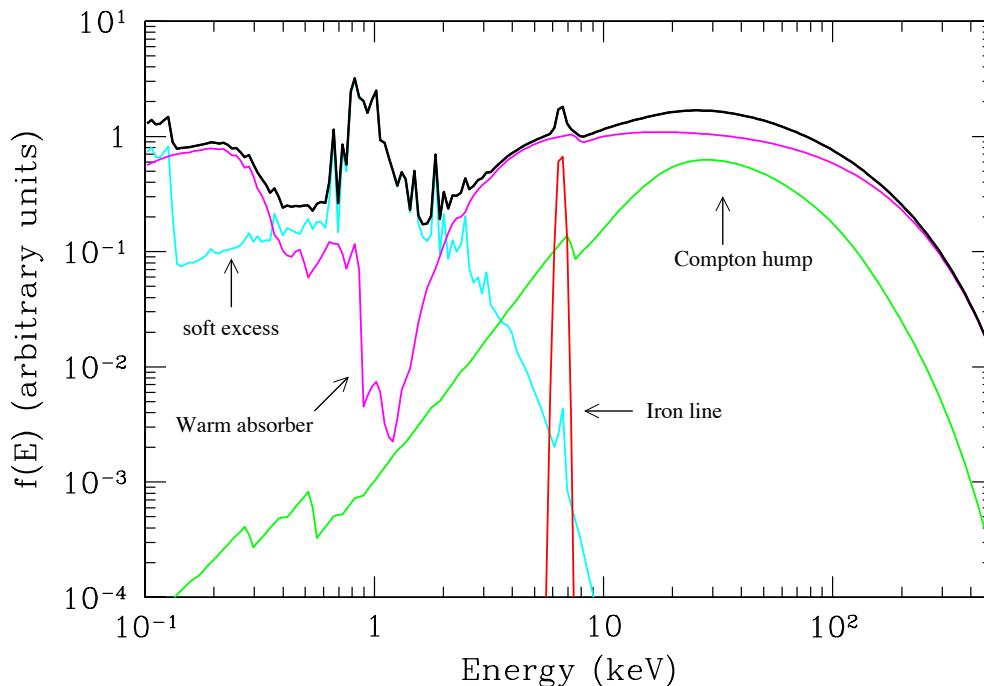


Figure 1.5: An example X-ray spectrum of a Type 1 AGN from Risaliti & Elvis (2004), showing the main reflection features such as the 6.4 keV Fe $K\alpha$ line and CRH. Also shown in magenta is absorption at soft (< 10 keV) energies by warm gas and ‘soft excess’ emission that is possibly attributed to line blending or thermal emission of a warm plasma with $kT \sim 0.1 - 1$ keV.

Spectral models that compute the reflected X-ray spectrum can be broadly classified into two main categories: phenomenological reflection models and physically-motivated reflection models. A popular phenomenological model for computing the reprocessed X-ray emission is PEXRAV (Magdziarz & Zdziarski, 1995), which models reflection off a slab of infinite extent and optical depth. However, such

simplified phenomenological models are unable to constrain the geometry of the reprocessing material, which has led to the development of a number of physically-motivated spectral models employing toroidal geometries. Some widely used torus models include MYTORUS (Murphy & Yaqoob, 2009) and BNTORUS (Brightman & Nandra, 2011). While such torus models provide a more realistic description of the reprocessing material, they are still limited in the range of physical scenarios they describe. For example, MYTORUS assumes a uniform density torus with a fixed opening angle of 60° . A new model, BORUS, developed by Baloković et al. (2018), provides more flexibility in modeling the torus geometry, taking into account the clumpy (as opposed to uniform) composition of the torus, by allowing the line-of-sight column density to be decoupled from the torus column density, and features the opening angle as a free parameter. Advanced reflection models have also been developed in recent years that more accurately model the physics of reprocessed radiation from the corona. For example, the RELXILL family of disk reflection models (García et al., 2014) adopt a rich atomic database, fully calculate the angular distribution of reflected radiation and contain various geometrical models of the illuminating coronal source.

Technological advances in observational X-ray astronomy over the past few decades have propelled studies of AGN using broadband X-ray spectroscopy. The launch of satellites with focusing optics in the X-ray band such as *XMM-Newton*, *Chandra*, and *NuSTAR*, combined with non-focusing X-ray observatories such as *Swift* performing wide field surveys, have enabled detailed characterization of the SMBH system and circumnuclear environment for large samples of AGN in our local universe. In particular, the launch of the *NuSTAR* observatory (Harrison et al., 2013) has revolutionized studies of AGN coronae. Being the first focusing hard X-ray telescope in orbit providing spectral coverage in the 3–79 keV band, *NuSTAR* has allowed measurements of the coronal high energy cutoff (E_{cut}) from single epoch observations in relatively large samples of nearby AGN for the first time (e.g., Ballantyne et al., 2014; Baloković et al., 2014; Kara et al., 2017). Prior to the launch of *NuSTAR*, measurements of the coronal cutoff energy have been difficult to obtain, since they require high-quality hard X-ray coverage above 10 keV in order to detect possible turnover in the spectrum at high energies. Previous studies of E_{cut} performed with non-focusing hard X-ray instruments such as *CGRO/OSSE* (e.g., Rothschild et al., 1983; Zdziarski et al., 2000), *BeppoSAX* (e.g., Nicastro et al., 2000; Dadina, 2007) and *INTEGRAL* (e.g., Beckmann et al., 2009; Ricci et al., 2011; Malizia et al., 2014) had very limited sensitivity and could only measure E_{cut} for the brightest AGN.

Surveys of the local AGN population have also made more readily available high quality broadband X-ray data for larger samples of sources. In this thesis work, I study the coronal properties of large samples of unobscured Seyfert 1 AGN selected from the *Swift*/BAT all-sky survey that have been observed with *NuSTAR*. The *Swift*/BAT catalog (e.g., Baumgartner et al., 2013; Oh et al., 2018) comprises of sources detected by the *Swift*/BAT all-sky scanning instrument (Gehrels et al., 2004) and provides a large sample of local, bright AGN with uniform sky coverage.

NuSTAR also conducts deep, wide field surveys in galactic and extragalactic fields as part of one of its primary mission objectives to probe the AGN population that forms the bulk of the Cosmic X-ray Background (CXB) peaking at 20-30 keV. Part of this thesis work examines samples of Seyfert 1 AGN observed with *NuSTAR* as part of its Extragalactic Legacy Surveys program¹. The *NuSTAR* Extragalactic Legacy Survey performs snapshot ~ 20 ks exposure observations of AGN detected by *Swift*/BAT. The 100-fold increase in sensitivity of the *NuSTAR* telescope compared to the *Swift*/BAT instrument enables robust spectral modeling with a minimal *NuSTAR* exposure of ~ 20 ks. With even longer exposure *NuSTAR* observations, it is possible to obtain tight limits on X-ray spectral parameters characterizing the coronal emission. While some studies of coronal cutoff energies in samples of AGN have been performed in the past, (e.g., Ricci et al., 2017b), most of these measurements utilized lower quality hard X-ray data from non-focusing instruments such as *Swift*/BAT and *Suzaku*. Robust constraints on coronal high energy cutoffs obtained with *NuSTAR* for large samples of unobscured AGN were absent in the literature prior to this thesis work.

1.6 Outline of this Thesis Work

This thesis focuses on studying the properties of the corona in samples of Seyfert 1 AGN using the technique of broadband X-ray spectroscopy. This work heavily utilizes spectroscopic data taken with *NuSTAR*, due to its unprecedented sensitivity at X-ray energies above 10 keV, where the coronal emission dominates. Unobscured, Seyfert 1 AGN are primarily studied in this thesis, since the X-ray spectral shape is strongly affected by reprocessing features, which are dominant in obscured AGN. This makes it difficult to disentangle the intrinsic coronal continuum shape from reflection features in obscured sources, particularly for measurements of coronal cutoff energy, where curvature at high energies can be attributed both to a high energy turnover and reprocessing (e.g. CRH).

¹https://www.nustar.caltech.edu/page/legacy_surveys

Chapter 2 presents the first study of this thesis, which explores coronal cutoff energies in a sample of 46 *Swift*/BAT-selected Seyfert 1 AGN observed with *NuSTAR* as part of the ~ 20 ks exposure Extragalactic Legacy Survey (published in Kamraj et al. 2018). I performed spectral modeling of the *NuSTAR* data for each source in order to measure the high energy cutoff of the coronal continuum. With these coronal cutoff measurements, I mapped out the compactness-temperature ($l - \theta$) plane for the sample. I discuss the importance of annihilation and pair production processes in regulating the temperature of the corona and the implications of low coronal temperatures on the cooling mechanisms within the corona.

In Chapter 3, I present a detailed study of the AGN 2MASX J19301380+3410495 identified from my first sample with a particularly low coronal temperature (published in Kamraj et al. 2019). This source is peculiar not only for its low temperature corona, but also shows high levels of X-ray obscuration despite being optically classified as an unobscured Type 1 AGN. I performed both detailed broadband X-ray spectral modeling using multi-epoch *Swift*/XRT, *XMM-Newton* and *NuSTAR* observations and also examined multi-wavelength properties of this source in order to investigate the mismatch between X-ray and optical classifications. The existence of such rare classes of AGN that show conflicting X-ray and optical classifications continue to challenge classical unified models of AGN.

Chapter 4 presents the final study of this thesis, in which I performed the first systematic study of the coronal properties of a large sample of unobscured AGN observed with *NuSTAR* (Kamraj et al. 2021, accepted). I compiled a sample of 195 observations of Seyfert 1 AGN selected from the *Swift*/BAT survey that also have short *NuSTAR* legacy observations or long exposure targets observed as part of individual *NuSTAR* Guest Observer programs. The combination of superior quality broadband X-ray data with a large sample size enables robust characterization of the physical properties of the corona in the local, unobscured AGN population. I investigate how coronal parameters connect with fundamental accretion properties in AGN, such as the Eddington ratio and SMBH mass. While some past studies of AGN that did not utilize *NuSTAR* measurements have found tentative correlations between the coronal high energy cutoff and accretion parameters such as the Eddington ratio (e.g., Ricci et al., 2018), studies of small samples of AGN observed with *NuSTAR* have shown no evidence for such a correlation (Tortosa et al., 2018).

In Chapter 5 I discuss possible future extensions of my thesis work aimed at probing rare classes of exotic AGN similar to 2MASX J19301380+3410495 that show

conflicting optical and X-ray classifications. I examine the possibility of using complementary multi-wavelength techniques in addition to broadband X-ray spectroscopy, such as infrared spectropolarimetry and spectral energy distribution fitting, in order to probe obscuration within such sources. I also discuss future prospects for the study of AGN coronae with prospective next generation X-ray telescopes. Finally, in Chapter 6, I present a summary of my thesis research and make concluding remarks.

*Chapter 2***CORONAL PROPERTIES OF SWIFT/BAT-SELECTED SEYFERT
1 AGN OBSERVED WITH NUSTAR**

N. Kamraj, F. A. Harrison, M. Baloković, A. Lohfink, and M. Brightman. Coronal Properties of Swift/BAT-selected Seyfert 1 AGNs Observed with NuSTAR. *The Astrophysical Journal*, 866:124, 2018. doi: 10.3847/1538-4357/aadd0d.

Nikita Kamraj¹, Fiona A. Harrison¹, Mislav Baloković², Anne Lohfink³, Murray Brightman¹

¹Cahill Center for Astronomy and Astrophysics, California Institute of Technology, Pasadena, CA 91125, USA

²Yale Center for Astronomy & Astrophysics, 52 Hillhouse Avenue, New Haven, CT 06511, USA

³Department of Physics, Montana State University, 211 Montana Hall, Bozeman, MT 59717, USA

Abstract

The *NuSTAR* observatory, with its high sensitivity in hard X-rays, has enabled detailed broadband modeling of the X-ray spectra of Active Galactic Nuclei (AGN), thereby allowing constraints to be placed on the high-energy cutoff of the X-ray coronal continuum. We investigate the spectral properties of a sample of 46 *NuSTAR*-observed Seyfert 1 AGN selected from the *Swift*/BAT 70-month hard X-ray survey. Our measurements of the high-energy cutoff of the continuum from modeling the *NuSTAR* X-ray spectra are used to map out the temperature – compactness ($\theta - l$) plane for AGN coronae. We find that most of the coronae lie clustered near the boundary for runaway pair production, suggesting that annihilation and pair production act to regulate the temperature of the corona. We discuss the implications of coronae whose high-energy cutoff may indicate a low coronal temperature on the heating and thermalization mechanisms in the corona.

2.1 Introduction

The continuum X-ray emission from Active Galactic Nuclei (AGN) is believed to originate in a hot, compact corona located above the accretion disk (e.g., Haardt & Maraschi, 1993). Compton upscattering of UV and optical photons from the inner accretion disk by coronal electrons produces a power-law-like X-ray continuum, with a cutoff at energies determined by the electron temperature T_e (e.g., Rybicki & Lightman, 1979; Zdziarski et al., 2000). The shape of the coronal continuum is sensitive to properties such as the seed photon field, electron temperature, optical depth, and observer viewing angle. The observed rapid variability of the 2–10 keV emission in many AGN, combined with X-ray spectral timing and reverberation mapping, strongly indicate that the corona is physically compact, of the order 3–10 gravitational radii (Fabian et al., 2009; Kara et al., 2013; Emmanoulopoulos et al., 2014; Fabian et al., 2015). The gravitational radius is defined to be GM_{BH}/c^2 , where M_{BH} is the supermassive black hole mass. Such radiatively compact sources can exchange significant energy between particles and photons, with the compactness characterised by the dimensionless parameter l (Guilbert et al., 1983), defined as:

$$l = 4\pi \frac{m_p}{m_e} \frac{R_g}{R} \frac{L}{L_E} \quad (2.1)$$

where m_p and m_e are the proton and electron mass, respectively, R_g is the gravitational radius, R the source radius, L the source luminosity, and L_E the Eddington luminosity. The electron temperature T_e can also be characterised by the dimensionless parameter $\theta = k_B T_e / m_e c^2$, where k_B is the Boltzmann constant. For sufficiently energetic photons, photon-photon collisions can lead to electron-positron pair production in the corona (Svensson, 1982; Guilbert et al., 1983; Zdziarski, 1985). At high coronal temperatures, when the Wien tail of the power-law spectrum extends above $2m_e c^2$, pair production can quickly become a runaway process, exceeding annihilation (Svensson, 1984). This will limit any further rise in temperature, thus acting as an l -dependent thermostat (Svensson, 1984; Zdziarski, 1985; Stern et al., 1995).

The *NuSTAR* observatory (Harrison et al., 2013), being the first focusing hard X-ray telescope in orbit, has enabled detailed, high signal-to-noise spectra to be obtained in the 3–79 keV band for many local AGN. *NuSTAR* spectral modeling can thus place constraints on the spectral photon index and high-energy cutoff of the coronal X-ray continuum, enabling robust estimates of l and θ . One of the primary goals of the

NuSTAR mission is to perform an extragalactic survey of the hard X-ray sky, in order to characterise the AGN population. We define hard X-rays as photons with energies > 10 keV. As part of its Extragalactic Legacy Surveys program¹, the *NuSTAR* observatory has performed snapshot ~ 20 ks observations of local AGN detected in the all-sky survey with the Burst Alert Telescope (BAT) instrument onboard the *Neil Gehrels Swift Observatory* (Gehrels et al., 2004; Baumgartner et al., 2013). Though previous work has provided broad constraints on the high-energy cutoff for samples of bright AGN, tight constraints for particular AGN only became available recently thanks to *NuSTAR* (e.g., Ballantyne et al., 2014; Brenneman et al., 2014; Marinucci et al., 2014; Fabian et al., 2015; Baloković et al., 2015). The 100-fold increase in sensitivity of the *NuSTAR* telescope compared to the *Swift*/BAT instrument enables robust spectral modeling with a minimal *NuSTAR* exposure of ~ 20 ks. With even longer exposure *NuSTAR* observations, it is possible to obtain tight limits on X-ray spectral parameters and perform reverberation mapping measurements of coronal size.

In this paper, we study a sample of 46 *Swift*/BAT selected Seyfert 1 (Sy1) AGN observed with *NuSTAR*, in order to map out the location of these sources on the temperature – compactness ($\theta - l$) diagram for AGN coronae. We do not include *Swift*/XRT data in our spectral modeling as the limited data quality of available simultaneous *Swift*/XRT data introduces difficulties in obtaining constraints on parameters such as the cutoff energy. The complexity of features in soft X-ray spectra would ideally require high signal-to-noise ratio, simultaneous spectra from soft X-ray telescopes with larger collecting area to model robustly, which are currently unavailable for the targets in our sample. In section 4.2, we discuss the sample used in this study, the data reduction, and analysis procedures adopted. Observational details of our AGN sample are presented in Table 2.2 of the appendix. In section 4.4, we present our results and discuss the heating and cooling mechanisms operating in the corona. We discuss future, deeper *NuSTAR* observations of AGN in our sample with potential cutoffs in the *NuSTAR* band in section 2.4, and present a summary in section 4.5. In this work, all uncertainties were calculated at the 90% confidence level and standard values of the cosmological parameters ($h_0 = 0.7$, $\Omega_\Lambda = 0.7$, $\Omega_m = 0.3$) were used to calculate distances.

¹https://www.nustar.caltech.edu/page/legacy_surveys

2.2 Sample, Data Reduction, and Analysis

Sample of Seyfert 1 AGN

We selected our sample from AGN identified in the *Swift*/BAT 70-month hard X-ray catalogue (Gehrels et al., 2004; Baumgartner et al., 2013). From the full catalogue, we selected *NuSTAR*-observed AGN with known redshifts and classified as Sy1 from optical hydrogen emission line measurements, or from available data from the NASA/IPAC Extragalactic Database (NED). The full list of AGN included in our study, along with their *NuSTAR* observation details, may be found in Table 2.2 of the appendix. Figure 2.1 shows the location of our sources on the redshift-luminosity plane, with the luminosity values determined from the *Swift*/BAT fluxes in the 14–195 keV range. We confirmed sources at high redshift to not be beamed AGN or blazar candidates from observations of their optical spectra and cross-matching with the Roma Blazar Catalog (Massaro et al., 2009). We found two sources which were misclassified from NED and were removed from our sample. We excluded 9 sources from our original sample due to lack of constraints on the high-energy cutoff from spectral fitting. Our final sample consists of 46 Sy1 AGN at $0.003 < z < 0.2$.

In Figure 2.2, we present the distributions of *Swift*/BAT fluxes, luminosities and redshifts for both our sample and the Sy1 classified sources from the *Swift*/BAT 70-month catalog. We find that our sample is statistically representative of the Sy1 population from the *Swift*/BAT 70-month catalog, with the mean and median values overlapping between our sample and the parent *Swift*/BAT sample. We further applied a two-sample Kolmogorov-Smirnov test and found the K-S test statistic to be 0.1 or lower, and the p-value above 60 % for all three distributions, thus confirming that the distributions are consistent between our sample and the larger *Swift*/BAT sample of Sy1s.

NuSTAR Observations and Data Reduction

Roughly once per week since its start of science operations in 2013, the *NuSTAR* satellite has been obtaining ~ 20 ks observations in the 3–79 keV band of AGN selected from the *Swift*/BAT 70-month hard X-ray catalog (Baumgartner et al., 2013). We performed reduction of raw event data from both *NuSTAR* modules, FPMA and FPMB (Harrison et al., 2013), using the *NuSTAR* Data Analysis Software (NuSTARDAS, version 1.2.1), distributed by the NASA High Energy Astrophysics Archive Research Center (HEASARC) within the HEASOFT package, version 6.16. We took instrumental responses from the *NuSTAR* calibration database (CALDB), version 20160502. Raw event data were cleaned and filtered for South Atlantic

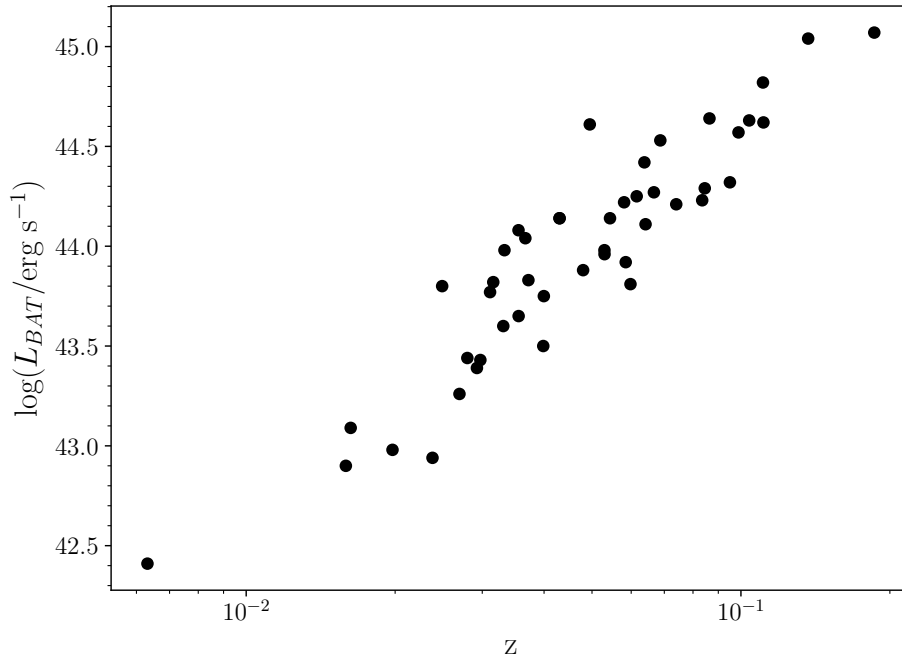


Figure 2.1: Redshift-luminosity distribution for *NuSTAR*-observed Sy1 AGN selected from the *Swift*/BAT 70-month hard X-ray catalogue.

Anomaly (SAA) passages using the `nupipeline` module. We extracted source and background energy spectra from the calibrated and cleaned event files using the `nuproducts` module. Detailed information on these data reduction procedures can be found in the *NuSTAR* Data Analysis Software Guide (Perri et al., 2017). An extraction radius of 30 was used for both the source and background regions. We extracted the background spectrum from source-free regions of the image, and away from the outer edges of the field of view, which have systematically higher background. The spectral files were rebinned using the HEASOFT task `grppha` to give a minimum of 20 photon counts per bin. For multiple observations of the same source, we coadded spectra using the HEASOFT task `addspec`.

Spectral Modeling

We performed spectral modeling of the *NuSTAR* data in the 3–79 keV band for each source in our sample using XSPEC v12.8.2 (Arnaud, 1996). We used χ^2 statistics for all model fitting and error estimation. We adopted cross sections from Verner et al. (1996) and solar abundances from Wilms et al. (2000). In all our modeling, we include a cross-correlation constant between FPMA and FPMB to account for slight differences in calibration (Madsen et al., 2015)

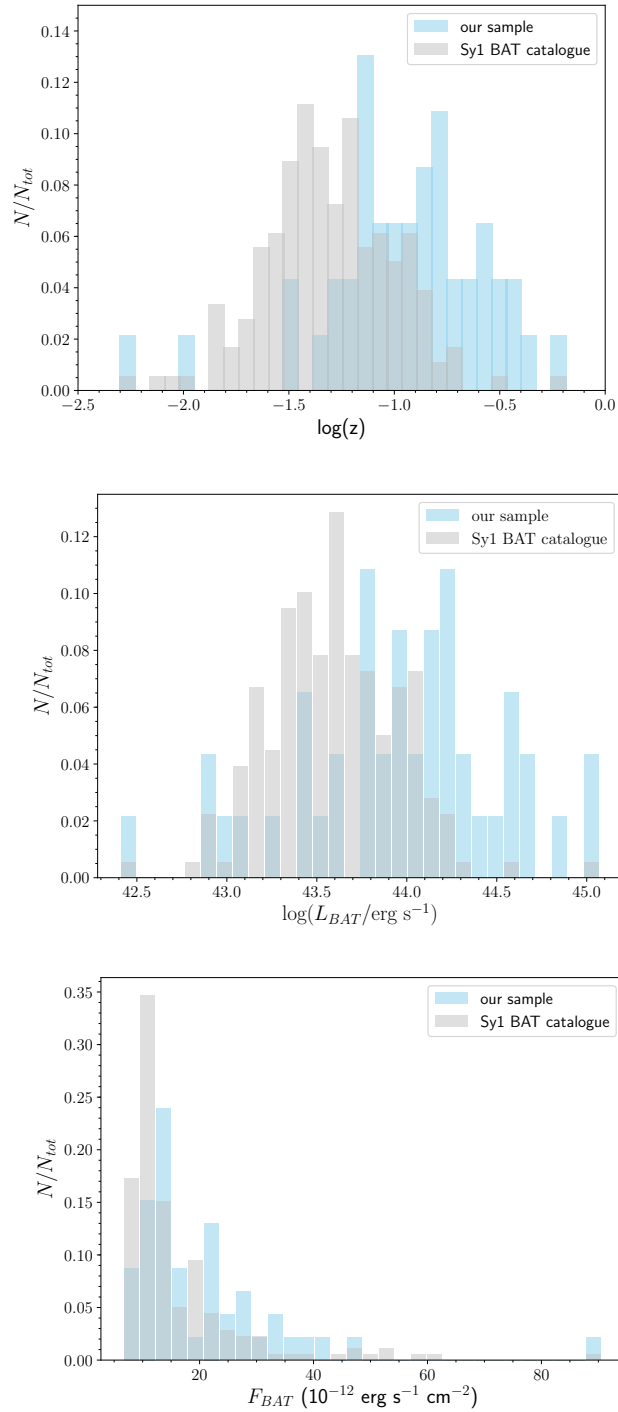


Figure 2.2: Distributions of redshifts, *Swift*/BAT 70-month X-ray catalogue luminosities and fluxes for both our sample and the Sy1 classified sources from the *Swift*/BAT catalogue. For clarity, sources with $L_{BAT} < 10^{40} \text{ erg s}^{-1}$ and $F_{BAT} > 1 \times 10^{-10} \text{ erg s}^{-1} \text{ cm}^{-2}$ were omitted from the plots.

We fit each spectrum with an absorbed power-law model with a high-energy cutoff, E_{cut} . The slope of the power-law continuum is characterized by the photon index, Γ . It is assumed that the intrinsic continuum intensity is proportional to $E^{-\Gamma} \exp(-E/E_{\text{cut}})$. In XSPEC notation, the model used is `TBabs × zwabs × cutoffpl`, where the component `TBabs` models Galactic absorption, which is fixed to a typical Galactic column density of $7.6 \times 10^{21} \text{ cm}^{-2}$ (Kalberla et al., 2005). We found that freezing the Galactic column density did not have any significant effect on the fit results, as spectral modeling over the hard X-ray band is relatively insensitive to this parameter. The redshifted component `zwabs` accounts for absorption by the host galaxy.

Where an Fe $K\alpha$ emission line feature was observed in the spectra at 6.4 keV, we added an additive `zgauss` Gaussian line component to the absorbed power-law model. We note that two objects out of our sample required fitting with an Fe $K\alpha$ line: Mrk 595 and RBS 1037. In addition, we test for the presence of spectral features due to reprocessing by adding a `pexrav` component (Magdziarz & Zdziarski, 1995). We fixed elemental abundances to solar and kept the inclination angle fixed at the default value of 60. We found that the reduced χ^2 values and best-fit parameters from modeling with `pexrav` were similar to those from fitting an absorbed cutoff power-law for the majority of the sources in our sample, indicating that the addition of a reflection component does not significantly modify fit results and thus is not required by the data. Furthermore, we found that the null hypothesis probability exceeds 50 % for many of our sources when fitting with an absorbed cutoff power-law; we found the mean null hypothesis probability of our sample to be 43 %. We note that we chose a reflection model for one source (2MASX J19301380+3410495) due to best-fit parameters such as the photon index being more physically reasonable compared to the absorbed cutoff power-law model. We also note that the reduced χ^2 for Mrk 9 is relatively high due to increased scatter in the data near ~ 10 keV and 30 keV, which do not correspond to any known physical features. We summarize some of the key best-fit spectral parameters for our sample in Table 2.3 of the appendix. We did not find any sources in our sample with significant line-of-sight absorption ($> 5 \times 10^{23} \text{ cm}^{-2}$), with most sources having hydrogen column densities constrained to be $< 10^{22} \text{ cm}^{-2}$. Figure 2.3 presents an example *NuSTAR* spectrum for a potential low-cutoff candidate in our sample, 2MASX J19301380+3410495, for which we measured E_{cut} to be 23_{-9}^{+29} keV.

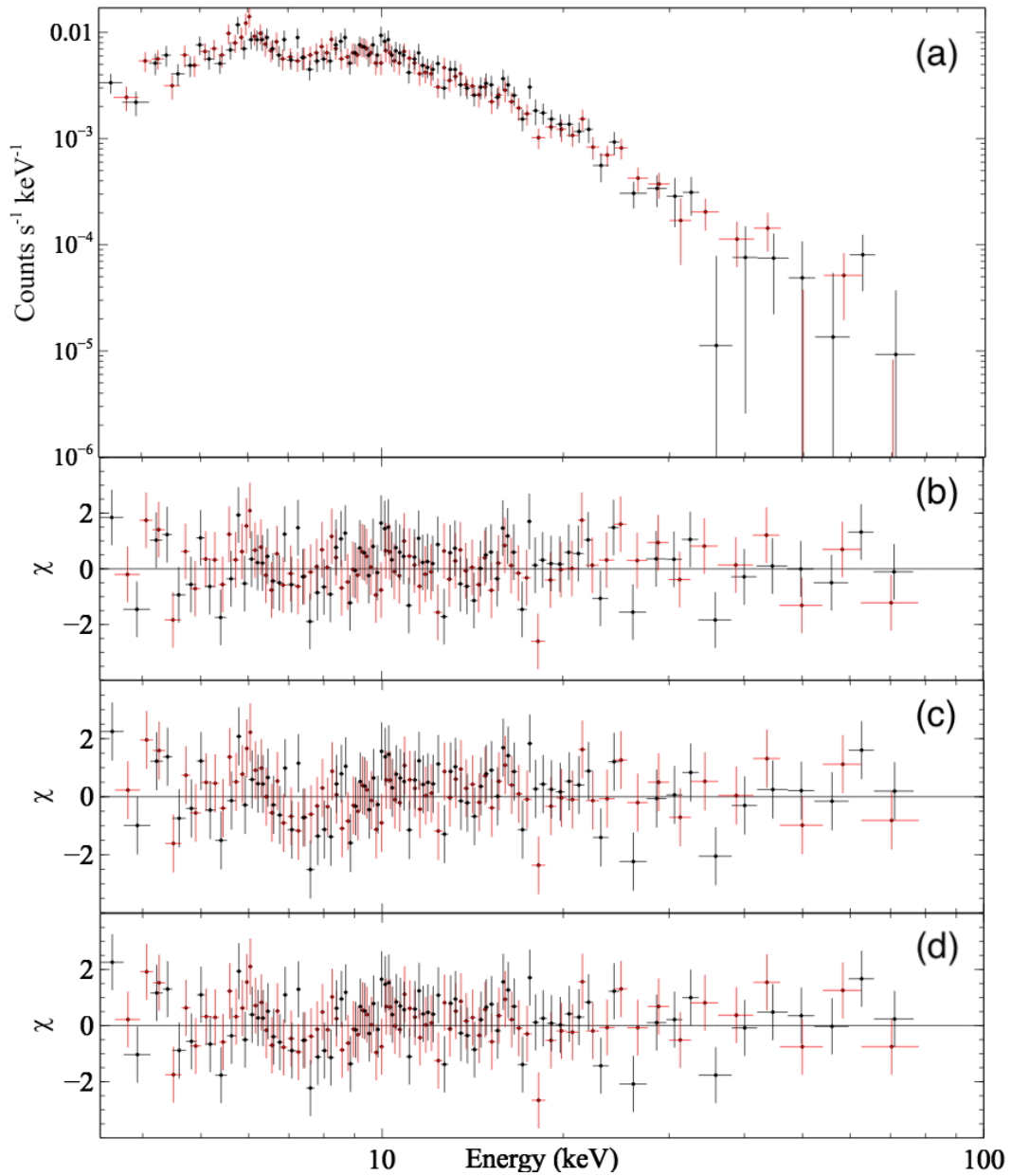


Figure 2.3: *NuSTAR* hard X-ray spectrum of a candidate low cutoff AGN 2MASX J19301380+3410495 (a), alongside fit residuals for (b) an absorbed power-law model ($\chi^2/\text{dof} = 155.1/161$), (c) absorbed power-law model with a high-energy cutoff ($\chi^2/\text{dof} = 144.4/160$), and (d) absorbed cutoff power-law with reflection modeled via *pexrav* ($\chi^2/\text{dof} = 138/160$). Black points correspond to FPMA data while red points in red correspond to FPMB.

2.3 Results and Discussion

In this section, we present limits on the high-energy cutoff, E_{cut} , found from spectral modeling of our sample. We then present the location of our sources on the $\theta - l$ plane for AGN coronae, and discuss the implications of sources with low values of E_{cut} on the heating and cooling mechanisms operating in the corona.

Cutoff Constraints

The distribution of lower limits on the high energy cutoff for our sample is presented in Figure 2.4. The histogram shows a number of AGN with lower limits on E_{cut} below 100 keV. Typical values of E_{cut} for AGN generally range from ~ 100 keV to 300 keV (Dadina, 2007; Malizia et al., 2014; Ricci et al., 2017b); we note that Gilli et al. (2007) comment that the mean value of E_{cut} for AGN must not exceed several hundred keV, in order to avoid overproducing the cosmic X-ray background above 100 keV.

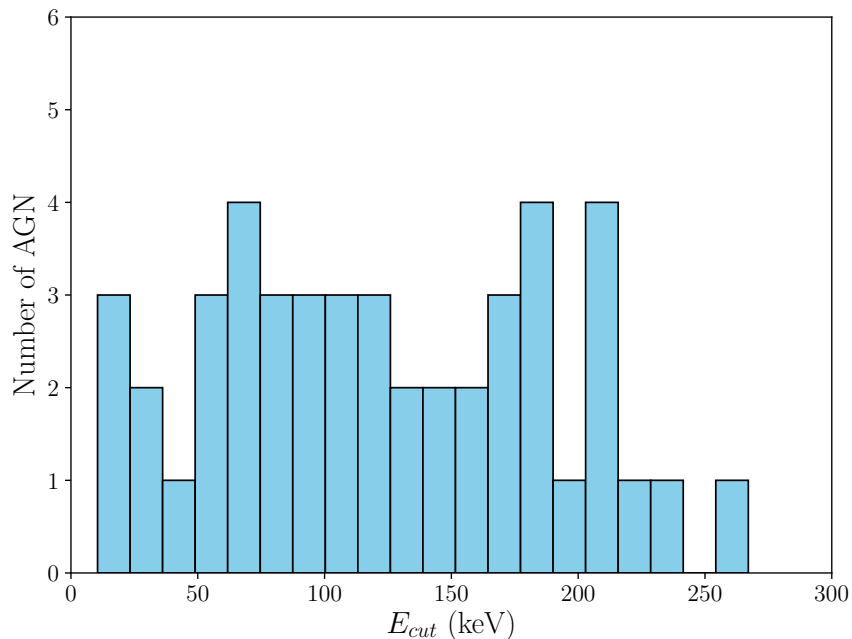


Figure 2.4: Distribution of lower limits on E_{cut} for our Sy1 AGN sample from modeling *NuSTAR* data.

Despite the fact that the quality of *NuSTAR* data in the hard X-ray band exceeds any previous observations of our targets, the cutoff power-law model does still display a degree of degeneracy in the derived photon index (Γ) and E_{cut} . In order to verify that our constraints on E_{cut} are physically reasonable, in Figure 2.5 we compare our derived Γ and E_{cut} values to curves of constant optical depth in the $E_{\text{cut}}-\Gamma$ parameter

space. The purple line in Figure 2.5 corresponds to theoretical constraints from Petrucci et al. (2001) for an optical depth $\tau = 6$. We use the relationship derived for a slab geometry of the corona by Petrucci et al. (2001) to calculate the optical depth as a function of Γ and E_{cut} :

$$\Gamma = \sqrt{\frac{9}{4} + \frac{511 \text{ keV}}{\tau k T_e (1 + \tau/3)}} - \frac{1}{2}. \quad (2.2)$$

AGN coronae are typically thought to be optically thin ($\tau < 1$) (Zdziarski, 1985; Stern et al., 1995), though some have been constrained to $\tau \sim 3$ based on high-quality *NuSTAR* data (e.g., Baloković et al., 2015; Tortosa et al., 2017; Kara et al., 2017). Combinations of Γ and E_{cut} that correspond to $\tau > 6$ can be considered to result from a degeneracy between model parameters and therefore are unphysical. With this particular assumption, we suspect that for 3 targets our results may be unrealistic; if, for example, $\tau < 10$ is chosen, then no targets fall in this category. However, sources lying near or below the line with $\tau = 6$ were not removed from our sample, as the limited *NuSTAR* data quality with a short, 20 ks exposure does not rule out physically reasonable values of the photon index.

We investigate the presence of model degeneracies in the sources with the lowest measured E_{cut} constraints (2MASX J19301380+3410495 & 1RXS J034704.9-302409) by exploring the $E_{\text{cut}}-\Gamma$ parameter space in XSPEC. Figure 2.6 shows the contour plots of the photon index against the high-energy cutoff for these sources. Whilst there is some degree of degeneracy between these two parameters, the value of E_{cut} is constrained to low values over the range of physically reasonable photon index values at the 68 % confidence level.

The $\theta - l$ Plane

In constructing the observational $\theta - l$ plane, we convert from E_{cut} to the coronal temperature using $k_B T_e = E_{\text{cut}}/2$ (Petrucci et al., 2001). In calculating l , we assume a conservative value of $10R_g$ for the coronal radius R , as adopted in Fabian et al. (2015), as the majority of the sources in our sample lack the required X-ray reflection modeling or reverberation measurements to place constraints on coronal size. We estimated the source luminosity L , from the flux in the 0.1–200 keV band, which was extrapolated from the applied spectral model. We convert the unabsorbed 0.1–200 keV flux obtained from spectral modeling to luminosity using luminosity distance

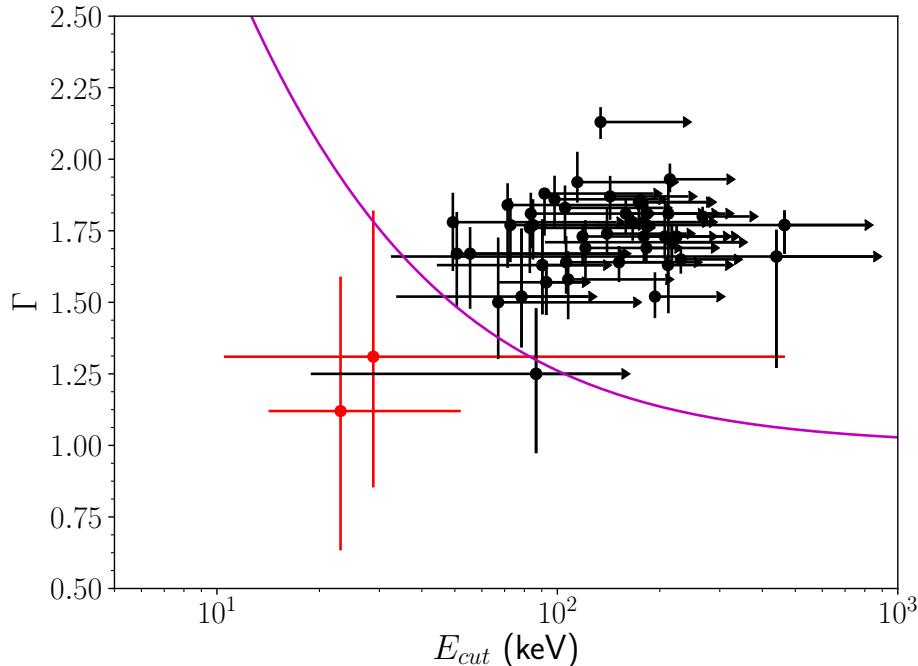


Figure 2.5: E_{cut} vs photon index Γ for our sample. Points in red denote candidate sources with low coronal high-energy cutoffs for which both upper and lower limits on E_{cut} were measured. The purple line corresponds to theoretical constraints from Petrucci et al. (2001) for $\tau = 6$.

values from NED. Black hole mass estimates, where available, were taken from Koss et al. (2017). The values of M_{BH} used in Koss et al. (2017) were obtained from a combination of broad Balmer emission line measurements, direct techniques such as X-ray reverberation mapping, and the $M_{BH} - \sigma_*$ relation of Kormendy & Ho (2013). We have black hole mass measurements obtained from the literature for 34 of the 46 sources in our sample. For sources with no published black hole mass, we use the median black hole mass of the Sy 1–1.5 AGN in the BAT AGN Spectroscopic Survey (BASS) (Koss et al., 2017), $\log(M_{BH}/M_{\odot}) = 7.97 \pm 0.52$.

We note that the precise location of AGN on the $\theta - l$ plane is dependent on general relativistic effects, such as gravitational redshift and light bending. Processes such as light bending introduce inclination-dependent corrections to l . These corrections depend on the geometry of the corona, which is currently highly uncertain. Therefore, due to the large uncertainties associated with model-based relativistic corrections, we do not include general relativistic effects here.

Figure 2.7 presents the location of our sources on the $\theta - l$ plane, in addition to theoretical pair lines for different coronal geometries. Runaway pair production

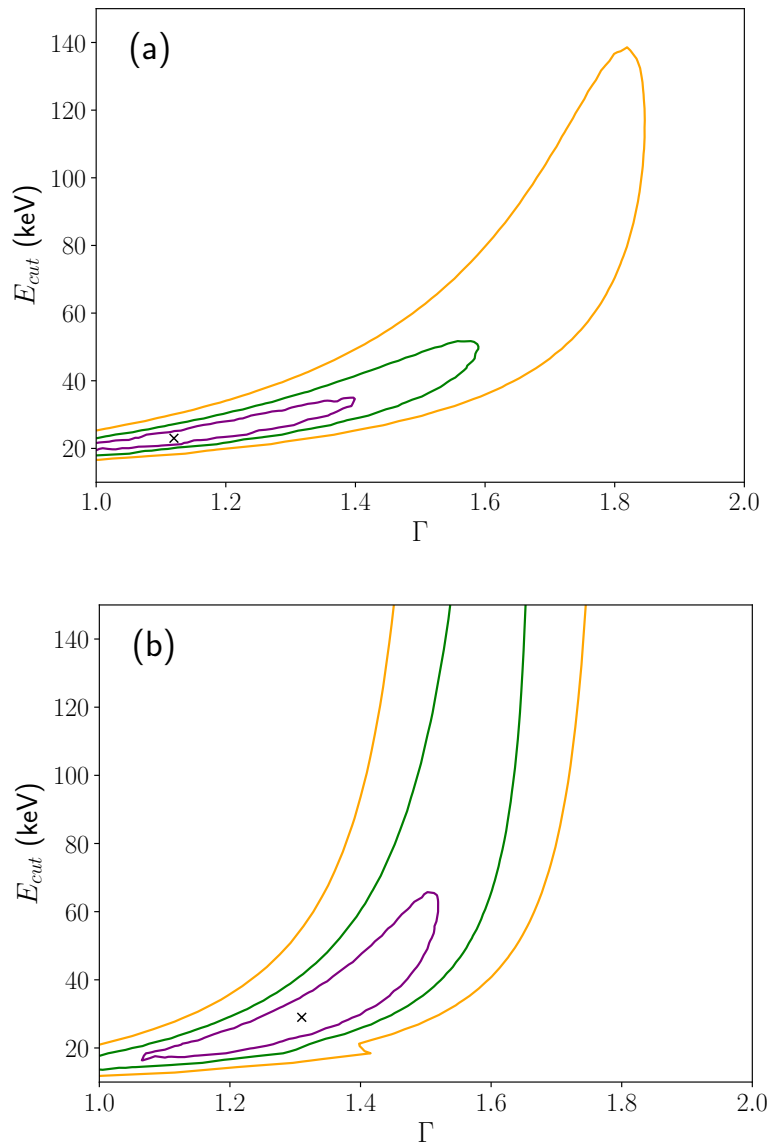


Figure 2.6: E_{cut} - Γ contour plots for *NuSTAR* observations of the candidate low cutoff Sy1s (a) 2MASX J19301380+3410495 (b) 1RXS J034704.9-302409. The solid purple, green, and yellow contours correspond to the 68, 90, and 99 % confidence levels, respectively. The black cross represents the best fit values of the parameters from applying the relevant model given in Table 2.3.

occurs to the right of the pair lines, as described in the introduction. Modeling the corona as an isolated electron cloud, Svensson (1984) estimated the pair production line to have the analytical form

$$l \sim 10\theta^{5/2}e^{1/\theta}. \quad (2.3)$$

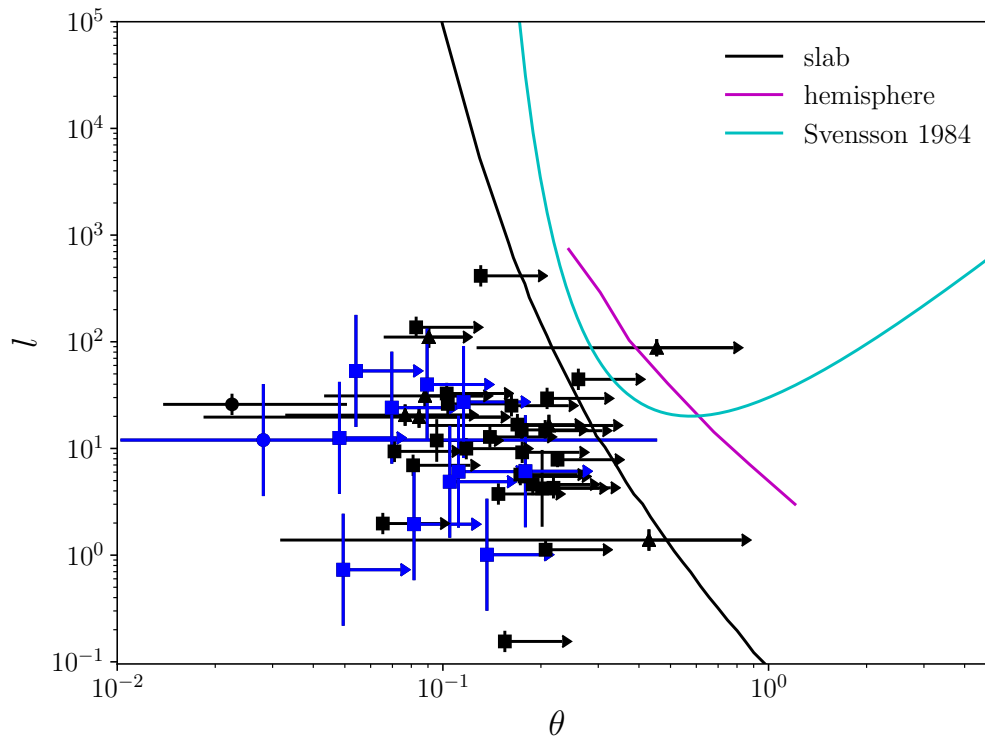


Figure 2.7: The $\theta - l$ plane for *NuSTAR*-observed Sy1 AGN. Solid lines correspond to pair lines for different coronal geometries. Circled points are candidate low cutoff sources for which both upper and lower limits on E_{cut} were measured. Triangles denote sources with a best-fit value and lower limit on E_{cut} . Squares denote sources with only lower limits on E_{cut} . Blue points indicate sources for which the black hole mass was taken to be the median black hole mass of the type 1 AGN in the BAT AGN Spectroscopic Survey (BASS) (Koss et al., 2017).

Stern et al. (1995) also computed the pair balance line for a slab and hemispherical corona, respectively, located above a reflecting accretion disk. The solid black and purple lines in Figure 2.7 correspond to these geometries.

Our results show that most of the AGN coronae in our sample are clustered near the lines for runaway pair production, similar to the results found by Fabian et al. (2015) for *NuSTAR*-observed AGN and black hole binaries (BHB). The pair lines thus appear to correspond to a physical boundary, constraining sources to that region. A few AGN are located away from the pair line boundary, hinting at low coronal temperatures. Note that we have assumed that the corona is homogeneous and at a single temperature, whereas in reality there may be a range of temperatures. This may result in a mean temperature at a lower value due to Compton cooling (Fabian et al., 2015).

Recent detections of low coronal cutoffs have been made within the *NuSTAR* band, such as Tortosa et al. (2017), Kara et al. (2017), and Xu et al. (2017). For example, Kara et al. (2017) measured $T_e = 15 \pm 2$ keV for the narrow-line Sy1 Ark 564, making it one of the lowest temperature coronae observed by *NuSTAR* to date. Multiple explanations have been proposed for the origin of low temperature coronae. In the case of an AGN accreting close to the Eddington limit, the stronger radiation field may enhance Compton cooling in comparison with sub-Eddington Seyferts (Kara et al., 2017). For sources accreting well below the Eddington limit, the relatively low coronal temperatures may be attributed to highly effective cooling in some AGN due to, e.g., high spin and the resulting higher seed photon temperature. Low temperatures may also arise from particularly weak coronal heating mechanisms, or more effective cooling due to multiple scatterings in a corona with high optical depth (e.g., Tortosa et al., 2017). Naively, when the optical depth in the corona exceeds unity, multiple inverse Compton scatterings transfer a proportionally higher fraction of the stored thermal energy to coronal luminosity. However, coronae are complex systems, and many coupled physical processes determine the electron temperature.

Another possibility is that the corona consists of a hybridized plasma, containing both thermal and non-thermal particles (e.g., Zdziarski et al., 1993; Ghisellini et al., 1993; Fabian et al., 2017). In such a system, the corona is highly magnetized and compact, and thus heating and cooling are so intense that electrons do not have time to thermalize before they are cooled by inverse Compton scattering. The presence of only a small fraction of non-thermal electrons with energies above 1 MeV can result in runaway pair production. The cooled electron-positron pairs may redistribute their available energy, thereby reducing the mean energy per particle and decreasing the coronal temperature. Such cooling would produce a hard non-thermal tail and an annihilation feature at 511 keV. Hard X-ray data of very high quality are necessary to distinguish between a hybrid, pair-dominated plasma and cooler, fully thermal plasma incapable of pair production.

2.4 Future Observations

The E_{cut} constraints presented here are based on snapshot ~ 20 ks *NuSTAR* observations of a sample of bright Sy1 galaxies, and identified several sources which potentially have high-energy cutoffs within the *NuSTAR* band (i.e., 3–79 keV). Future work will involve performing longer exposure *NuSTAR* observations of AGN from our sample that display hints of a low coronal cutoff, which will aid in removing model degeneracies and more tightly constrain E_{cut} , in order to determine

Table 2.1: Mean values of the high-energy cutoff, its lower and upper limits from simulated *NuSTAR* spectra, for *Swift*/BAT-selected Sy1 AGN

Name	Exposure Time (ks)	E_{cut} (keV)	E_{cut} lower limit (keV)	E_{cut} upper limit (keV)
1RXS J034704.9-302409	50	92.7	17.1	118.8
	100	54.6	19.2	111.8
2MASX J19301380+3410495	50	21.4	15.7	33.0
	100	20.7	16.7	27.0
Mrk 1393	50	189.0	43.5	191.7
	100	155.0	45.0	199.7
SDSS J104326d47+110524.2	50	170.4	46.3	203.2
	100	134.1	52.1	206.5
UGC 06728	50	162.6	59.4	234.8
	100	127.5	67.6	222.8

the coronal temperature. In choosing AGN from our sample for longer exposure *NuSTAR* observations, we performed 5000 simulations of the spectra of candidate low E_{cut} AGN from our sample in XSPEC, for exposure times of 50 ks and 100 ks. From the simulated spectra, we plotted distributions of the best-fit value of E_{cut} found from applying an absorbed cutoff power-law model, in addition to lower limits and upper limits on E_{cut} . The plots in Figure 8 show distributions of values of E_{cut} for one such candidate low cutoff source, 2MASX J19301380+3410495. Table 2.1 summarizes the mean values of E_{cut} and its lower and upper limits obtained from our simulations for some candidate low cutoff AGN in our sample.

The simulation results show that the distributions peak at low values of E_{cut} , and at similar values for both a 50 ks and 100 ks exposure. We conclude from our results that a 50 ks exposure should be sufficient to constrain the high-energy cutoff in our sample of candidate low cutoff AGN.

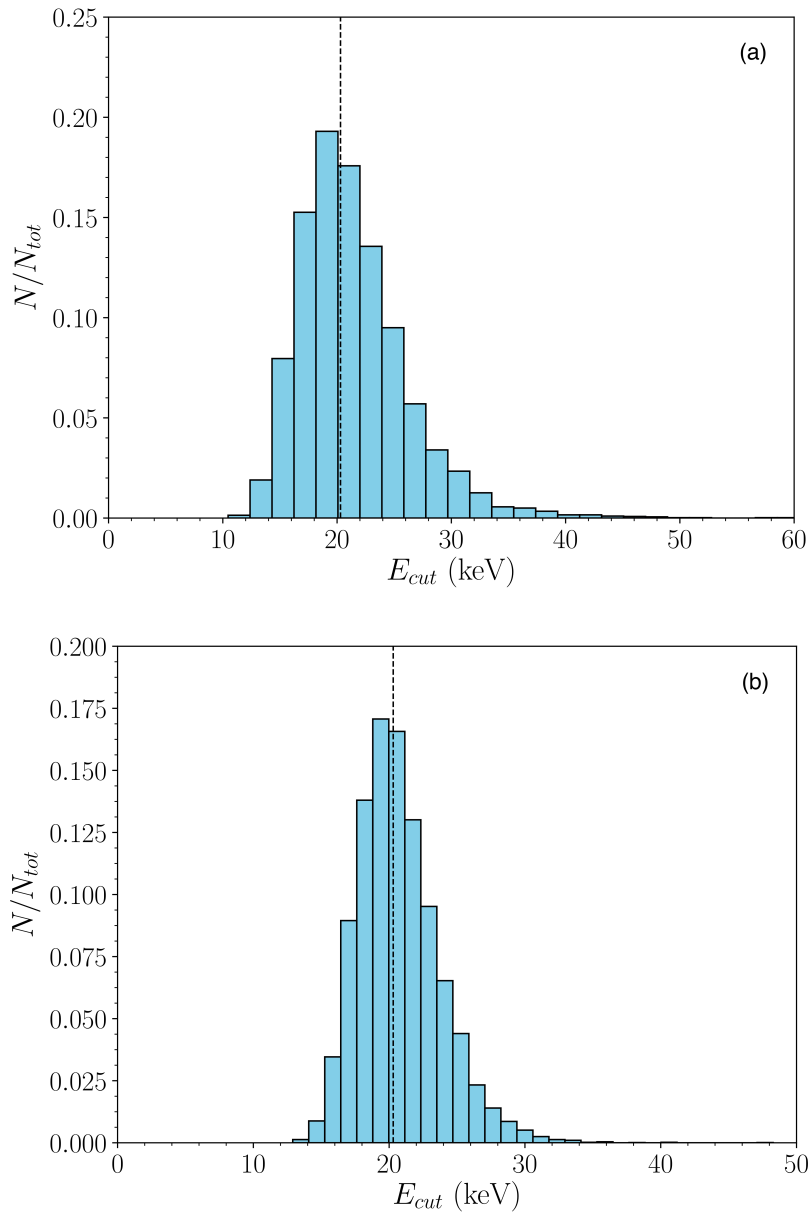


Figure 2.8: Distributions of E_{cut} values for 5000 simulations of the *NuSTAR* spectrum of a candidate low cutoff AGN, 2MASX J19301380+3410495. Dotted lines denote the input E_{cut} value assumed for simulated spectra. Simulations were performed for exposure times of (a) 50 ks and (b) 100 ks.

2.5 Summary

In this work, we have investigated the coronal properties of a sample of *Swift*/BAT selected Seyfert 1 AGN that have been observed with *NuSTAR*. We individually modeled the *NuSTAR* spectra of all sources in our sample and searched for sources with hints of low coronal cutoffs, observable within the *NuSTAR* band. We mapped

out the location of the sources in our sample on the compactness-temperature diagram for AGN coronae, and found that the majority of sources lie near the boundary for runaway pair production. The pair production line corresponds to a physical boundary, constraining AGN to that region. A few AGN located away from the pair lines may possess low coronal temperatures; deeper 50 ks *NuSTAR* observations will be performed of these sources to constrain the coronal temperature and optical depth. The detection of low coronal cutoffs may be explained via scenarios such as a strong radiation field, large optical depth, or a hybrid pair-dominated plasma. Further computations with hybrid plasma models, taking into account general relativistic effects, will help elucidate in more detail the heating and cooling mechanisms operating in the corona.

2.6 Acknowledgements

We would like to thank the referee for their helpful comments, which helped improve the final version of the manuscript. We have made use of data from the *NuSTAR* mission, a project led by the California Institute of Technology, managed by the Jet Propulsion Laboratory, and funded by the National Aeronautics and Space Administration. We thank the *NuSTAR* Operations, Software and Calibration teams for support with the execution and analysis of these observations. This research has made use of the *NuSTAR* Data Analysis Software (NuSTARDAS) jointly developed by the ASI Science Data Center (ASDC, Italy) and the California Institute of Technology (USA). M. Baloković acknowledges support from NASA Headquarters under the NASA Earth and Space Science Fellowship Program (grant NNX14AQ07H) and support from the Black Hole Initiative at Harvard University, through the grant from the John Templeton Foundation.

2.7 Appendix

Table 2.2: *NuSTAR* Observation Details for *Swift*/BAT–selected Sy1 AGN

Name	<i>Swift</i> /BAT ID	Observation ID	Observation Date	Exposure Time (ks)	Total Counts
1RXS J034704.9-302409	SWIFT J0347.0-3027	60061039002	2013-03-15	6.4	13.5
		60061039004	2013-03-24	12.7	20.4
		60061039006	2013-04-02	9.5	21.9
1RXS J174538.1+290823	SWIFT J1745.4+2906	60160674002	2014-12-09	20.3	2233
1RXS J213445.2-272551	SWIFT J2134.9-2729	60061306002	2013-10-22	19.8	2178
2MASS J19334715+3254259	SWIFT J1933.9+3258	60160714002	2016-05-31	12.6	3024
2MASX J04372814-4711298	SWIFT J0437.4-4713	60160197002	2015-12-09	20.0	1500
2MASX J12313717-4758019	SWIFT J1232.0-4802	60160498002	2016-08-21	19.3	1718
2MASX J15144217-8123377	SWIFT J1513.8-8125	60061263002	2013-08-06	13.3	1011
2MASX J15295830-1300397	SWIFT J1530.0-1300	60160617002	2017-02-14	24.2	2130
2MASX J19301380+3410495	SWIFT J1930.5+3414	60160713002	2016-07-19	20.5	1701
2MASX J19380437-5109497	SWIFT J1938.1-5108	60160716002	2016-07-15	21.8	2834
2MASX J20005575-1810274	SWIFT J2001.0-1811	60061295002	2016-10-25	21.9	1367
2MASXi J1802473-145454	SWIFT J1802.8-1455	60160680002	2016-05-01	20.0	6800
		3C 227	SWIFT J0947.7+0726	60061329002	2014-02-20
		60061329004	2014-02-26	12.1	188
4C +18.51	SWIFT J1742.2+1833	60160672002	2017-03-27	22.5	1080
ESO 438-G009	SWIFT J1110.6-2832	60160423002	2015-02-01	21.7	1302
Fairall 1146	SWIFT J0838.4-3557	60061082002	2014-07-27	21.3	4473
Fairall 1203	SWIFT J0001.6-7701	60160002002	2015-04-11	34.1	1739
[HB89] 0241+622	SWIFT J0244.8+6227	60160125002	2016-07-31	23.4	9126
IGR J14471-6414	SWIFT J1446.7-6416	60061257002	2013-05-28	15.0	975
IGR J14552-5133	SWIFT J1454.9-5133	60061259002	2013-09-19	21.9	2190
IRAS 04392-2713	SWIFT J0441.2-2704	60160201002	2015-12-20	19.5	2145
LCRSB 232242.2-384320	SWIFT J2325.5-3827	60160826002	2016-07-08	22.5	495
Mrk 9	SWIFT J0736.9+5846	60061326002	2013-10-29	23.3	1142
Mrk 376	SWIFT J0714.3+4541	60160288002	2015-04-07	24.2	1791
Mrk 595	SWIFT J0241.6+0711	60160119002	2017-01-18	21.3	873
Mrk 732	SWIFT J1113.6+0936	60061208002	2013-06-11	26.3	3419
Mrk 739E	SWIFT J1136.0+2132	60260008002	2017-03-16	18.5	1277
Mrk 813	SWIFT J1427.5+1949	60160583002	2017-01-23	24.6	2952
Mrk 817	SWIFT J1436.4+5846	60160590002	2015-07-25	21.9	2847
Mrk 841	SWIFT J1504.2+1025	60101023002	2015-07-14	23.4	6084
Mrk 1018	SWIFT J0206.2-0019	60160087002	2016-02-10	21.6	583
Mrk 1044	SWIFT J0230.2-0900	60160109002	2016-02-08	21.7	2821
Mrk 1310	SWIFT J1201.2-0341	60160465002	2016-06-17	21.1	2743
Mrk 1393	SWIFT J1508.8-0013	60160607002	2016-01-19	22.4	896
NGC 0985	SWIFT J0234.6-0848	60061025002	2013-08-11	13.9	2363
PG 0804+761	SWIFT J0810.9+7602	60160322002	2016-04-02	17.3	1903
PKS 0558-504	SWIFT J0559.8-5028	60160254002	2016-11-19	21.0	2940
RBS 0295	SWIFT J0214.9-6432	60061021002	2017-01-14	23.3	1887
RBS 0770	SWIFT J0923.7+2255	60061092002	2012-12-26	18.9	6426
RBS 1037	SWIFT J1149.3-0414	60061215002	2017-02-02	40.7	2198
RBS 1125	SWIFT J1232.1+2009	60061229002	2016-07-28	20.0	1280
SBS 1136+594	SWIFT J1139.1+5913	60160443002	2014-12-26	23.5	3760
SDSS J104326.47+110524.2	SWIFT J1043.4+1105	60160406002	2016-06-14	20.1	137
UGC 06728	SWIFT J1143.7+7942	60160450002	2016-07-10	22.6	2486
UM 614	SWIFT J1349.7+0209	60160560002	2015-03-31	18.2	2002
WKK 1263	SWIFT J1241.6-5748	60160510002	2016-04-27	16.4	7872

Table 2.3: Redshifts, black hole masses, and best-fit spectral parameters from fitting *NuSTAR* data for our *Swift*/BAT-selected Sy1 AGN sample

Source	Redshift	$\log(M_{\text{BH}}/M_{\odot})^A$	Γ	E_{cut} (keV)	$F_{0.1-200}^B$ $10^{-12} \text{ erg cm}^{-2} \text{ s}^{-1}$	χ^2/dof	Model ^C
1RXS J034704.9-302409*	0.095	7.97±0.52	1.31 ^{+0.51} _{-0.46}	29 ⁺⁴³⁷ ₋₁₈	1.12 ^{+0.38} _{-0.10}	50.9/50	1
1RXS J174538.1+290823	0.111	8.82±0.10	1.76 ^{+0.06} _{-0.16}	≥ 83	8.59 ^{+0.91} _{-0.89}	181.5/187	1
1RXS J213445.2-272551	0.067	6.99±0.10	1.77 ^{+0.09} _{-0.12}	≥ 85	7.62 ^{+0.73} _{-0.38}	155.8/175	1
2MASS J19334715+3254259	0.057	7.88±0.10	1.78 ^{+0.04} _{-0.06}	≥ 166	15.3 ^{+0.6} _{-0.6}	236.3/225	1
2MASX J04372814-4711298*	0.053	7.97±0.52	1.92 ^{+0.11} _{-0.07}	≥ 114	5.08 ^{+0.56} _{-0.25}	147.5/123	1
2MASX J12313717-4758019*	0.028	7.97±0.52	1.81 ^{+0.07} _{-0.12}	≥ 84	5.88 ^{+0.75} _{-0.46}	107.8/139	1
2MASX J15144217-8123377	0.068	8.96±0.10	1.66 ^{+0.09} _{-0.39}	≥ 32	6.67 ^{+0.94} _{-1.24}	95.3/86	1
2MASX J15295830-1300397*	0.104	7.97±0.52	1.73 ^{+0.04} _{-0.10}	≥ 119	5.49 ^{+0.25} _{-0.25}	172.4/170	1
2MASX J19301380+3410495	0.063	8.15±0.10	1.12 ^{+0.47} _{-0.49}	23 ⁺²⁹ ₋₉	22.9 ^{+5.98} _{-3.77}	138/160	2
2MASX J19380437-5109497	0.040	7.23±0.10	1.83 ^{+0.08} _{-0.12}	≥ 105	9.03 ^{+0.78} _{-0.65}	214.2/215	1
2MASX J20005575-1810274	0.037	8.07±0.36	1.73 ^{+0.08} _{-0.08}	≥ 207	9.62 ^{+0.79} _{-0.76}	285.1/250	1
2MASXi J1802473-145454	0.003	7.76±0.10	1.81 ^{+0.05} _{-0.07}	≥ 159	23.9 ^{+1.3} _{-1.2}	466.3/451	1
3C 227	0.086	8.61±0.10	1.63 ^{+0.16} _{-0.17}	≥ 44	11.7 ^{+1.1} _{-0.9}	331/347	1
4C +18.51*	0.186	7.97±0.52	1.67 ^{+0.09} _{-0.19}	≥ 55	3.04 ^{+0.34} _{-0.20}	73.2/100	1
ESO 438-G009*	0.024	7.97±0.52	1.74 ^{+0.09} _{-0.07}	≥ 140	3.95 ^{+0.23} _{-0.23}	92.3/113	1
Fairall 1146*	0.031	7.97±0.52	1.81 ^{+0.04} _{-0.05}	≥ 184	14.1 ^{+0.9} _{-0.5}	365.9/326	1
Fairall 1203*	0.058	7.97±0.52	1.58 ^{+0.11} _{-0.07}	≥ 108	3.37 ^{+0.38} _{-0.33}	139.4/150	1
[HB89] 0241+622	0.044	8.09±0.10	1.63 ^{+0.04} _{-0.05}	≥ 211	24.1 ^{+1.0} _{-0.4}	631.1/565	1
IGR J14471-6414	0.053	7.70±0.10	1.77 ^{+0.09} _{-0.13}	≥ 73	4.08 ^{+0.51} _{-0.28}	84.3/82	1
IGR J14552-5133	0.016	6.86±0.10	1.73 ^{+0.03} _{-0.09}	≥ 180	6.43 ^{+0.35} _{-0.25}	191.9/181	1
IRAS 04392-2713*	0.084	7.97±0.52	1.84 ^{+0.08} _{-0.22}	≥ 71	7.82 ^{+0.71} _{-0.44}	200.8/173	1
LCRSB 232242.2-384320*	0.036	7.97±0.52	1.67 ^{+0.14} _{-0.19}	≥ 51	1.44 ^{+0.23} _{-0.13}	50.9/46	1
Mrk 9	0.040	7.59±0.10	1.52 ^{+0.08} _{-0.08}	≥ 193	2.83 ^{+0.19} _{-0.18}	155.1/100	1
Mrk 376	0.056	8.17±0.10	1.64 ^{+0.06} _{-0.07}	≥ 152	4.38 ^{+0.37} _{-0.20}	170.3/147	1
Mrk 595	0.027	8.28±0.10	1.50 ^{+0.23} _{-0.20}	≥ 67	2.62 ^{+0.43} _{-0.33}	79.5/76	3
Mrk 732	0.029	7.23±0.10	1.85 ^{+0.07} _{-0.07}	≥ 173	7.95 ^{+0.31} _{-0.31}	269.6/258	1
Mrk 739E	0.030	7.14±0.10	1.87 ^{+0.07} _{-0.08}	≥ 143	4.80 ^{+0.30} _{-0.29}	113.1/106	1
Mrk 813	0.110	8.87±0.10	1.85 ^{+0.03} _{-0.10}	≥ 177	7.95 ^{+0.31} _{-0.31}	269.6/230	1
Mrk 817	0.031	7.59±0.07	1.65 ^{+0.04} _{-0.05}	≥ 230	7.82 ^{+0.36} _{-0.30}	263.1/214	1
Mrk 841	0.036	7.81±0.10	1.78 ^{+0.05} _{-0.06}	≥ 179	17.9 ^{+1.0} _{-0.7}	403.9/425	1
Mrk 1018	0.042	8.03±0.10	1.81 ^{+0.14} _{-0.35}	≥ 212	1.76 ^{+0.46} _{-0.24}	50.5/51	1
Mrk 1044	0.016	6.44±0.10	1.93 ^{+0.05} _{-0.05}	≥ 214	8.74 ^{+0.36} _{-0.36}	215.2/205	1
Mrk 1310	0.019	6.21±0.08	1.77 ^{+0.05} _{-0.10}	≥ 130	8.68 ^{+0.72} _{-0.32}	215/217	1
Mrk 1393	0.054	7.87±0.10	1.25 ^{+0.23} _{-0.28}	≥ 19	2.07 ^{+0.47} _{-0.21}	109.8/79	1
NGC 0985	0.043	7.92±0.10	1.69 ^{+0.10} _{-0.11}	≥ 121	11.7 ^{+1.1} _{-0.97}	187/195	1
PG 0804+761	0.100	8.73±0.05	1.69 ^{+0.07} _{-0.05}	≥ 183	6.85 ^{+0.34} _{-0.33}	126.3/155	1
PKS 0558-504	0.137	7.33±0.10	2.13 ^{+0.05} _{-0.06}	≥ 134	10.4 ^{+3.7} _{-0.39}	217.9/206	1
RBS 0295*	0.074	7.97±0.52	1.78 ^{+0.10} _{-0.17}	≥ 49	5.32 ^{+0.51} _{-0.42}	149.3/153	1
RBS 0770	0.032	7.34±0.10	1.80 ^{+0.03} _{-0.03}	≥ 267	22.8 ^{+0.59} _{-0.58}	400.3/434	1
RBS 1037*	0.084	7.97±0.52	1.88 ^{+0.01} _{-0.15}	≥ 92	3.77 ^{+0.17} _{-0.19}	180.6/185	3
RBS 1125	0.063	7.76±0.20	1.86 ^{+0.08} _{-0.10}	≥ 98	4.11 ^{+0.25} _{-0.25}	109.1/107	1
SBS 1136+594	0.060	7.98±0.10	1.71 ^{+0.06} _{-0.08}	≥ 92	10.6 ^{+0.4} _{-0.4}	295/285	1
SDSS J104326.47+110524.2	0.048	7.91±0.10	1.52 ^{+0.24} _{-0.18}	≥ 34	4.13 ^{+0.69} _{-0.23}	122/122	1
UGC 06728	0.006	5.66±0.10	1.57 ^{+0.07} _{-0.11}	≥ 67	6.96 ^{+0.30} _{-0.30}	227.3/208	1
UM 614	0.033	7.09±0.10	1.64 ^{+0.09} _{-0.11}	≥ 106	7.31 ^{+0.71} _{-0.50}	162.7/172	1
WKK 1263	0.024	8.25±0.10	1.73 ^{+0.04} _{-0.04}	≥ 224	31.6 ^{+1.5} _{-1.1}	470.3/503	1

Sources marked with an asterisk (*) correspond to AGN whose black hole masses were taken to be the median black hole mass of the type 1 AGN in the BAT AGN Spectroscopic Survey (BASS) (Koss et al., 2017).

^A Reference: Koss et al. (2017).

^B Unabsorbed 0.1 - 200 keV flux extrapolated from applied spectral model

^C Applied XSPEC models: (1) constant × TBabs × zwabs × cutoffpl

(2) constant × TBabs × zwabs × (cutoffpl + pexrav)

(3) constant × TBabs × zwabs × (cutoffpl + zgauss)

Chapter 3

THE BROADBAND X-RAY SPECTRUM OF THE
X-RAY-OBSCURED TYPE 1 AGN 2MASX J193013.80+341049.5

Nikita Kamraj, Mislav Baloković, Murray Brightman, Daniel Stern, Fiona A. Harrison, Roberto J. Assef, Michael J. Koss, Kyuseok Oh, and Dominic J. Walton. The Broadband X-Ray Spectrum of the X-Ray-obscured Type 1 AGN 2MASX J193013.80+341049.5. *The Astrophysical Journal*, 887(2):255, 2019. doi: 10.3847/1538-4357/ab57fc.

Nikita Kamraj¹, Mislav Baloković², Murray Brightman¹, Daniel Stern³, Fiona A. Harrison¹, Roberto J. Assef⁴, Michael J. Koss⁵, Kyuseok Oh^{6,7}, Dominic J. Walton⁸

¹Cahill Center for Astronomy and Astrophysics, California Institute of Technology, Pasadena, CA 91125, USA

²Yale Center for Astronomy & Astrophysics, 52 Hillhouse Avenue, New Haven, CT 06511, USA

³Jet Propulsion Laboratory, California Institute of Technology, Pasadena, CA 91109, USA

⁴Núcleo de Astronomía de la Facultad de Ingeniería y Ciencias, Universidad Diego Portales, Av. Ejército Libertador 441, Santiago, Chile

⁵Eureka Scientific Inc., 2452 Delmer St. Suite 100, Oakland, CA 94602, USA

⁶Department of Astronomy, Kyoto University, Oiwake-cho, Sakyo-ku, Kyoto 606-8502, Japan

⁷Korea Astronomy and Space Science Institute, 776 Daedeokdae-ro, Yuseong-gu, Daejeon 34055, Republic of Korea

⁸Institute of Astronomy, University of Cambridge, Madingley Road, Cambridge CB3 0HA, UK

Abstract

We present results from modeling the broadband X-ray spectrum of the Type 1 AGN 2MASX J193013.80+341049.5 using *NuSTAR*, *Swift* and archival *XMM-Newton* observations. We find this source to be highly X-ray obscured, with column densities exceeding 10^{23} cm^{-2} across all epochs of X-ray observations, spanning an 8 year period. However, the source exhibits prominent broad optical emission lines, consistent with an unobscured Type 1 AGN classification. We fit the X-ray spectra with both phenomenological reflection models and physically-motivated torus models to model the X-ray absorption. We examine the spectral energy distribution of this source and investigate some possible scenarios to explain the mismatch between X-ray and optical classifications. We compare the ratio of reddening to X-ray absorbing column density (E_{B-V}/N_{H}) and find that 2MASX J193013.80+341049.5

likely has a much lower dust-to-gas ratio relative to the Galactic ISM, suggesting that the Broad Line Region (BLR) itself could provide the source of extra X-ray obscuration, being composed of low-ionization, dust-free gas.

3.1 Introduction

Under the unified model of Active Galactic Nuclei (AGN) (Antonucci, 1993; Urry & Padovani, 1995), differences between Type 1 and Type 2 AGN arise solely from our line-of-sight viewing angle relative to a toroidal obscuring structure surrounding the central supermassive black hole (SMBH). The dusty molecular torus believed to be responsible for the obscuration seen in Type 2 AGN likely has a clumpy distribution, as evidenced from infrared interferometric observations (Tristram et al., 2007; López-Gonzaga et al., 2016) and short timescale variability of the line-of-sight column density in some AGN (e.g., Marinucci et al., 2016). The unified model, while simplistic, has been successful in explaining observations of radio jets, polar ionization cones, and polarization position angle (e.g., Evans et al., 1991; Storchi-Bergmann et al., 1992).

Optical classification of AGN is based on widths of observed emission lines. Type 1 AGN contain both broad ($\text{FWHM} \gtrsim 1000 \text{ km s}^{-1}$) and narrow emission lines whereas Type 2 AGN contain only narrow emission lines. In the unified picture, this is due to obscuration of the Broad Line Region (BLR), which is close to the central SMBH, by the molecular torus. Hence in Type 2 AGN, only emission from the Narrow Line Region (NLR) is observed, which is extended on kilo-parsec scales. In Type 1 AGN, the torus is viewed at angles such that the line of sight to the BLR is unobscured.

X-ray classification of AGN is typically based on measurements of the hydrogen column density (N_{H}). Neutral gas along our line of sight absorbs X-ray continuum photons, with the level of absorption dependent on the column density of gas. The approximate dividing line between unobscured, Type 1 AGN and obscured, Type 2 AGN is at $N_{\text{H}} = 10^{22} \text{ cm}^{-2}$ (Ricci et al., 2017b). Assuming the simple picture of a static obscuring torus surrounding the AGN is correct, then there should be agreement between optical and X-ray classifications.

The *Swift*/BAT survey comprises all sources detected by the all-sky 14–195 keV Burst Alert Telescope (BAT) instrument onboard the *Neil Gehrels Swift Observatory* (Gehrels et al., 2004; Oh et al., 2018), and provides a hard X-ray-selected sample of local AGN that is relatively unbiased to obscuration. The *Swift*/BAT sample therefore offers a unique opportunity to test the unified model of AGN. Within

Table 3.1: Details of the *NuSTAR* and *XMM-Newton* observations of 2MASX J193013.80+341049.5 considered in this work.

Mission	Observation ID	Observation Date	Exposure Time (ks)	Count rate (counts s ⁻¹)
<i>NuSTAR</i>	60160713002	2016-07-19	23.4	0.142
<i>NuSTAR</i>	60376001002	2017-10-10	55.4	0.120
<i>XMM-Newton</i>	0602840101	2009-05-16	16.9	0.288

Observed source count rates are in the 0.5–10 keV band for the *XMM-Newton* EPIC-pn detector and the 3–79 keV band for *NuSTAR* (FPMA).

the *Swift*/BAT sample, there is excellent agreement between the optical and X-ray classifications for $\sim 95\%$ of sources (Koss et al., 2017). However, there are a number of unusual sources in the *Swift*/BAT sample that show disagreement between their X-ray and optical classifications. Some narrow-line Type 2 AGN have been found to be X-ray unabsorbed and there is some debate about whether they represent a class of AGN lacking a BLR (Panessa & Bassani, 2002; Tran et al., 2011; Merloni et al., 2014). In contrast, a number of Type 1 AGN (Sy1 - 1.9) are highly X-ray absorbed (e.g., Shimizu et al., 2018).

In this paper, we study the spectral properties of an unusual source from the *Swift*/BAT survey, 2MASX J193013.80+341049.5, which is optically classified as a Type 1 AGN, yet is found to be highly X-ray absorbed, with a column density $N_{\text{H}} > 10^{23} \text{ cm}^{-2}$. The source is a nearby ($z = 0.063$) Seyfert galaxy with a bolometric luminosity $L_{\text{Bol}} = 1.3 \times 10^{45} \text{ erg s}^{-1}$ (Koss et al., 2017), a *R*-band apparent magnitude of 15.8, and a compact optical morphology. We present results from modeling the broadband X-ray spectrum of 2MASX J193013.80+341049.5 using *NuSTAR*, *XMM-Newton* and *Swift*/BAT observations, and examine the multi-wavelength properties of this source. This paper is structured as follows: in section 4.2 we describe the X-ray observations and data reduction procedures; in section 4.3 we present results from broadband X-ray modeling; section 3.4 presents analysis of multi-wavelength data on this source, including optical spectra and broadband Spectral Energy Distributions (SEDs); section 4.5 summarizes our results and presents our conclusions.

3.2 X-ray Observations and Data Reduction

NuSTAR

2MASX J193013.80+341049.5 was observed with *NuSTAR* in July 2016 for ~ 20 ks as part of the Extragalactic Legacy Surveys program¹. A second, deeper *NuSTAR* observation was performed in October 2017 for ~ 50 ks. Details of both these observations are presented in Table 3.1.

We reduced the raw event data from both *NuSTAR* modules, FPMA and FPMB (Harrison et al., 2013) using the *NuSTAR* Data Analysis Software (NuSTARDAS, version 2.14.1), distributed by the NASA High-Energy Astrophysics Archive Research Center (HEASARC) within the HEASOFT package, version 6.24. Instrumental responses were calculated based on the *NuSTAR* calibration database (CALDB), version 20180925. We cleaned and filtered raw event data for South Atlantic Anomaly (SAA) passages using the `nupipeline` module. We extracted source and background spectra from the calibrated and cleaned event files using the `nuproducts` module. Detailed information on these data reduction procedures can be found in the *NuSTAR* Data Analysis Software Guide (Perri et al., 2017). A circular extraction radius of 30 was used for both the source and background regions. We extracted the background spectrum from source-free regions of the image on the same detector chip as the source, away from the outer edges of the field of view, which have systematically higher background. In order to maximize the available *NuSTAR* exposure, we extracted the ‘spacecraft science’ mode 6 data, in addition to the standard ‘science’ mode 1 data, following the method outlined in Walton et al. (2016). We coadded the mode 1 and mode 6 spectra for each respective observation using the HEASOFT task `addspec`. We rebinned the spectral files using the HEASOFT task `grppha` to give a minimum of 20 photon counts per bin.

Archival XMM-Newton

In addition to the *NuSTAR* observations taken in the 3–79 keV band, we analyzed archival *XMM-Newton* observations taken in May 2009.

We performed reduction of the *XMM-Newton* data using the *XMM-Newton* Science Analysis System (SAS, version 16.1.0), following the standard prescription outlined in the *XMM-Newton* ABC online guide.² Calibrated, cleaned event files were created from the raw data files using the SAS commands `epchain` for the EPIC-pn detector (Strüder et al., 2001) and `emchain` for the two EPIC-MOS detectors (Turner et al.,

¹https://www.nustar.caltech.edu/page/legacy_surveys

²<https://heasarc.gsfc.nasa.gov/docs/xmm/abc/>

2001). As recommended, we only extracted single and double pixel events for EPIC-pn and single to quadruple pixel events for EPIC-MOS. We excluded intervals of high background flux in the first $\approx 1/4$ of the observation, resulting in total source exposure of 8.4, 11.0, and 12.8 ks for the pn, MOS1 and MOS2 detectors, respectively. Source spectra were extracted from the cleaned event files using the SAS task `xmmselect` from a circular aperture with a radius of 40 centered on the source. Background spectra were extracted from a circular aperture with radius of 80 placed near the source on the same chip. Instrumental response files were generated for each of the detectors using the SAS tasks `rmfgen` and `arfgen`.

Archival Swift

In addition to the *NuSTAR* and *XMM-Newton* spectra, we also analyzed *Swift*/BAT spectra collected over the first 70 months of observation (Baumgartner et al., 2013), covering the 14–195 keV band. The *Swift*/BAT data reduction procedure is detailed in Oh et al. (2018). We do not include *Swift*/XRT data in our broadband spectral modeling due to the poor signal-to-noise ratio of available *Swift*/XRT data, which has < 200 total photon counts. We separately analyzed archival *Swift*/XRT data taken in 2005 to check for N_{H} variability. For this analysis, we reduced the *Swift*/XRT data using the `XRTPIPELINE`, following the standard procedures detailed in Evans et al. (2009).

3.3 X-ray Spectral Modeling

We performed joint spectral modeling of the broadband *NuSTAR*, *XMM-Newton*, and *Swift*/BAT data using XSPEC v12.8.2 (Arnaud, 1996). We use χ^2 statistics for all model fitting and error estimation, and we quote uncertainties at the 90% confidence level. We adopt cross sections from Verner et al. (1996) and solar abundances from Wilms et al. (2000). We account for variability between different epochs by including cross-normalization factors between different datasets (e.g., Baloković et al., 2018). In all our modeling, we include a Galactic absorption component with a fixed column density of $N_{\text{H, Gal}} = 1.62 \times 10^{21} \text{ cm}^{-2}$ (Kalberla et al., 2005). We did not include *NuSTAR* data from the 2016 observation above 30 keV, as the source becomes background dominated above this energy, due to higher background levels relative to the 2017 observation. We model *NuSTAR* data from 2017 in the 3–79 keV band, and archival *XMM-Newton* data in the 0.4–10 keV band.

Analysis of the *NuSTAR* light curves for both observations in the 3–50 keV band (shown in Figure 3.1) show little evidence for strong variability in either the 2016

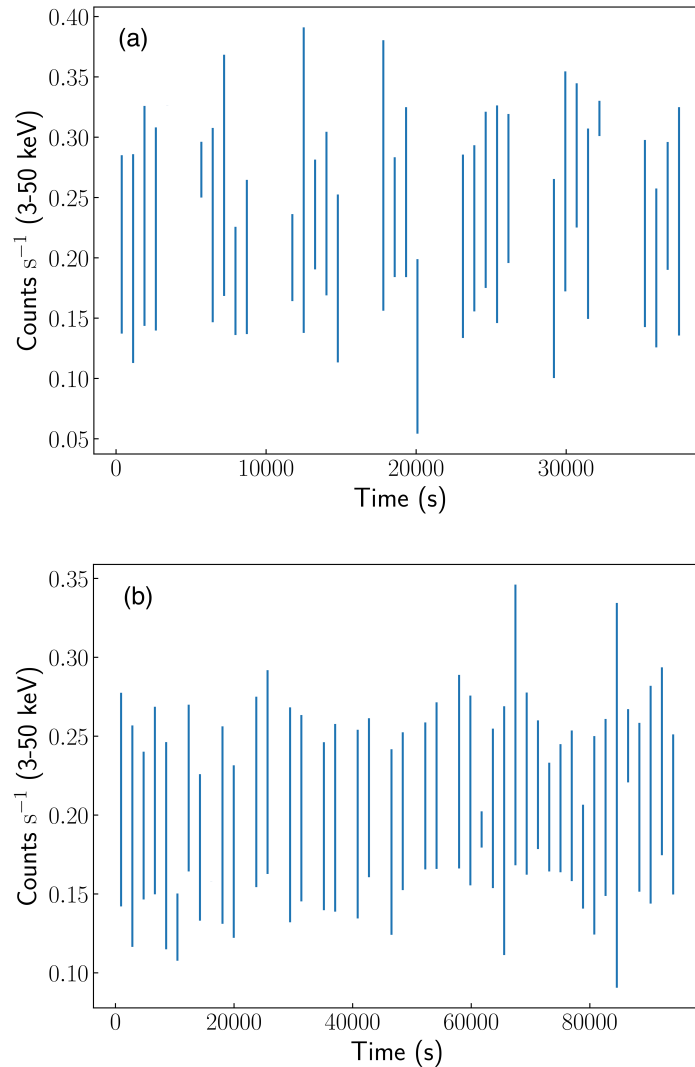


Figure 3.1: *NuSTAR* light curves of 2MASX J193013.80+341049.5 in the 3–50 keV band, where (a) is the light curve of the ~ 20 ks observation taken in 2016 and (b) the deeper ~ 50 ks observation taken in 2017. Gaps in data are due to Earth occultation events. There is no evidence for strong X-ray variability in this source.

or 2017 observations, justifying the use of time-averaged spectra. Flux levels in the 2–10 keV band were also found to be similar between the two observations. Hogg et al. (2012) performed a detailed light curve analysis of the archival *XMM-Newton* observation and found no significant variability in the *XMM-Newton* EPIC-pn and MOS light curves.

In our spectral modeling, we simultaneously fit the *XMM-Newton* (EPIC-pn and EPIC-MOS), *NuSTAR* (FPMA and FPMB), and *Swift*/BAT spectra, covering a total energy range from 0.4 to 150 keV. We begin our analysis by fitting a simple absorbed

cutoff power law model to the broadband data. As shown in Figure 4.1, an Fe $K\alpha$ emission line near 6.4 keV is evident in addition to excess soft emission below 3 keV.

We construct models consisting of both phenomenological reflection models and physically-motivated torus models. All models include a photoelectric neutral absorber, power law continuum, and a scattered power law continuum. We leave the line-of-sight column density N_{H} free between different epochs. We list the applied models in XSPEC notation as follows:

1. `phabs × (zphabs × cabs × cutoffpl + zgauss + pexrav + constant × cutoffpl)`: Models an absorbed cutoff power law with a Gaussian Fe $K\alpha$ line, a cold Compton reflection component and a scattered power law component. `phabs` models Galactic absorption while `zphabs` models host galaxy absorption. `pexrav` (Magdziarz & Zdziarski, 1995) models reflection off a slab of infinite extent and optical depth covering between 0 and 2π steradians of the sky relative to the illuminating source, corresponding to R between 0 and 1.
2. `phabs × (cabs × TBFFe × cutoffpl + pexmon + constant × cutoffpl)`: Similar to Model 1, with the exception that `zphabs` is replaced with `TBFFe`, which models absorption with a variable iron abundance; the `zgauss` and `pexrav` components are replaced with `pexmon`, which is a slab reflection model that self consistently models the Fe & Ni K complexes and Compton reflection hump assuming a semi-infinite plane geometry.
3. `phabs × (cabs × TBFFe × cutoffpl + borus02 + constant × cutoffpl)`: In the physically motivated `borus02` model (Baloković et al., 2018), obscuring material is arranged in a toroidal structure around the central AGN, with a variable opening angle and torus column density that can be decoupled from the line-of-sight column density. This model provides self-consistent modeling of the fluorescent line emission and Compton reflection features.

For Model 1, we set iron and light element abundances to solar values and fix the inclination angle of the plane of reflecting material at the default value of $\cos \theta = 0.45$. We tie the photon index and normalization of the reflected power law to that of the incident power law. We fix the energy of the Fe $K\alpha$ line at 6.4 keV. As shown in Figure 4.1 (c), this model provides a considerable improvement in the

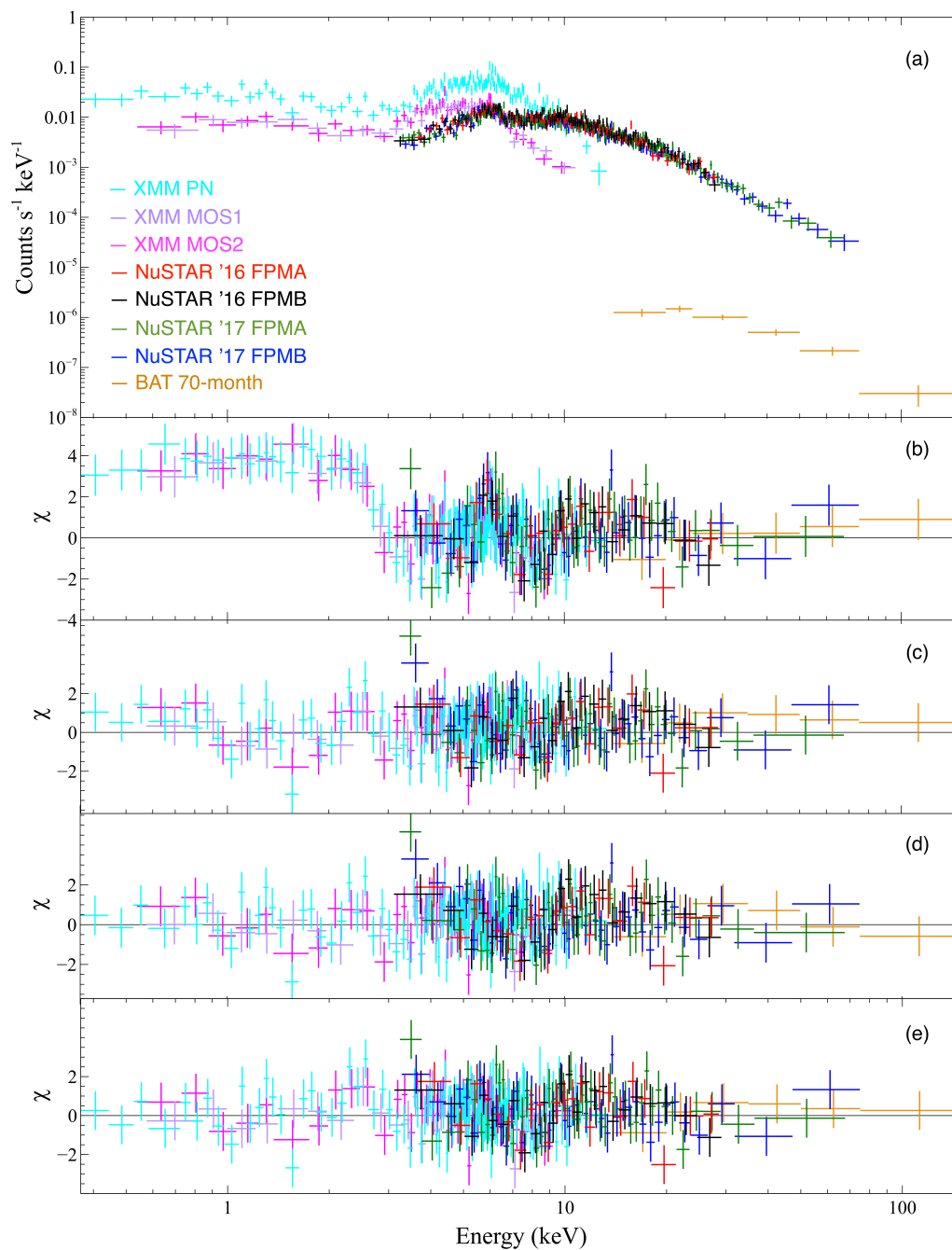


Figure 3.2: Broadband X-ray spectrum of 2MASX J19301380+3410495 (a), alongside fit residuals for (b) an absorbed cutoff power law model ($\chi^2/\text{dof} = 1409/811$), (c) absorbed cutoff power law with an Fe $K\alpha$ line, scattered power law, and a reflection component incorporated using the pexrav model ($\chi^2/\text{dof} = 826/798$), (d) absorbed cutoff power law with a variable iron abundance absorber and reflection modeled with pexmon ($\chi^2/\text{dof} = 816/798$), and (e) borus model ($\chi^2/\text{dof} = 808/795$).

fit compared to an absorbed cutoff power law model, with $\chi^2/\text{dof} = 826/798$. We find evidence of moderate reflection, with the reflection parameter R constrained to $0.26_{-0.23}^{+0.32}$. The cutoff energy is found to be strikingly low; $E_{\text{cut}} = 50_{-11}^{+19}$ keV. We find a fairly hard photon index ($\Gamma = 1.35_{-0.15}^{+0.18}$), which may partly account for the low cutoff energy obtained, due to degeneracy between E_{cut} and Γ , as evident in Figure 3.4. The line-of-sight column density exceeds 10^{23} cm^{-2} in all epochs of observation, confirming this source to be highly X-ray absorbed. The value of N_{H} was similar between the *NuSTAR* observations, at $\sim (3 - 4) \times 10^{23} \text{ cm}^{-2}$. For the archival *XMM-Newton* observation, N_{H} was slightly lower at $\sim 2.6 \times 10^{23} \text{ cm}^{-2}$, but still consistent with high X-ray obscuration, and with the values reported by Hogg et al. (2012). We also examined archival *Swift*/XRT spectra taken in December 2005 and found high levels of absorption, with N_{H} found to be $5.3_{-2.3}^{+5.5} \times 10^{23} \text{ cm}^{-2}$ from fitting Model 1 to the data.

We find a fairly low equivalent width of the Fe $K\alpha$ line, at ≈ 80 eV for the *XMM-Newton* observation and ≈ 90 eV for the *NuSTAR* observation. This motivates the exploration of alternative models with a variable iron abundance. In Model 2, we allow the iron abundance to vary by replacing the photoelectric absorption component `zphabs` with an absorber with variable iron abundance (`TBFeo`). We also replace the `pexrav` reflection model and `zgauss` line component with the phenomenological `pexmon` model, which self-consistently models both the reflection continuum and the Fe $K\alpha$ line. We tie the iron abundance parameter of the `pexmon` model to that of `TBFeo`. Model 2 yields an improvement to the fit compared to Model 1, with $\chi^2/\text{dof} = 816/798$. However, we find that the iron abundance is consistent with the Solar value when left as a free parameter. The reduction in χ^2/dof compared to Model 1 is likely attributed to differences between the two models, such as the inclusion of additional emission lines in Model 2. Furthermore, Model 2 produces slightly higher N_{H} values for a given epoch (see Table 3.2).

The phenomenological models used to account for reflection assume a simplistic slab geometry of the reflector with infinite extent and optical depth. While such models provide a convenient, simplified picture of the AGN reprocessor, they are not a physically realistic description of the geometry of the circumnuclear material, which is thought to have a roughly toroidal shape. We thus construct a third, physically-motivated model in which the `pexmon` component is replaced by `borus02` (Baloković et al., 2018). The `borus02` model self-consistently computes the absorbed and reprocessed emission for a torus geometry with a central illuminating

Table 3.2: Best-fit parameter values from modeling the broadband X-ray spectrum of 2MASX J193013.80+341049.5

Model component	Parameter		Model 1	Model 2	Model 3
zphabs	N_{H} (<i>NuSTAR</i> 2016)	[10^{23} cm $^{-2}$]	3.3 ± 0.3	-	-
	N_{H} (<i>NuSTAR</i> 2017)	[10^{23} cm $^{-2}$]	3.8 ± 0.3	-	-
	N_{H} (<i>XMM-Newton</i>)	[10^{23} cm $^{-2}$]	$2.6^{+0.3}_{-0.2}$	-	-
TBFeo	A_{Fe}	[solar]	-	$1.07^{+0.25}_{-0.30}$	$0.45^{+0.06}_{-0.05}$
	N_{H} (<i>NuSTAR</i> 2016)	[10^{23} cm $^{-2}$]	-	$4.8^{+0.6}_{-0.5}$	$5.2^{+0.5}_{-0.1}$
	N_{H} (<i>NuSTAR</i> 2017)	[10^{23} cm $^{-2}$]	-	$5.5^{+0.7}_{-0.5}$	$4.9^{+0.5}_{-0.7}$
	N_{H} (<i>XMM-Newton</i>)	[10^{23} cm $^{-2}$]	-	$3.9^{+0.4}_{-0.3}$	$4.7^{+0.3}_{-0.4}$
pexrav	Γ^A		$1.35^{+0.18}_{-0.15}$	-	-
	E_{cut}	[keV]	$49.9^{+19.0}_{-11.2}$	-	-
	R		$0.26^{+0.32}_{-0.23}$	-	-
	A_{Fe}	[solar]	1 (fixed)	-	-
	Norm B	[10^{-3}]	$1.41^{+0.59}_{-0.37}$	-	-
pexmon	Γ^A		-	$1.33^{+0.21}_{-0.14}$	-
	E_{cut}	[keV]	-	$49.9^{+38.3}_{-13.2}$	-
	R		-	$0.25^{+0.23}_{-0.10}$	-
	Norm B	[10^{-3}]	-	$1.47^{+0.54}_{-0.34}$	-
borus02	Γ^A		-	-	$1.73^{+0.05}_{-0.27}$
	E_{cut}	[keV]	-	-	$71.9^{+21.2}_{-41.0}$
	$\log N_{\text{H,Tor}}$		-	-	$24.25^{+0.02}_{-0.12}$
	C_f^C	[%]	-	-	> 83.9
	Norm B	[10^{-3}]	-	-	$2.44^{+0.63}_{-0.81}$
χ^2/dof			826/798	816/798	808/795

A Continuum photon index.

B power law normalization in units of counts s $^{-1}$ keV $^{-1}$ at 1 keV.

C Torus covering factor.

X-ray source. It provides more flexibility in modeling the torus geometry compared to previously developed torus models such as MYTorus (Murphy & Yaqoob,

2009), as it includes the opening angle, the high-energy cutoff, and the relative iron abundance as free parameters. In contrast, MYTorus assumes a uniform density torus with a fixed opening angle of 60° , Solar abundance of iron, and a termination energy at 500 keV. Both models can emulate torus clumpiness by allowing the average column density through the torus to be independent of the line-of-sight column density.

With Model 3, we set the covering factor of the torus, C_f , equal to $\cos i$, where i is the viewing angle of the torus. We find that the fit naturally converges close to $C_f = \cos i$ when both parameters are left free to vary. We tie the iron abundance parameter of `borus02` to that of `TBFeo`. We link the photon index and normalization of the `borus02` component to that of the incident power law. Model 3 provides the best fit to the data compared to Models 1 and 2, with $\chi^2/\text{dof} = 808/795$. Leaving the iron abundance free results in a sub-solar value ($A_{\text{Fe}} = 0.45^{+0.06}_{-0.05}$), consistent with the weak Fe $K\alpha$ line observed in this source.

Table 3.2 summarizes our modeling results for some of the key best-fit parameters for each of the three spectral models applied in this work. We conclude from our broadband spectral fitting that our physically-motivated `borus02` model (Model 3) provides the best fit to the data and also gives a photon index that lies within the typical range observed for Seyferts. We show the full broadband unfolded X-ray spectrum for the `borus02` model fit in Figure 3.3.

With the additional, deeper 50 ks *NuSTAR* observations taken in 2017, the high-energy cutoff of the X-ray continuum is confirmed to be constrained to values that are atypically low compared to the Seyfert population. Ricci et al. (2017b) found that the median cutoff energy for the *Swift*/BAT sample of unobscured AGN is $E_{\text{cut}} = 210 \pm 36$ keV. Figure 3.4 shows the contour plot of the photon index against the high-energy cutoff from the `borus02` model fit. While there is some degree of degeneracy between these two parameters, the value of E_{cut} is constrained to low values that are below the median cutoff energy found by Ricci et al. (2017b). Such a low coronal cutoff is unusual but not unprecedented, with recent detections reported of AGN with high-energy cutoffs within the *NuSTAR* band (e.g., Tortosa et al., 2017; Kara et al., 2017; Kamraj et al., 2018).

Various explanations have been proposed for the origin of low temperature coronae. For sources accreting at high Eddington rates, Compton cooling may be enhanced due to the stronger radiation field present in comparison to lower Eddington ratio Seyferts (Kara et al., 2017). For AGN accreting well below the Eddington limit,

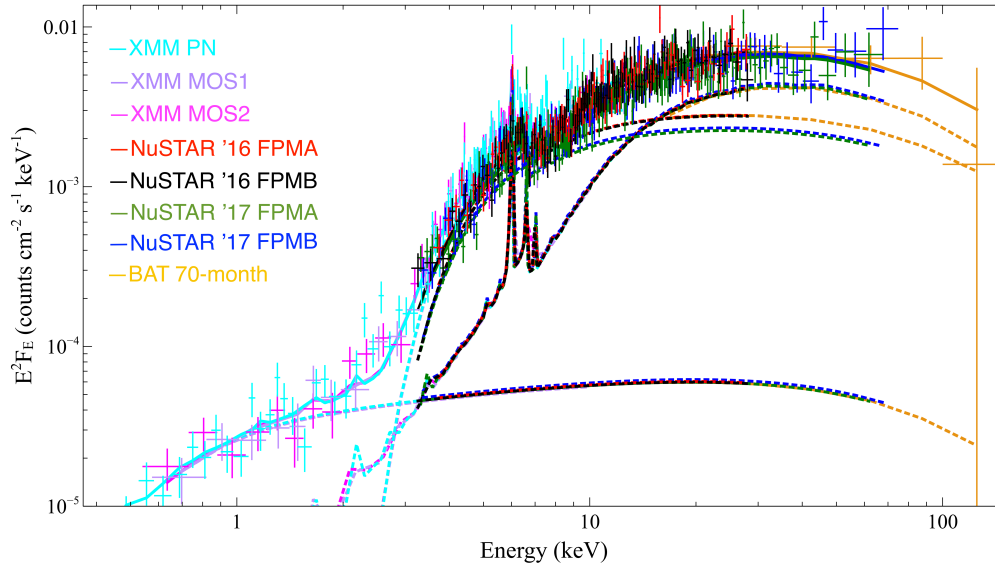


Figure 3.3: Broadband X-ray spectrum of 2MASX J193013.80+341049.5 unfolded through the *borus02* model (Model 3). Solid lines represent total model while dashed lines depict individual model components.

low coronal temperatures may be attributed to a high optical depth within the corona, which results in more effective cooling due to multiple inverse Compton scatterings of seed photons from the accretion disk (Tortosa et al., 2017). Low temperatures can also be achieved if the corona consists of a hybridized plasma, containing both thermal and non-thermal particles (e.g., Zdziarski et al., 1993; Ghisellini et al., 1993; Fabian et al., 2017). In such a hybridized system, only a small fraction of non-thermal electrons with energies above 1 MeV are needed to result in runaway electron-positron pair production. The cooled pairs redistribute their available energy, thereby reducing the mean energy per particle and decreasing the coronal temperature. Such cooling would produce a hard non-thermal tail in the X-ray spectrum and an annihilation feature at 511 keV, both of which are currently undetectable with present X-ray instrumentation. In order to robustly test hybrid plasma models, next-generation hard X-ray observatories with high sensitivity at energies beyond 100 keV, such as the *High-Energy X-ray Probe (HEX-P)* (Madsen et al., 2018), will be essential.

3.4 Multi-wavelength Analysis

From broadband X-ray spectral modeling, we confirm that 2MASX J193013.80+341049.5 exhibits high levels of X-ray obscuration, with N_{H} exceeding 10^{23} cm^{-2} in both the

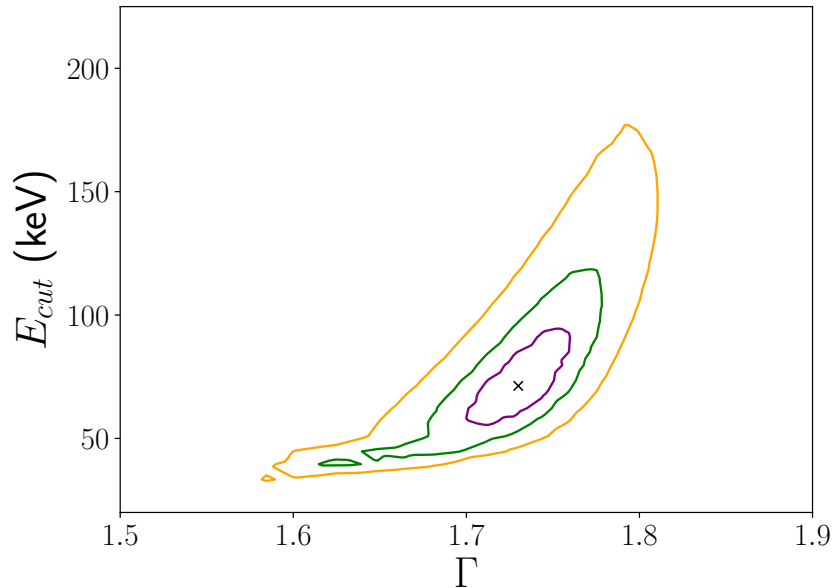


Figure 3.4: $E_{\text{cut}}-\Gamma$ contour plot from the `borus02` model fit (Model 3) to broadband X-ray data of 2MASX J193013.80+341049.5. The solid purple, green, and yellow contours correspond to the 68, 90, and 99 % confidence levels, respectively. The black cross represents the best-fit values of the parameters from applying the `borus02` model.

NuSTAR and archival *XMM-Newton* observations. The X-ray spectral features of this source are characteristic of a classic obscured, Type 2 AGN. The high X-ray absorption present is thus in clear conflict with the optical classification of this source as a Type 1 AGN. We explore properties of this enigmatic source at other wavelengths to investigate whether there are other unusual features possibly linked to the high X-ray obscuration, but comparatively lower optical obscuration present in this source. We also discuss possible mechanisms for producing such mismatches between X-ray and optical classifications.

Optical Spectra

2MASX J193013.80+341049.5 has consistently been classified as a Type 1 AGN from optical spectra taken over several epochs (e.g., Landi et al., 2007; Trippe et al., 2011), which show clear broad components to the $H\alpha$ and $H\beta$ lines. We also obtained recent optical spectra using the Double Spectrograph (DBSP) instrument on the 200-inch Hale telescope at Palomar Observatory. Observations were performed in 2016 October, 2018 August, and 2019 August. We compare the Palomar spectra with those taken at Orzale in 2006 and KPNO in 2007 (Koss et al., 2017). Full observation details of the optical spectra examined in this work are presented in

Table 3.3: Observation details of the optical spectra of 2MASX J193013.80+341049.5 considered in this work.

Observation Date	Telescope	Instrument	Exposure time (s)	Slit Size (\AA)	Slit Size (kpc)	Spectral Resolution (FWHM) (\AA)
2006-05-08	Orzale	BFOSC	3600	2	2.4	13
2007-06-16	KPNO	Goldcam	3600	2	2.4	3.3
2016-10-02	Palomar	DBSP	300	1.5	1.8	4.2, 5.9
2018-08-11	Palomar	DBSP	300	2	2.4	4.8, 7.4
2019-08-28	Palomar	DBSP	900	1.5	1.8	4.4, 5.8

Table 3.4: Flux details and selected line-width properties of the optical spectra of 2MASX J193013.80+341049.5 considered in this work.

Observation Date	Continuum flux ^A ($\text{erg s}^{-1} \text{cm}^{-2} \text{\AA}^{-1}$)	H α flux ($10^{-17} \text{erg s}^{-1} \text{cm}^{-2}$)	H α FWHM (km s^{-1})	H β flux ($10^{-17} \text{erg s}^{-1} \text{cm}^{-2}$)	H β FWHM (km s^{-1})
2006-05-08	160	60501	6948	8580	3577
2007-06-16	77	37097	7053	4363	3373
2016-10-02	78	41239	6720	3189	3639
2018-08-11	48	33022	6697	1822	3610
2019-08-28	58	30915	7227	2657	4385

^A Continuum flux density estimated in the 4760–4780 \AA band.

Table 3.3. Broad H α and H β lines are present in all epochs, consistent with a Type 1 optical classification (Figure 3.5). We also observed a nearby galaxy companion during the UT 2019 August 28 observation, 2MASX J193015.12+34111.18, which is 27.3 to the northeast of the AGN (33.4 kpc). The galaxy is an absorption line system at a close redshift ($z = 0.063$ based on the Ca H+K absorption lines) to the primary AGN galaxy.

For emission line measurements, we follow the procedure used in the OSSY database (Oh et al., 2011) and its broad-line prescription (Oh et al., 2015). We apply stellar templates (Bruzual & Charlot, 2003; Sánchez et al., 2006) and emission-line fitting in a rest-frame ranging from 3780 \AA to 7580 \AA . Using the broad H α flux and line-widths from the 2016 observation, we derive a black hole mass of $\log(M_{\text{BH}}/M_{\odot}) = 8.3$ using the virial approximation of Greene & Ho (2007). The flux of the broad H β line, broad H α line, and continuum (4760–4780 \AA) are observed to decrease over the period 2006–2019 (Table 3.4) by more than a factor of 2. Errors are dominated by flux calibration of the order 10–20%. The H β line FWHM remains roughly constant across observations. It is unlikely that the mismatch in X-ray and optical classifications is due to short timescale variability of the line-of-sight absorption, as N_{H} remains consistently high in all epochs of X-ray observations. Furthermore, Hogg et al. (2012) note little variability in optical spectra taken three months apart (Landi et al., 2007; Winter et al., 2010).

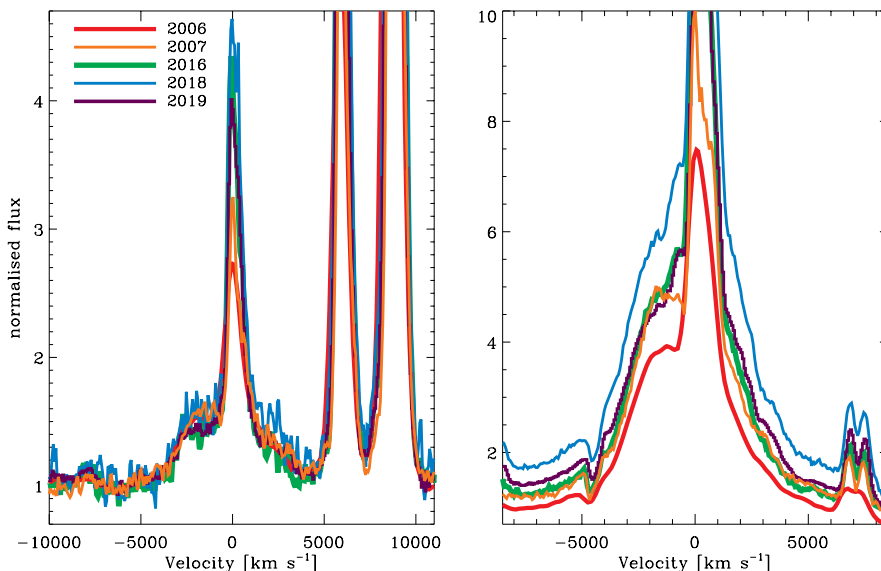


Figure 3.5: Optical spectra of 2MASX J193013.80+341049.5 taken at Orzale (2006), KPNO (2007), and Palomar Observatory (2016, 2018, 2019). The fluxes have been normalized by the emission in a line-free region (4760 - 4780 Å). Left and right panels show the velocity centered on the $H\beta$ and $H\alpha$ line profiles, respectively.

X-ray to Mid-IR Relation

It is well-established that the X-ray and mid-IR emission from AGN are correlated (e.g., Lutz et al., 2015; Gandhi et al., 2009; Stern, 2015). We investigate whether 2MASX J193013.80+341049.5 has mid-IR properties that are consistent with the observed correlation between mid-IR and X-ray luminosity. We estimate the mid-IR luminosity at 6 μm by constructing the broadband SED for 2MASX J193013.80+341049.5 using publicly available data from the *Vizier* catalog. The data obtained from *Vizier* includes measurements from catalogs such as 2MASS, Gaia, PanSTARRS, AKARI, WISE, and XMM-UVOT, covering a total wavelength range from 0.3–100 μm . We linearly interpolate between 3.75 and 15 μm to determine the rest-frame 6 μm flux density. We convert from specific flux to luminosity using a luminosity distance of 268 Mpc obtained from the NASA/IPAC Extragalactic Database (NED). We calculate the X-ray luminosity from the unabsorbed flux in the 2–10 keV band, using the 2017 *NuSTAR* data. We also estimated the predicted 2–10 keV luminosity based on the $H\alpha$ luminosity measured from the 2016 optical spectra, using the observed relation between intrinsic 2–10 keV luminosity and $H\alpha$ luminosity (Panessa et al., 2006). We found the predicted X-ray luminosity to be consistent with the intrinsic luminosity observed from the *NuSTAR* data.

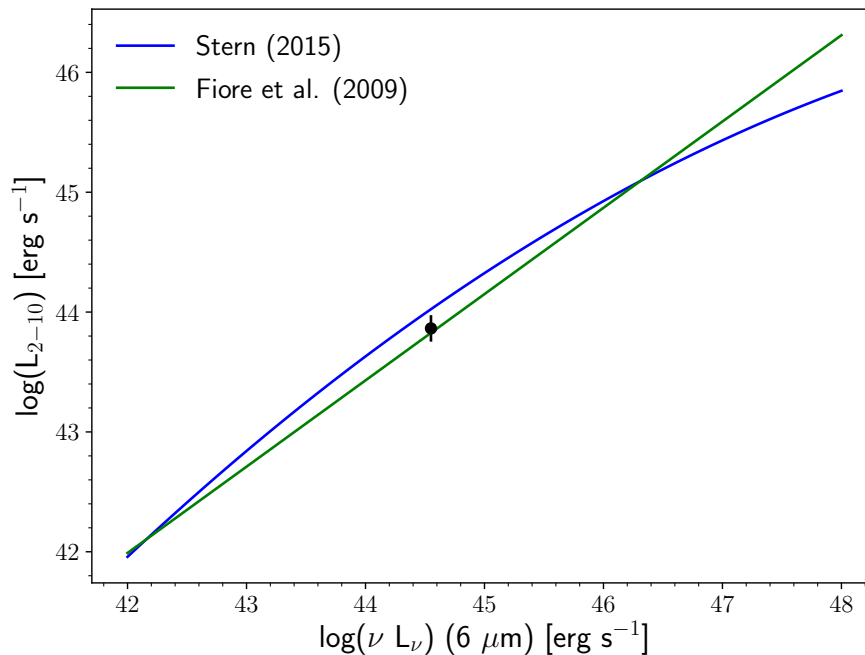


Figure 3.6: Rest-frame 2–10 keV X-ray luminosity against rest-frame 6 μm mid-infrared luminosity for 2MASX J193013.80+341049.5 (black point) along with published relations from Fiore et al. (2009) and Stern (2015).

Figure 3.6 shows the rest-frame 2–10 keV luminosity against the rest-frame 6 μm luminosity for 2MASX J193013.80+341049.5, along with correlations reported in the literature. Fiore et al. (2009) report a mid-IR to X-ray correlation based on samples of X-ray-selected Type 1 AGN in the COSMOS and CDFS fields. The relation presented in Stern (2015) was obtained by including a sample of the most luminous quasars from the Sloan Digital Sky Survey, and is appropriate for AGN across a large luminosity range, spanning from the Seyfert through to the quasar regime. The location of our source is consistent with both these published relations, indicating that 2MASX J193013.80+341049.5 is not atypical in terms of its mid-IR/X-ray luminosity ratio.

Broadband SED and α_{ox}

We construct the broadband SED for 2MASX J193013.80+341049.5 using publicly available flux densities from the *Vizier* catalog and PanSTARRS DR2. We perform SED fitting in order to investigate the relationship between UV and X-ray luminosity for this source, parameterized by the α_{ox} spectral slope, defined as:

$$\alpha_{\text{ox}} = -0.384 \times \text{Log}[L_{2\text{keV}}/L_{2500}]$$

where $L_{2\text{keV}}$ and L_{2500} are the monochromatic luminosities at 2 keV and 2500 Å, respectively. We determine the monochromatic luminosity at 2500 Å, corrected for dust-reddening, via SED template fitting. We model the SED of 2MASX J193013.80+341049.5 in the 0.03–30 μm range using the algorithm and empirical templates of Assef et al. (2010). The models consist of a linear combination of a dust-reddened AGN template and three empirical galaxy templates, corresponding to E, Sbc, and Im-type galaxies. We do not include UV data in our SED fitting due to the uncertainty in the UV extinction correction. Figure 3.7 presents the best-fit SED model of 2MASX J193013.80+341049.5 along with individual model components. We linearly interpolate the best-fit, un-reddened AGN component to determine the intrinsic specific flux at 2500 Å. We compute the monochromatic X-ray luminosity at 2 keV from modeling the broadband X-ray spectra, correcting for absorption.

In Figure 3.8 we present the monochromatic X-ray luminosity as a function of the monochromatic UV luminosity, along with fitted relations reported in the literature. Lusso et al. (2010) present a significant correlation between $L_{2\text{keV}}$ and L_{2500} based on a sample of 545 X-ray-selected Type 1 AGN from the XMM-COSMOS survey, spanning a wide range of redshifts and X-ray luminosities. In Lusso & Risaliti (2016), a tighter correlation is reported using a sample of 2685 quasars that have been optically selected with homogeneous SED and X-ray detections, with dust-reddened and gas-obscured sources excluded from the sample. 2MASX J193013.80+341049.5 is consistent with observed relations between $L_{2\text{keV}}$ and L_{2500} (Figure 3.8), indicating that this source is also not atypical in terms of its UV/X-ray luminosity ratio. We find $\alpha_{\text{ox}} \sim 1.4$, which is within the typical range of α_{ox} distributions, which covers 1.2 - 1.8 (Lusso et al., 2010).

The normal X-ray-to-optical ratio (parameterized by α_{ox}) of 2MASX J193013.80+341049.5 indicates that it is unlikely that the Type 1 optical classification is due to scattering of BLR photons into our line of sight through a region of lower column density. If there were strong scattering present, a stronger X-ray-to-optical ratio would be expected due to suppression of optical emission. We further rule out a scattering scenario through our broadband SED fitting, where we allow for a second unobscured AGN component to account for the scattered light leaked from a primary obscured AGN component. The best-fit for such a model produces zero flux for the second AGN

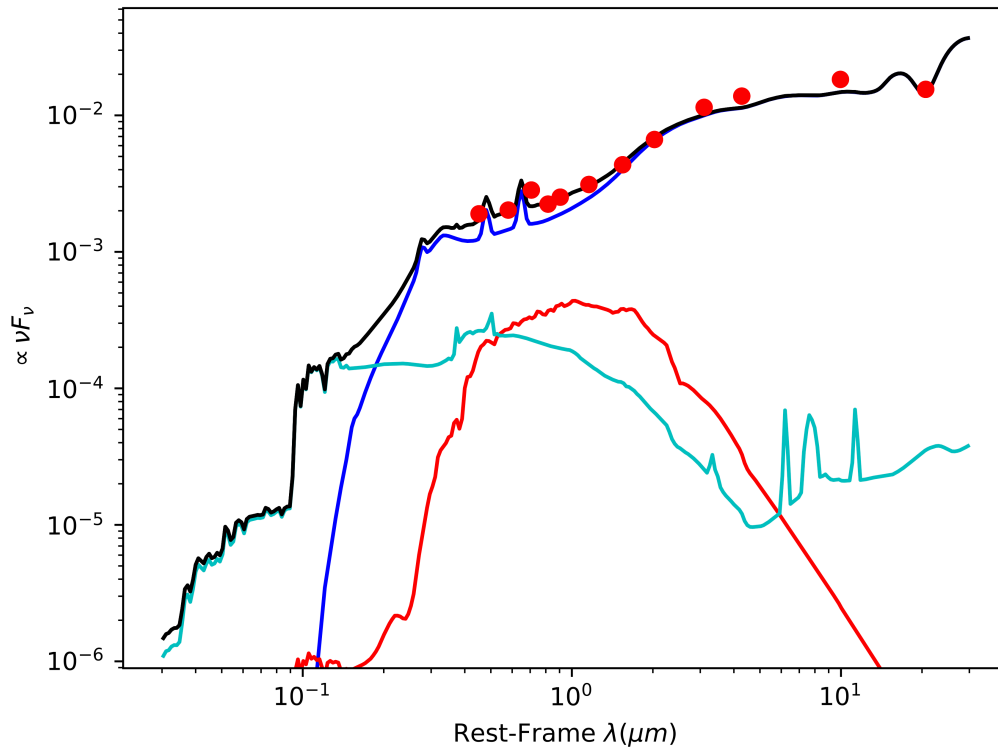


Figure 3.7: Spectral energy distribution (SED) of 2MASX J193013.80+341049.5. The best-fit SED model (black line) consists of an AGN component (blue line), a young stellar population (cyan line), and an old stellar population (red line). Solid red points are observed flux densities used for the SED fit, obtained from publicly available data from the *Vizier* catalog and PanSTARRS DR2.

component, indicating no evidence for scattered/reflected light leaking into our line of sight.

Gas-to-Dust Ratio

Some studies have reported Type 1 AGN with large X-ray column densities (e.g., Shimizu et al., 2018), however explanations for the existence of such objects have varied widely. One explanation that is consistent with the unified model is that our line of sight grazes the edge of the obscuring torus where the cloud distribution is less dense, but still provides significant X-ray absorption due to the X-ray corona's small physical size compared to the BLR. This would result in a larger effective covering fraction of the compact corona in comparison with the more extended BLR. This scenario is supported from our X-ray modeling with *Borus*, where we found that a geometry in which the torus is viewed through the rim provided the best-fit to the data.

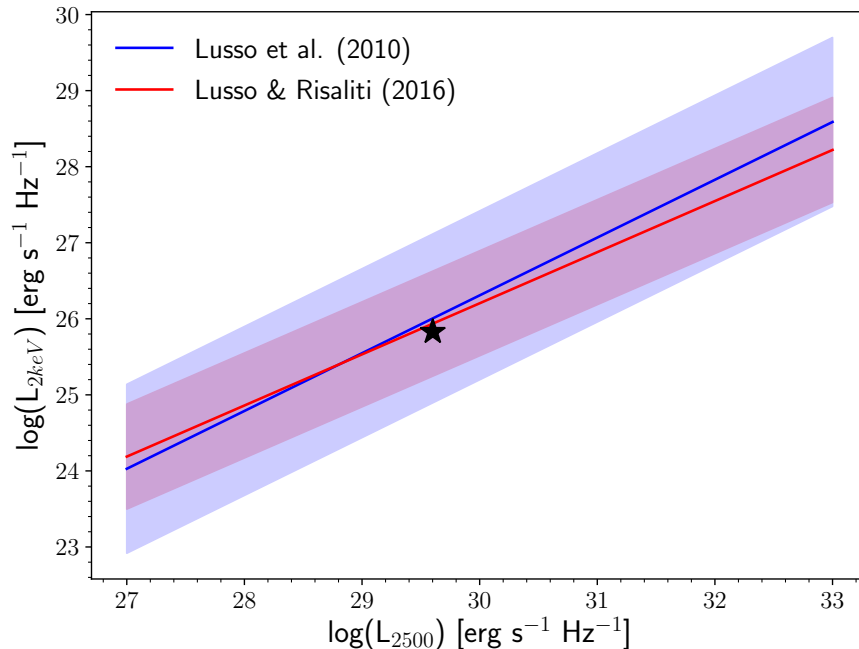


Figure 3.8: Rest-frame monochromatic 2 keV luminosity $L_{2\text{keV}}$, against rest-frame 2500 Å luminosity L_{2500} for 2MASX J193013.80+341049.5 (black star). Also plotted are literature relations from Lusso et al. (2010) and Lusso & Risaliti (2016). The shaded regions represent the 3σ dispersion in the fitted relations.

If we model the torus to have a clumpy distribution (Krolik & Begelman, 1988b), then another possibility is that a clump has entered our line of sight during the X-ray observation, causing a temporary increase in the X-ray column density. However, the lack of variability in N_{H} between epochs of X-ray observations appear to disfavor such short timescale variability as the cause of the X-ray/optical mismatch (see also Section 4.1).

High levels of X-ray obscuration but lack of optical obscuration could also be explained by the presence of high-density, ionized gas outflows. For example, the broad-line radio galaxy 3C 445 is classified as Type 1 from broad $\text{H}\alpha$ and $\text{H}\beta$ lines in its optical spectrum, however *Suzaku* and *Chandra* observations show it to be heavily absorbed with $N_{\text{H}} \sim 10^{23} \text{ cm}^{-2}$. The soft X-ray spectrum of this source is dominated by ionized emission lines (Braitto et al., 2011). A mechanism proposed by Braitto et al. (2011) is that the photo-ionized, outflowing absorber is associated with a disk wind that is clumpy in nature and located close to the central X-ray source. The clumpy distribution of the absorber enables visible sightlines to the BLR gas. High resolution X-ray grating observations are generally needed to identify emission lines or absorption features associated with ionized gas outflows.

Another possibility for the mismatch in X-ray and optical classifications for 2MASX J193013.80+341049.5 is a lower dust-to-gas ratio relative to the Galactic interstellar medium. Maiolino et al. (2001) investigated the ratio of reddening to the X-ray absorbing column density, E_{B-V}/N_{H} , for a diverse sample of AGN characterised by cold X-ray absorption. They found that E_{B-V}/N_{H} is lower than Galactic by factors ranging from ~ 3 –100 for most sources in their sample, assuming a standard Galactic extinction curve. In Figure 3.9, we show E_{B-V}/N_{H} as a function of the intrinsic 2–10 keV luminosity for 2MASX J193013.80+341049.5 compared to the sample from Maiolino et al. (2001). We find $E_{B-V} = 0.50 \pm 0.07$, determined from our broadband SED fitting. We observe that 2MASX J193013.80+341049.5 has an E_{B-V}/N_{H} that is significantly lower than the Galactic standard value by a factor of 170. This suggests that reduced dust absorption compared to the gaseous column density may likely explain the mismatch between the X-ray and optical classification of 2MASX J193013.80+341049.5. It is possible that the BLR itself provides extra X-ray obscuration and consists of neutral, dust-free gas that is an inner extension of the dusty molecular torus (Davies et al., 2015). If the BLR is the source of the X-ray absorption, N_{H} variability may be seen on relatively short timescales (e.g., Risaliti et al., 2005). One method to verify where the bulk of the absorbing gas resides is through resolving the width of the Fe $K\alpha$ line (e.g., Gandhi et al., 2015). Future X-ray missions such as *Athena* (Barcons et al., 2015) will be able to measure the width of the Fe $K\alpha$ line with unprecedented spectral resolution.

3.5 Summary

In this paper, we present both a broadband X-ray and a multi-wavelength analysis of the enigmatic X-ray obscured, but optically unobscured Type 1 AGN 2MASX J193013.80+341049.5. From joint modeling of *NuSTAR* and archival *XMM-Newton* observations, we find 2MASX J193013.80+341049.5 to be strongly absorbed, with $N_{\text{H}} > 2 \times 10^{23} \text{ cm}^{-2}$. We also find the source to possess an atypically low coronal temperature compared to the Seyfert population ($E_{\text{cut}} \sim 72 \text{ keV}$). Some possible mechanisms to explain the low coronal temperature include a large optical depth of the corona, a strong radiation field, or a hybrid pair-dominated plasma.

We investigate possible scenarios to explain the mismatch between X-ray and optical classifications using techniques such as broadband SED modeling. We find that 2MASX J193013.80+341049.5 likely has a much lower dust-to-gas ratio relative to the Galactic ISM, with E_{B-V}/N_{H} lower than the Galactic standard by a factor of ~ 170 . This suggests that the X-ray/optical mismatch could be explained by the

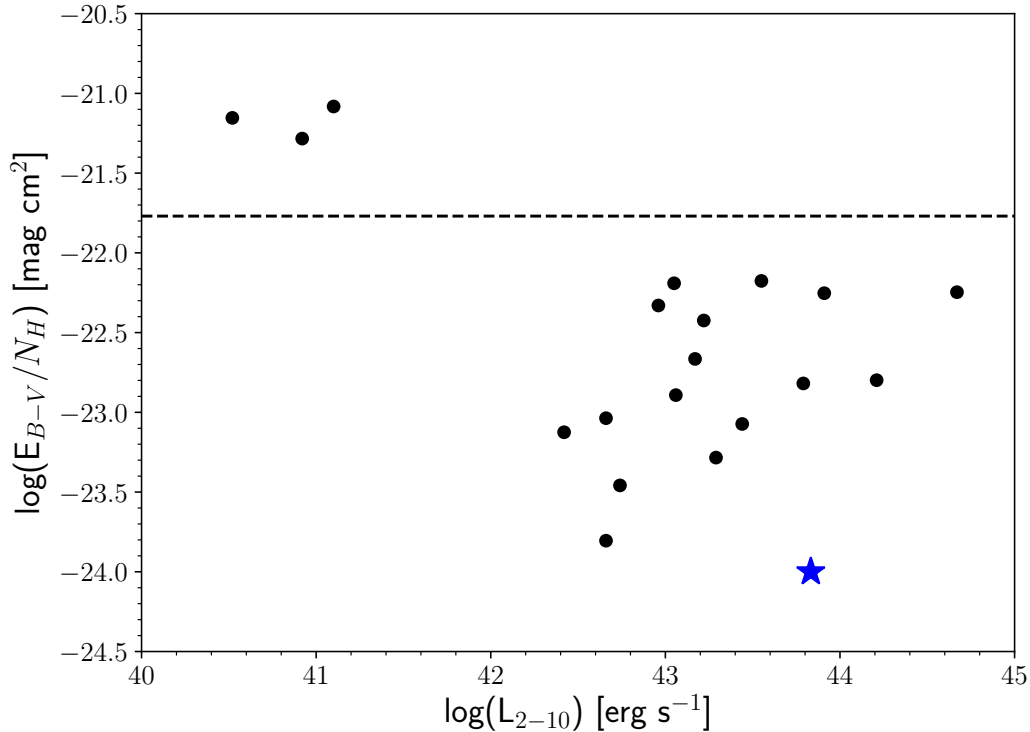


Figure 3.9: E_{B-V}/N_H ratio vs. intrinsic 2–10 keV X-ray luminosity for 2MASX J193013.80+341049.5 (blue star), and for sources from the sample of Maiolino et al. (2001) (black points). The reddening E_{B-V} is estimated assuming a Galactic standard extinction curve. The column density N_H is determined from fitting X-ray spectra. Dashed black line represents the Galactic standard value of E_{B-V}/N_H .

BLR itself providing the source of extra X-ray obscuration, and is composed of low-ionization, dust-free gas.

3.6 Acknowledgements

We have made use of data from the *NuSTAR* mission, a project led by the California Institute of Technology, managed by the Jet Propulsion Laboratory, and funded by the National Aeronautics and Space Administration. We thank the *NuSTAR* Operations, Software and Calibration teams for support with the execution and analysis of these observations. This research has made use of the *NuSTAR* Data Analysis Software (NuSTARDAS) jointly developed by the ASI Science Data Center (ASDC, Italy) and the California Institute of Technology (USA). M.B. acknowledges support from the Black Hole Initiative at Harvard University, which is funded in part by the Gordon and Betty Moore Foundation (grant GBMF8273) and in part by the John Templeton Foundation. M.K. acknowledges support from NASA through ADAP

award NNH16CT03C. D.J.W. acknowledges support from STFC in the form of an Ernest Rutherford fellowship. R.J.A was supported by FONDECYT grant number 1191124.

Chapter 4

**X-RAY CORONAL PROPERTIES OF *SWIFT*/BAT-SELECTED
SEYFERT 1 ACTIVE GALACTIC NUCLEI**

N. Kamraj, F. A. Harrison, M. Brightman, M. Baloković, C. Ricci, D. Stern, J. A. García, Michael J. Koss, J. E. Mejía-Restrepo, Kyuseok Oh, M. C. Powell, and C. M. Urry. X-ray Coronal Properties of *Swift*/BAT-Selected Seyfert 1 Active Galactic Nuclei. 2021, *The Astrophysical Journal*, *accepted*.

Nikita Kamraj¹, Fiona A. Harrison¹, Murray Brightman¹, Mislav Baloković², Claudio Ricci^{3,4,5}, Daniel Stern⁶, Javier A. García¹, Michael J. Koss⁷, Julian E. Mejía-Restrepo⁸, Kyuseok Oh^{9,10}, Meredith C. Powell¹¹, Claudia M. Urry¹²

¹Cahill Center for Astronomy and Astrophysics, California Institute of Technology, Pasadena, CA 91125, USA

²Yale Center for Astronomy & Astrophysics, 52 Hillhouse Avenue, New Haven, CT 06511, USA

³Núcleo de Astronomía de la Facultad de Ingeniería y Ciencias, Universidad Diego Portales, Av. Ejército Libertador 441, Santiago, Chile

⁴Kavli Institute for Astronomy and Astrophysics, Peking University, Beijing 100871, People's Republic of China

⁵George Mason University, Department of Physics & Astronomy, MS 3F3, 4400 University Drive, Fairfax, VA 22030, USA

⁶Jet Propulsion Laboratory, California Institute of Technology, Pasadena, CA 91109, USA

⁷Eureka Scientific Inc., 2452 Delmer St. Suite 100, Oakland, CA 94602, USA

⁸European Southern Observatory, Casilla 19001, Santiago 19, Chile

⁹Department of Astronomy, Kyoto University, Oiwake-cho, Sakyo-ku, Kyoto 606-8502, Japan

¹⁰Korea Astronomy and Space Science Institute, 776 Daedeokdae-ro, Yuseong-gu, Daejeon 34055, Republic of Korea

¹¹Kavli Institute of Particle Astrophysics and Cosmology, Stanford University, 452 Lomita Mall, Stanford, CA 94305, USA

¹²Yale Center for Astronomy & Astrophysics, 52 Hillhouse Avenue, New Haven, CT 06511, USA

Abstract

The corona is an integral component of Active Galactic Nuclei (AGN) which produces the bulk of the X-ray emission above 1–2 keV. However, many of its physical properties and the mechanisms powering this emission remain a mystery. In particular, the temperature of the coronal plasma has been difficult to constrain for large samples of AGN, as constraints require high quality broadband X-ray spectral coverage extending above 10 keV in order to measure the high energy cutoff, which provides constraints on the combination of coronal optical depth and temperature.

We present constraints on the coronal temperature for a large sample of Seyfert 1 AGN selected from the *Swift*/BAT survey using high quality hard X-ray data from the *NuSTAR* observatory combined with simultaneous soft X-ray data from *Swift*/XRT or *XMM-Newton*. When applying a physically-motivated, non-relativistic disk reflection model to the X-ray spectra, we find a mean coronal temperature $kT_e = 84 \pm 9$ keV. We find no significant correlation between the coronal cutoff energy and accretion parameters such as the Eddington ratio and black hole mass. We also do not find a statistically significant correlation between the X-ray photon index, Γ , and Eddington ratio. This calls into question the use of such relations to infer properties of supermassive black hole systems.

4.1 Introduction

Active Galactic Nuclei (AGN) are known to produce copious amounts of hard X-ray radiation. This continuum X-ray emission is believed to be produced in a hot cloud of plasma called the *corona*, where electrons Compton up-scatter thermal optical and UV photons from the accretion disk to X-ray energies (e.g., Haardt & Maraschi, 1993; Merloni & Fabian, 2001). While many of its physical properties are not well constrained, the corona is known to be compact, of the order of 3–10 R_g (where $R_g = GM_{\text{BH}}/c^2$ is the gravitational radius for a black hole of mass M_{BH}), as determined by methods such as rapid X-ray variability (e.g., McHardy et al., 2005), quasar microlensing (e.g., Chartas et al., 2016), and reverberation mapping of X-ray radiation reprocessed by the accretion disk (e.g., Fabian et al., 2009; De Marco et al., 2013; Uttley et al., 2014). AGN coronae may also be compact in a radiative sense, indicating an abundance of interactions involving significant energy exchange between particles and photons within the source (Fabian et al., 2015). This radiative compactness can be characterized by the dimensionless parameter l (Guilbert et al., 1983), defined as:

$$l = 4\pi \frac{m_p}{m_e} \frac{R_g}{R} \frac{L}{L_E} \quad (4.1)$$

where m_p and m_e are the proton and electron mass, respectively, R_g is the gravitational radius, R is the coronal radius, L is the coronal luminosity, and L_E is the Eddington luminosity.

Some of the fundamental physical properties of the corona, such as its temperature (kT_e) and optical depth (τ) can be probed through broadband X-ray spectroscopy. Specifically, the coronal X-ray emission can be characterized by a high-energy cutoff,

E_{cut} , when approximating the X-ray continuum flux as a power law $\propto E^{-\Gamma} e^{-E/E_{\text{cut}}}$, where E is the photon energy and Γ is the continuum photon index (e.g., Rothschild et al., 1983). Spectral parameters obtained from broadband X-ray fitting thus correspond to physical parameters of the corona, with the temperature related to the cutoff energy via $E_{\text{cut}} \sim 2\text{--}3 kT_e$, assuming a slab-like coronal geometry (Petrucci et al., 2001). Measurements of the cutoff energy have been difficult to obtain, since they require high-quality broadband X-ray spectral coverage above 10 keV. Previous studies of E_{cut} performed with non-focusing/collimating X-ray instruments in the hard X-ray band such as *CGRO/OSSE* (e.g., Rothschild et al., 1983; Zdziarski et al., 2000), *BeppoSAX* (e.g., Nicastro et al., 2000; Dadina, 2007) and *INTEGRAL* (e.g., Beckmann et al., 2009; Ricci et al., 2011; Malizia et al., 2014) had limited sensitivity and could only constrain E_{cut} for the brightest nearby AGN.

The launch of the *NuSTAR* observatory (Harrison et al., 2013) has transformed measurements of AGN cutoff energies. Being the first focusing hard X-ray telescope in orbit with spectral coverage up to 79 keV, *NuSTAR* has enabled E_{cut} to be constrained for many individual unobscured and obscured AGN (e.g., Ballantyne et al., 2014; Brenneman et al., 2014; Baloković et al., 2015; Kara et al., 2017; Xu et al., 2017). The *Swift*/BAT catalog (e.g., Gehrels et al., 2004; Baumgartner et al., 2013; Oh et al., 2018) provides a large sample of local, bright AGN with uniform sky coverage. Several studies have presented X-ray spectral analyses of *Swift*/BAT-selected AGN to investigate physical properties of the accreting supermassive black hole (SMBH). For example, Ricci et al. (2017b) performed a broadband spectral analysis of 836 *Swift*/BAT AGN and found a median cutoff energy for the entire sample of $E_{\text{cut}} = 200 \pm 29$ keV; however, these measurements did not use *NuSTAR* data and primarily utilised lower quality hard X-ray data from non-focusing instruments such as *Swift*/BAT. Kamraj et al. (2018) presented E_{cut} constraints for a sample of 46 *Swift*/BAT-selected Seyfert 1 AGN using ~ 20 ks exposure *NuSTAR* snapshot observations performed as part of the *NuSTAR* Extragalactic Legacy Surveys program¹. More recently, Baloković et al. (2020) presented E_{cut} constraints for obscured AGN selected from the *Swift*/BAT catalog, that also have short, 20 ks *NuSTAR* exposures.

In addition to constraining cutoff energies, *NuSTAR* has revitalized deeper exploration of AGN coronal parameters and their possible connection with the accretion properties of SMBH systems, such as the associated Eddington ratio. While some past studies of AGN that did not utilize *NuSTAR* measurements have found tentative

¹https://www.nustar.caltech.edu/page/legacy_surveys

correlations between median values of E_{cut} and accretion parameters such as the Eddington ratio (e.g., Ricci et al., 2018), studies of small samples of AGN observed with *NuSTAR* have shown no evidence for such a correlation (Tortosa et al., 2018).

In this paper, we present the first systematic study of the coronal properties of a large sample of unobscured AGN observed with *NuSTAR*. We use 195 observations of Seyfert 1 AGN selected from the *Swift*/BAT all-sky survey that also have snapshot *NuSTAR* legacy observations or long exposure targets observed as part of individual Guest Observer programs. We include simultaneous soft X-ray data from the *Swift*/XRT and *XMM-Newton* instruments where available. This study provides a combination of superior quality broadband X-ray data with a large sample size, enabling robust characterization of the physical properties of the corona in the local, unobscured AGN population.

This paper is structured as follows: in section 4.2, we describe the sample used in this work, the X-ray observations, and data reduction procedures; in section 4.3, we detail the various spectral models considered for fitting to the broadband X-ray data; in section 4.4, we present constraints on coronal temperatures for our sample and investigate the relation between parameters derived from spectral fitting and accretion properties such as Eddington ratio and black hole mass; we summarize our findings in section 4.5. We quote parameter uncertainties from spectral fitting at the 90% confidence level.

4.2 Sample, Observations, and Data Reduction

Seyfert 1 Sample

For this study, we selected sources by choosing AGN from the *Swift*/BAT 70-month X-ray catalog (Baumgartner et al., 2013). The all-sky catalog consists of AGN that are bright in the hard X-ray band (14–195 keV). Among these sources, we select AGN that are optically classified as Seyfert 1 (Sy1), a sample that contains sub-classes ranging from Sy1–Sy1.8, following the Osterbrock classification system (Osterbrock, 1981). The optical spectroscopic classification is derived from the BAT AGN Spectroscopic Survey (BASS;² Koss et al. (2017)). From this sample of unobscured AGN, we then selected sources that had been observed by *NuSTAR*, both as part of the Extragalactic Legacy Survey and Guest Observer program observations. Our final sample contains 195 Sy 1 AGN with redshifts in the range $0.002 < z < 0.2$. In addition to the *NuSTAR* observations, where available we

²<https://www.bass-survey.com/>

utilize simultaneous soft X-ray data in the 0.4–10 keV band taken with either the *Swift*/XRT or *XMM-Newton*/EPIC instruments.

NuSTAR

We performed reduction of the raw event data from both *NuSTAR* modules, FPMA and FPMB (Harrison et al., 2013) using the *NuSTAR* Data Analysis Software (NuSTARDAS, version 2.14.1), distributed by the NASA High-Energy Astrophysics Archive Research Center (HEASARC) within the HEASOFT package, version 6.27. We calculated instrumental responses based on the *NuSTAR* calibration database (CALDB), version 20180925. We cleaned and filtered raw event data for South Atlantic Anomaly (SAA) passages using the `nupipeline` module. We then extracted source and background spectra from the calibrated and cleaned event files using the `nuproducts` module. More detailed information on these data reduction procedures can be found in the *NuSTAR* Data Analysis Software Guide (Perri et al., 2017). Source spectra were extracted from circular regions with an extraction radius ranging from 30 to 60 depending on the source size and brightness. We extracted background spectra from source-free regions of the image on the same detector chip as the source, away from the outer edges of the field of view, which have systematically higher background.

XMM-Newton

In addition to the *NuSTAR* hard X-ray data, where available, we utilize simultaneous observations from the *XMM-Newton* observatory (Jansen et al., 2001) in the soft X-ray band taken with the EPIC-pn detector (Strüder et al., 2001). We have simultaneous *XMM-Newton* observations for 26 observations in our sample. We performed reduction of the raw *XMM-Newton* data using the *XMM-Newton* Science Analysis System (SAS, Gabriel et al., 2004, version 16.1.0), following the standard prescription outlined in the *XMM-Newton* ABC online guide.³ Calibrated, cleaned event files were created from the raw data files using the SAS command `epchain` for the EPIC-pn detector. As recommended, we only extracted single and double pixel events for EPIC-pn. Source spectra were extracted from the cleaned event files using the SAS task `xmmselect`. Background spectra were extracted from a circular aperture placed near the source on the same CCD chip. We checked for the presence of detector pileup using the SAS task `EPATPLOT`. Where significant pileup was detected in an observation, we used an annular extraction region in which the

³<https://heasarc.gsfc.nasa.gov/docs/xmm/abc/>

core of the source point spread function is excised in order to remove pileup. We generated instrumental response files using the SAS tasks `rmfgen` and `arfgen`.

Swift/XRT

For sources where simultaneous soft X-ray coverage with *XMM-Newton* was not available, we use simultaneous data taken with the *Swift*/XRT instrument (Burrows et al., 2005). We have simultaneous *Swift*/XRT observations for 149 observations in our sample. We reduced the *Swift*/XRT data using the ASDC XRT Online Analysis service⁴. We performed standard filtering using the `XRTPIPELINE` script following the guidelines detailed in Evans et al. (2009). We extracted background spectra from large annular regions around the source, taking care to avoid contamination. Instrumental ARF and RMF response files were generated using the `XRTPRODUCTS` script.

4.3 X-ray Spectral Modeling

We performed all spectral modeling of the broadband X-ray data using the XSPEC fitting tool (v12.11, Arnaud, 1996). We adopt cross sections from Verner et al. (1996) and solar abundances from Wilms et al. (2000). In all our model fitting, we include a Galactic absorption component modeled with the TBABS absorption code (Wilms et al., 2000), using Galactic column densities $N_{\text{H, Gal}}$ taken from the HI maps of the LAB survey (Kalberla et al., 2005). We also add a cross-normalization constant factor (c_{ins}) to all models to account for variability and calibration uncertainties across different instruments.

Model 1: Simple Absorbed Power Law

The first model we employ consists of a simple absorbed power law continuum with a high-energy cutoff E_{cut} . The power law continuum slope is characterized by the photon index Γ , with the intrinsic continuum flux proportional to $E^{-\Gamma} \exp(-E/E_{\text{cut}})$. In XSPEC notation, the model is given by $c_{\text{ins}} \times \text{TBABS} \times \text{ZPHABS} \times \text{CUTOFFPL}$, where `ZPHABS` models photoelectric host galaxy absorption. Figure 4.1 presents an example broadband X-ray spectrum for one of the sources in our sample, alongside residuals to the absorbed power law model fit to the data.

⁴<http://www.asdc.asi.it/mnia/index.php?mission=swiftmastr>

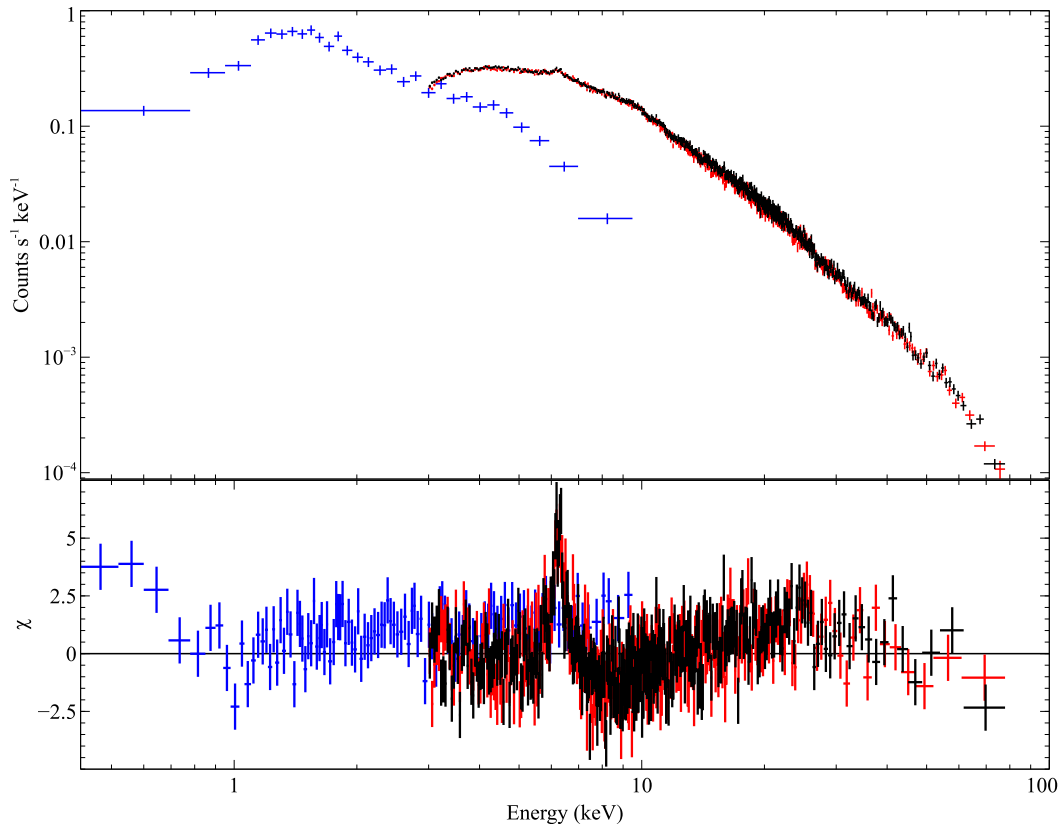


Figure 4.1: Broadband X-ray spectrum of IC4329A (top) alongside fit residuals for an absorbed cutoff power law model (bottom). Blue points represents *Swift*/XRT data while black and red points correspond to *NuSTAR* FPMA and FPMB data, respectively. Data points are re-binned for plotting clarity.

Model 2: Phenomenological Reflection (PEXRAV)

The second model we apply accounts for reflection features in the X-ray spectrum from reprocessing of the hard X-ray emission, such as the Fe $K\alpha$ line at a rest-frame energy of 6.4 keV and Compton reflection hump peaking around 20–30 keV (see e.g. Figure 4.1). We model these features using the phenomenological PEXRAV model (Magdziarz & Zdziarski, 1995), which assumes reflection off a slab of semi-infinite extent and optical depth. Our model expression in XSPEC is given by $c_{ins} \times \text{TBABS} \times \text{ZPHABS} \times (\text{CUTOFFPL} + \text{ZGAUSS} + \text{PEXRAV})$, where ZGAUSS models a Gaussian Fe $K\alpha$ line. We fix iron and light element abundances to solar values and fix the inclination angle of the plane of reflecting material at the default value of $\cos \theta = 0.45$. We tie the photon index and normalization of the reflected power law to that of the incident power law and fix the energy of the Fe $K\alpha$ line at 6.4 keV.

Model 3: Physical Reflection (XILLVERCP) Model

The final model we apply is an advanced reflection model that accurately models the physics of reprocessed radiation from the corona. We replace the PEXRAV component with the XILLVERCP model (García & Kallman, 2010), which forms part of the RELXILL family of disk reflection models (García et al., 2014). These models adopt a rich atomic database, fully calculate the angular distribution of the reflected radiation, and provide various geometrical models of the illuminating coronal source. The XILLVERCP model treats the coronal radiation incident on the disk as a thermally Comptonized continuum using the NTHCOMP code (Zdziarski et al., 1996) which vastly improves over a simple exponential cutoff power law continuum approximation. The model also self-consistently calculates the relative strength of the reflected emission, R , and the ionization parameter of the accretion disk, defined as $\xi = 4\pi F_X/n$ where F_X is the incident X-ray flux and n is the disk density. A disk density of 10^{15} cm^{-3} is assumed for the XILLVERCP model. Other key free parameters are the photon index Γ and the coronal electron temperature kT_e . We fix the inclination angle measured with respect to the disk normal at the default value of 30° . These advanced reflection models are able to provide constraints on the coronal temperature up to several hundred keV, past the limit of the *NuSTAR* detector bandpass, since the ionization state and disk structure are conditioned by the high-energy region of the spectrum, which in turn determines the observed reflection features (García et al., 2015).

Choice of Spectral Fitting Statistic

In our model fitting, we consider both χ^2 statistics and the Cash statistic (C-stat, Cash, 1979). While χ^2 statistics have traditionally been used as the primary fit statistic for X-ray spectral fitting, its usage is appropriate only when there are sufficient photon counts in a given energy bin such that the statistical variations can be approximated by a Gaussian distribution. Rebinning of spectra to achieve a Gaussian approximation can thus wash out key features in the X-ray spectrum, such as curvature at high energies from which estimations of E_{cut} are made. A more appropriate fit statistic to use, particularly when dealing with low photon counts, is C-stat, which maintains Poisson counting statistics and provides unbiased parameter estimation while still resembling a χ^2 statistic (Kaastra, 2017).

When applying χ^2 statistics, we rebinned the *NuSTAR* data to give a minimum of 20 photon counts per bin. For C-stat, we rebinned the data to have unity photon count per bin. We used the HEASOFT task `grppha` for all spectral binning. In Figure 4.2,

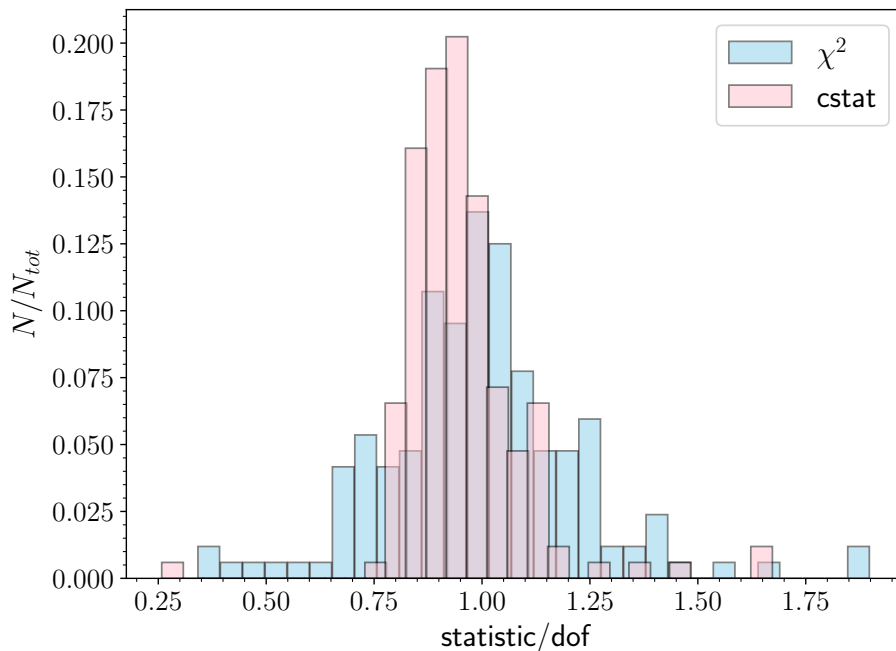


Figure 4.2: Distributions of the goodness-of-fit for the χ^2 and Cash statistics (C-stat) for an absorbed power law model fit (Model 1) to the broadband X-ray data for our entire sample.

we show the distribution of the goodness of fit (defined as the value of the fit statistic divided by the number of degrees of freedom) for both χ^2 and C-statistics, when applying the absorbed power law model fit to the data for our sample. We find that the distribution of the goodness of fit has a similar mean value for both types of statistic, indicating that C-stat provides an equally valid goodness of fit measure compared to χ^2 statistics. In addition, the goodness of fit is more tightly distributed around unity for C-stat, thus providing an overall better fit, motivating its usage as the primary fit statistic for our work.

4.4 Results and Discussion

Distribution of High Energy Cutoffs

We examined the distributions of coronal cutoff energies determined from broadband X-ray modeling (E_{cut} or kT_e depending on type of spectral model) for our full sample, considering both best-fit values and lower bounds. We first compared best-fit results for the χ^2 and C-stat distributions, and overall, we find improved constraints when using C-stat. Figure 4.3 shows the distributions of best-fit E_{cut} values for the absorbed power law model fit to the data for both χ^2 and C-stat. We observe that

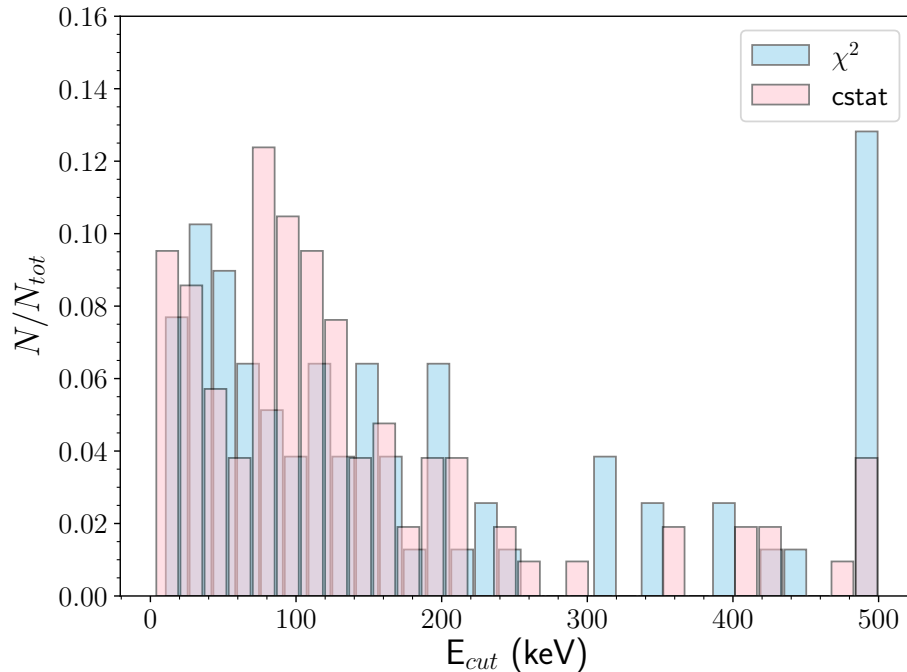


Figure 4.3: Distributions of the high energy cutoff E_{cut} for the χ^2 and Cash statistics (C-stat) for an absorbed power law model fit (Model 1) to the broadband X-ray data for our entire sample. We note that the model limit for the value of E_{cut} is 500 keV.

with the χ^2 statistic, a large number of sources have high energy cutoffs pegged at the upper limit of the model, leading to mean and median E_{cut} values that are skewed to higher energies. With C-stat, significantly fewer sources have best-fit coronal cutoff values at the upper limit of the model, producing average cutoffs that are lower and more closely resembling the true mean of the distribution, particularly since curvature in the spectrum at high energies associated with the coronal cutoff is not washed out, which can often be the case with the relatively wide energy bins necessary for χ^2 fitting.

We find full constraints on E_{cut} (both lower and upper limits) for 60 observations in our sample using C-stat, compared to 44 full E_{cut} constraints when performing spectral fitting with χ^2 for the absorbed power law model. For the PEXRAV model, we obtain full E_{cut} constraints for 91 observations with C-stat and 70 observations with χ^2 statistics. For the final XILLVERCP model, full constraints on kT_e are obtained for 79 observations with C-stat and 43 observations with χ^2 . In all cases, the number of full constraints on E_{cut} or kT_e is greater when applying the C-statistic compared to the χ^2 statistic. Furthermore, we note that while some individual AGN may have very high cutoff energies, e.g. Cen A (Fürst et al., 2016), generally average high

energy cutoffs of the AGN population cannot exceed several hundred keV as this would otherwise overproduce the cosmic X-ray background above 100 keV (Gilli et al., 2007; Ananna et al., 2019).

In Figure 4.4, we present distributions of coronal cutoff energies using C-stat for the three spectral models considered in this work. Overall, we find good agreement between the different spectral models for the mean value of E_{cut} . We determine the mean value of E_{cut} or kT_e from the best-fit distributions presented in Figure 4.4 (purple). We do not include best-fit values of E_{cut} or kT_e that are pegged at the upper limit of the spectral model (500 keV, 1 MeV and 400 keV for models 1, 2, and 3, respectively) in our determination of mean values, as such values typically result from XSPEC being unable to determine error bounds from the data. For the XILLVERCP model, assuming a conversion factor for $E_{\text{cut}} \sim 2\text{--}3 kT_e$ (Petrucci et al., 2001), the mean value of $kT_e = 84 \pm 9$ keV is consistent with the mean value of E_{cut} derived for spectral models 1 and 2, which were found to be 137 ± 12 keV and 156 ± 13 keV respectively. Table 4.1 presents example spectral fit constraints and source properties for some select objects from our sample.

We generally find good agreement when comparing our E_{cut} or kT_e results to similar measurements for unobscured AGN reported in the literature. For example, Ricci et al. (2017b) reported a median value of $E_{\text{cut}} = 210 \pm 36$ keV for unobscured AGN from the *Swift*/BAT 70-month catalog, determined from broadband spectral fitting of *Swift*/BAT and *Suzaku* data. In recent work by Molina et al. (2019) which studied *NuSTAR* spectra for a small sample of 18 broad-lined AGN selected with *INTEGRAL*, a mean value of $E_{\text{cut}} = 111 \pm 45$ keV was obtained for their sample, which is marginally consistent with our measurements given the large uncertainty.

Relation between the High Energy Cutoff and Accretion Parameters

We next explore possible relations between the cutoff energy/temperature and fundamental accretion properties of the SMBH, such as Eddington ratio (L/L_{Edd}) and mass of the SMBH (M_{BH}). We adopt black hole mass estimates from the second data release of optical measurements from the BASS survey (DR2: Broad-Line Based Black Hole Mass Estimates and Biases from Obscuration, Mejía-Restrepo et al., submitted). In addition to broad-line measurements from optical spectra, black hole mass estimates from the BASS survey have been compiled using several other techniques, such as stellar velocity dispersions, direct methods such as maser emission and reverberation mapping, and the $M_{\text{BH}} - \sigma_*$ relation of Kormendy & Ho

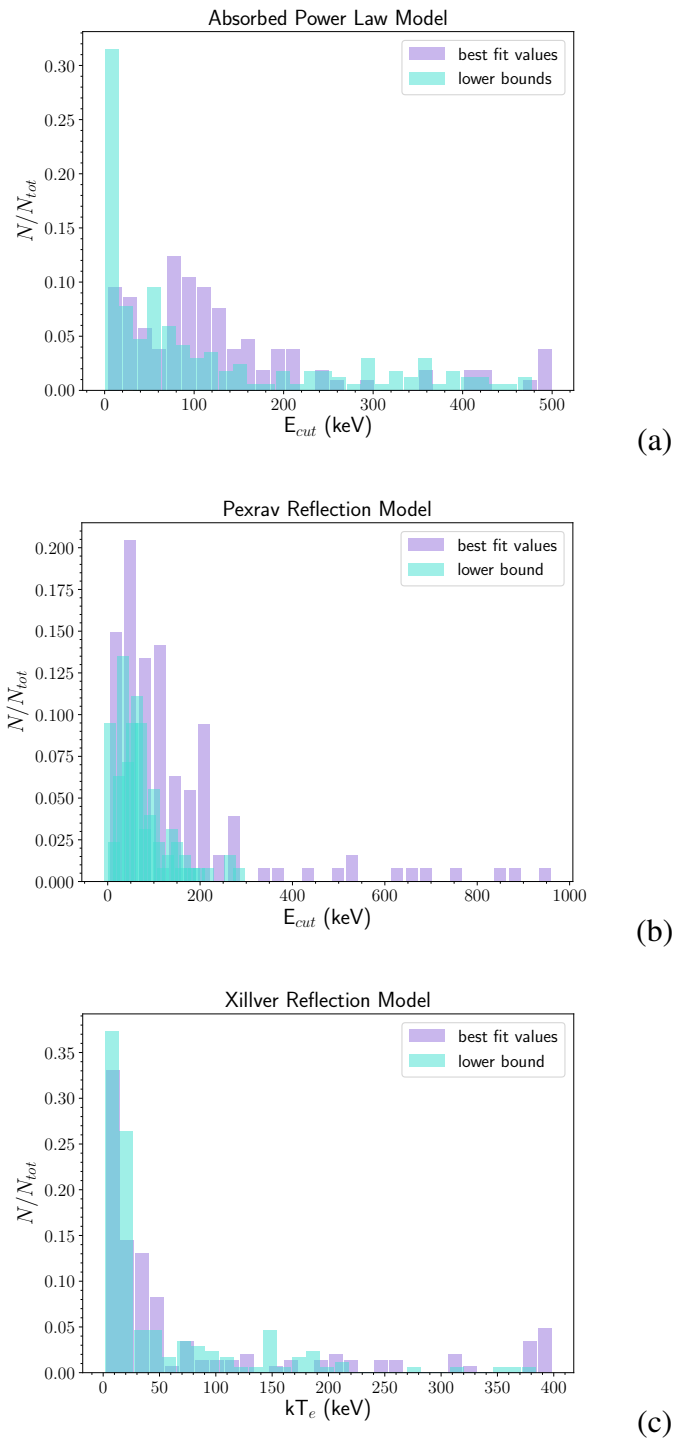


Figure 4.4: Distributions of the best-fit values and lower bounds of the high energy cutoff, E_{cut} , and coronal temperature, kT_e , for the different spectral models applied to the broadband X-ray data for our entire sample, using C-stat. Mean best-fit values of the coronal cutoff for the different spectral models, as determined from the purple histograms, are as follows: (a) $E_{cut} = 137 \pm 12$ keV, (b) $E_{cut} = 156 \pm 13$ keV, (c) $kT_e = 84 \pm 9$ keV.

Table 4.1: Redshifts, black hole masses and best-fit spectral parameters from fitting broadband X-ray data for select sources from our sample of *Swift*/BAT-selected Sy1s.

Source	Redshift	$\log(M_{\text{BH}}/M_{\odot})^A$	Γ	E_{cut} (keV)	kT_e (keV)	C-stat/dof	Model ^B
Fairall 1203	0.058	8.20	$1.24^{+0.15}_{-0.17}$	42^{+51}_{-16}	-	1052/1192	1
			$1.45^{+0.23}_{-0.19}$	≥ 45	-	186/247	2
			$1.56^{+0.05}_{-0.04}$	-	15^{+39}_{-4}	1043.5/1189	3
IC 4329A	0.016	7.81	$1.69^{+0.004}_{-0.01}$	≥ 394	-	4955/4179	1
			1.72 ± 0.01	170^{+23}_{-18}	-	2698/2706	2
			$1.77^{+0.01}_{-0.004}$	-	82^{+16}_{-7}	4275.7/4210	3
MCG-3-4-72	0.046	7.09	1.73 ± 0.05	117^{+223}_{-48}	-	1554/1642	1
			1.95 ± 0.06	123^{+596}_{-59}	-	748.5/749	2
			$1.73^{+0.04}_{-0.05}$	-	15^{+23}_{-4}	1537/1654	3
Mrk 1148	0.064	8.01	$1.73^{+0.05}_{-0.04}$	81^{+59}_{-18}	-	2138/2262	1
			1.89 ± 0.04	≥ 85	-	1477/1633	2
			$1.78^{+0.04}_{-0.03}$	-	≥ 18	2167.5/2290	3
RBS 542	0.104	7.89	1.61 ± 0.02	74^{+14}_{-10}	-	3389.8/3251	1
			1.64 ± 0.03	49^{+7}_{-5}	-	1658/1570	2
			$1.70^{+0.03}_{-0.02}$	-	≥ 16	3253/3257	3

Information presented in this table is available for our full sample in machine-readable form upon request.

^A Reference: Mejía-Restrepo et al., submitted (BASS XXII DR2: Broad-line Based Black Hole Mass Estimates and Biases from Obscuration).

^B Applied XSPEC models: (1) $c_{\text{ins}} \times \text{TBABS} \times \text{ZPHABS} \times \text{CUTOFFPL}$
(2) $c_{\text{ins}} \times \text{TBABS} \times \text{ZPHABS} \times (\text{CUTOFFPL} + \text{ZGAUSS} + \text{PEXRAV})$
(3) $c_{\text{ins}} \times \text{TBABS} \times \text{ZPHABS} \times (\text{XILLVERCP} + \text{ZGAUSS})$

(2013). The Eddington luminosity L_{Edd} for pure H composition is given by:

$$L_{\text{Edd}} = \frac{4\pi G M_{\text{BH}} m_p c}{\sigma_T} \quad (4.2)$$

where G is the gravitational constant, c is the speed of light, and σ_T is the Thompson scattering cross section. We calculate the Eddington ratio L/L_{Edd} using the bolometric AGN luminosity, determined from the intrinsic X-ray luminosity in the 2–10 keV band, applying a bolometric correction factor of 20 to the 2–10 keV luminosity (Vasudevan & Fabian, 2009).

Figure 4.5 presents the lower bound of E_{cut} or kT_e versus Eddington ratio for the three spectral models considered. Since our sample contains a large number of

sources with either partial constraints or lower limits on the coronal cutoff energy, for consistency we examine the trend in the lower bounds of E_{cut} or kT_e across the entire sample. While our sample includes some strong constraints for bright AGN with long *NuSTAR* exposures, as noted in Baloković et al. (2020), for large sample statistics, such lower bound constraints are more informative than analysis of a small number of tightly constrained limits. Recently, Akylas & Georgantopoulos (2021) studied the coronal cutoffs in *Swift*/BAT-selected Sy 1 AGN using *NuSTAR* data, incorporating techniques similar to Baloković et al. (2020) that allow them to take the numerous lower limits on E_{cut} into account. Best-fit values of E_{cut} or kT_e obtained from spectral fitting with XSPEC can fluctuate between the upper and lower bounds with refitting, thus the lower bound presents a more robust constraint. We also note lower bounds on the cutoff energy that lie well outside the *NuSTAR* bandpass should be considered with due caution, due to uncertainties in spectral modeling combined with limitations in data quality for some sources. For example, Matt et al. (2015) found $E_{\text{cut}} = 720_{-190}^{+130}$ keV when fitting the *NuSTAR* spectrum of NGC 5506 with a relativistic reflection model. However, Baloković et al. (2020) found $E_{\text{cut}} = 110 \pm 10$ keV for NGC 5506 when fitting the same *NuSTAR* data with a slightly different spectral model. Despite the improved sensitivity of broadband spectra taken with *NuSTAR* and usage of more physically accurate reflection models, the extrapolation of Comptonization spectra to energies above the bandpass of *NuSTAR* presents large uncertainties and are overall difficult to predict above 100 keV (e.g., Niedźwiecki et al., 2019; Zdziarski et al., 2021).

We do not find a significant correlation between the lower bound of the coronal cutoff and Eddington ratio for the full sample, with p-values exceeding 1 % when applying a Spearman rank correlation test to both individual points and binned data. We also investigated the dependence of the coronal cutoff on the mass of the AGN SMBH (M_{BH}). Figure 4.6 shows the results for different spectral models. While we find a declining trend in the mean lower bound of E_{cut} with M_{BH} for the absorbed power law model, with a p-value of 0.004%, we do not find any statistically significant correlation for the two reflection models (p-value > 10%), which more accurately characterize the AGN emission compared to the simple power law fit.

Comparing our results with similar studies of coronal parameters by Ricci et al. (2018) using pre-*NuSTAR* broadband X-ray data, we find some differences. Ricci et al. (2018) find a negative trend in the median value of E_{cut} with Eddington ratio for their sample of 211 unobscured AGN, including lower limits. However

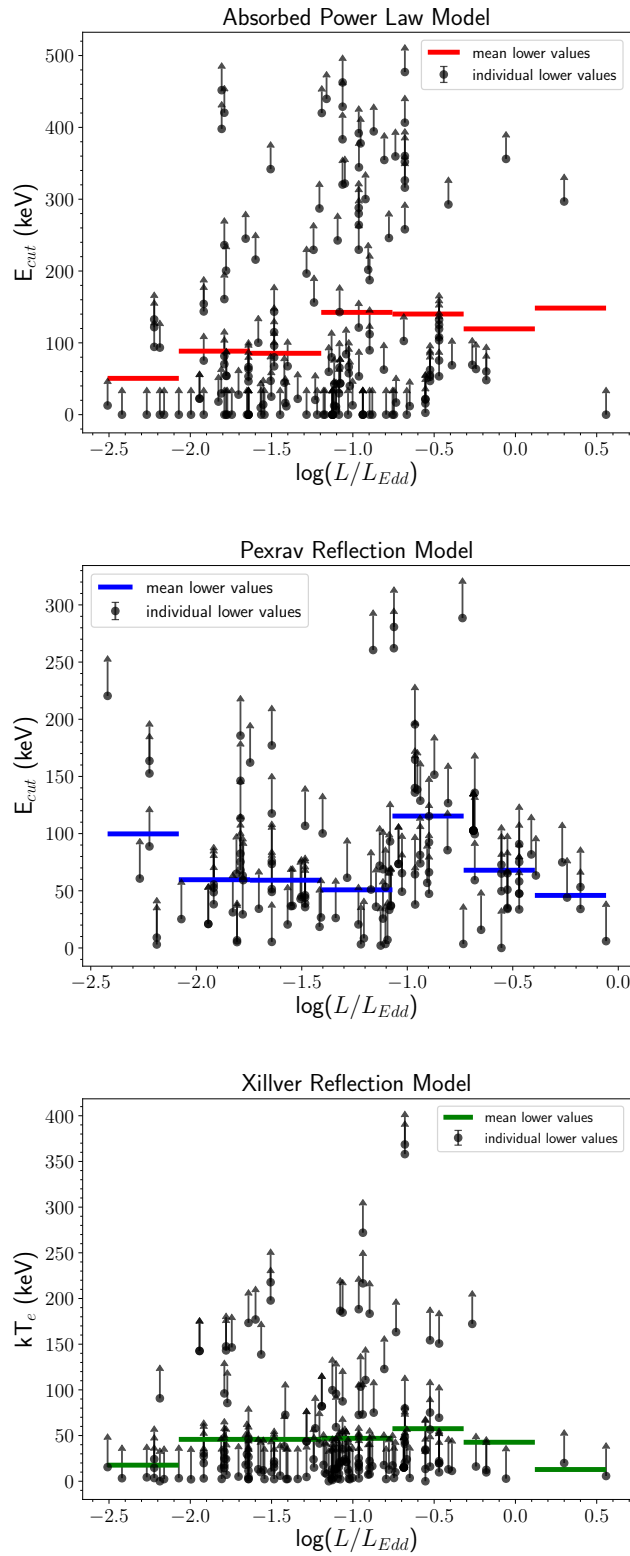


Figure 4.5: Lower bounds of E_{cut} and kT_e versus the Eddington ratio L/L_{Edd} for different X-ray spectral models applied to our entire sample, using C-stat. Solid horizontal lines represent mean values of E_{cut} or kT_e for different intervals of L/L_{Edd} .

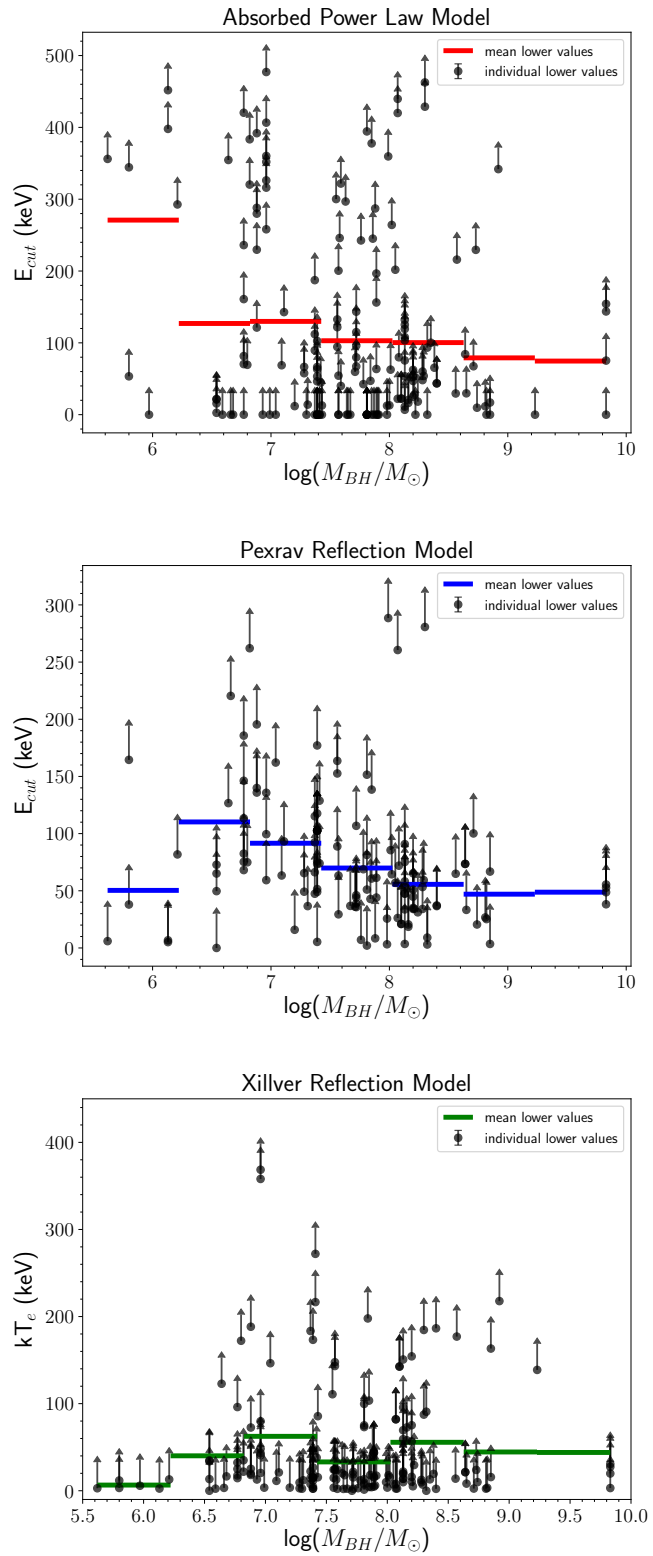


Figure 4.6: Lower bounds of E_{cut} and kT_e versus SMBH mass M_{BH} for different X-ray spectral models applied to our entire sample, using C-stat. Solid horizontal lines represent mean values of E_{cut} or kT_e for different intervals of M_{BH} .

no significant correlation is found between E_{cut} and Eddington ratio when lower limits are ignored in their sample. While they observe a possible trend between E_{cut} and M_{BH} , such a correlation disappears when dividing the sources into bins of different Eddington ratio. Tortosa et al. (2018) studied coronal parameters in a sample of 19 *Swift*/BAT-selected Seyfert 1 galaxies observed with *NuSTAR*, and found no correlation between the high energy cutoff and SMBH mass or Eddington ratio. In another study, Molina et al. (2019) examined X-ray spectra of 18 broad-lined AGN selected with *INTEGRAL* and observed with *NuSTAR*. They found no correlation between the high energy coronal cutoff and Eddington ratio. In a more recent study by Hinkle & Mushotzky (2021), which examined coronal parameters in a sample of 33 *Swift*/BAT-selected Sy1 and Sy2 AGN observed with *NuSTAR* and *XMM-Newton*, no strong correlation was found between cutoff energy and SMBH mass or Eddington ratio. Therefore, we demonstrate that, when fitting high quality broadband X-ray spectra obtained with *NuSTAR* for large samples of AGN, we do not find a strong correlation between the coronal cutoff and AGN accretion parameters such as Eddington ratio and SMBH mass.

The $\Gamma - L/L_{\text{Edd}}$ Relation

Next, we investigate the relationship between the X-ray photon index and Eddington ratio, hereafter referred to as the $\Gamma - L/L_{\text{Edd}}$ relation. Numerous studies report a positive linear correlation between these two parameters of the form

$$\Gamma = \Psi \log\left(\frac{L}{L_{\text{Edd}}}\right) + \omega. \quad (4.3)$$

Early studies of individual sources and small samples of AGN hinted at a correlation between Γ and L_{Edd} (e.g., Pounds et al., 1995; Brandt et al., 1997), though such studies probed a very limited range of AGN luminosities. Studies covering a wider range of luminosities and redshifts such as Shemmer et al. (2006, 2008) and Brightman et al. (2013) identified a statistically significant correlation between Γ and L_{Edd} , with a slope $\Psi \sim 0.3$. However, Sobolewska & Papadakis (2009) performed detailed spectral analysis of 10 *RXTE*-observed AGN and found Ψ to vary from object to object, with a flatter average slope $\Psi = 0.08$. Yang et al. (2015) constructed a large sample of AGN and black hole binaries covering a wide luminosity range, and found Γ to be constant at very low luminosities, but varied from being positively and negatively correlated over certain luminosity ranges. Recent studies by Trakhtenbrot et al. (2017) which examined the $\Gamma - L/L_{\text{Edd}}$ relation for 228 *Swift*/BAT AGN, have

also reported flatter slopes ($\Psi \sim 0.15$), with overall large scatter in the relation. Furthermore, the authors found no evidence for a $\Gamma - L/L_{\text{Edd}}$ correlation for subsets of AGN with reliable, direct BH mass estimates. Ricci et al. (2013) also found a similarly flat slope ($\Psi = 0.12$) for their sample of 36 *Chandra*-observed AGN. In Trakhtenbrot et al. (2017), the authors only recover the steeper slope consistent with earlier studies ($\Psi \sim 0.3$) when applying a simple power law model fit to the subset of broad-lined AGN in their sample. These results demonstrate that the $\Gamma - L/L_{\text{Edd}}$ relation may not be robust or universal, with the strength of the correlation varying with choice of sample, luminosity ranges of the sample, energy range of X-ray data used in analysis, and type of X-ray spectral model used in determining Γ .

In our work, we examined the $\Gamma - L/L_{\text{Edd}}$ relation for our full sample for all three X-ray spectral models used in our analysis. We also investigated whether there was a dependence of the slope of the relation on the type of X-ray spectral model fitted to the broadband data. We present our results for the $\Gamma - L/L_{\text{Edd}}$ relation in Figure 4.7, showing Γ values for the XILLVER reflection model, which most accurately characterizes the AGN X-ray emission. Overall, we find considerable scatter and no strong trend between Γ and L_{Edd} for all spectral models that we applied. Applying a formal Spearman rank test confirmed the absence of a statistically significant correlation, with correlation coefficients less than 0.25 and p-values exceeding 0.2%. We find no strong correlation when dividing the data into bins of Eddington ratio (purple lines in Figure 4.7). When applying a simple linear regression fit to the data for each X-ray spectral model, we obtain very flat slopes: $\Psi \sim 0.03 - 0.06$. Comparing to the literature, our slopes for the $\Gamma - L/L_{\text{Edd}}$ relation are much flatter than previously reported results, as we find little evidence for a correlation between Γ and L_{Edd} . We conclude that when analyzing a large, unbiased sample of unobscured AGN with high sensitivity broadband X-ray spectral data, we do not find robust evidence for a $\Gamma - L/L_{\text{Edd}}$ correlation and caution on the usage of such a relation to derive estimates of L_{Edd} or M_{BH} .

Location of Sources in the Compactness–Temperature Plane

Using our constraints on the coronal temperature, we constructed a compactness–temperature ($l - \theta$) diagram using sources from our sample. θ is defined to be a dimensionless parameter for coronal temperature: $\theta = kT_e/m_e c^2$. In constructing the $l - \theta$ plane, we use kT_e values obtained from the XILLVER spectral model fit to the X-ray data. This eliminates the uncertainty in determining θ from E_{cut} values, since the conversion from E_{cut} to kT_e varies depending on the optical depth of the

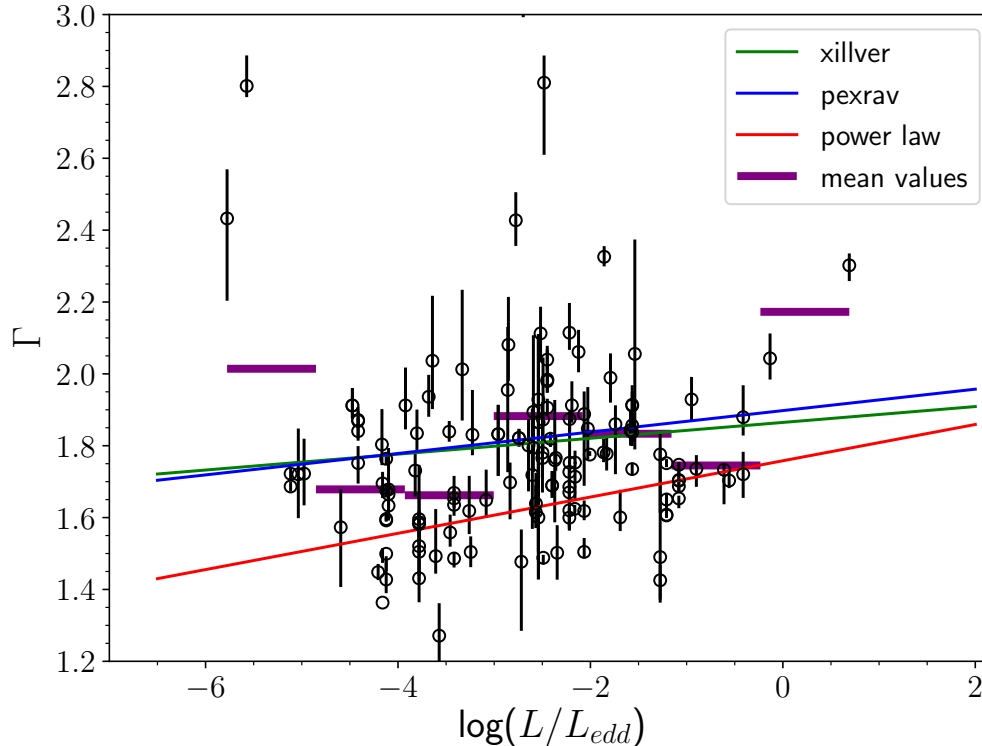


Figure 4.7: The $\Gamma - L/L_{\text{Edd}}$ relation for our full sample. Solid lines show linear fits to the data for the three different X-ray spectral models applied in this work. Marked in purple are mean values of Γ for different bins of Eddington ratio for the XILLVER reflection model.

corona (Petrucci et al., 2001), which can vary from source to source. In determining values of l , we assume a conservative value of $10R_g$ for the coronal radius (Fabian et al., 2015).

Figure 4.8 presents compactness–temperature diagrams for the AGN in our sample for which black hole mass estimates are available. We plot several pair production lines corresponding to different coronal geometries. Treating the corona as an isolated cloud, Svensson (1984) calculated the pair production line to have an analytical form $l \sim 10\theta^{5/2}e^{1/\theta}$, which is shown in solid cyan in our $l - \theta$ plots. We also mark pair production lines for a slab and hemispherical corona located above a reflecting accretion disk computed from Stern et al. (1995) (black and purple lines, respectively in Figure 4.8). In the top panel of Figure 4.8, the dashed lines correspond to the boundaries where electron-electron (black) and electron-proton (green) processes dominate over Compton cooling (Ghisellini et al., 1993; Fabian, 1994). The lower plot show the distribution of sources on the $l - \theta$ plane individually color coded by black hole mass.

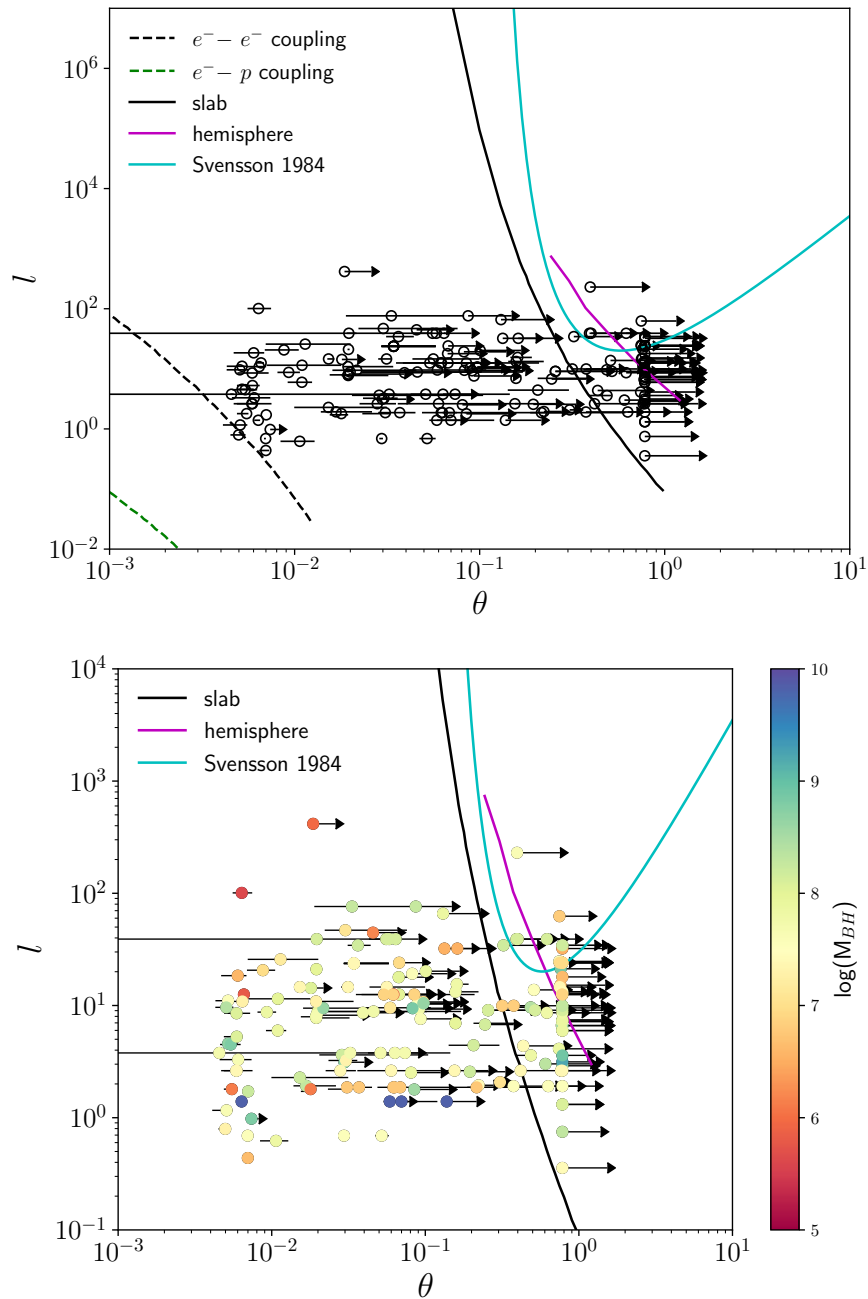


Figure 4.8: Compactness–Temperature ($l - \theta$) diagrams for our full sample, with θ determined using kT_e values from the XILLVER model fit to data. Solid lines correspond to pair production lines for different coronal geometries. The dashed lines in the top panel correspond to boundaries where regions are dominated by electron-electron and electron-proton coupling processes. Data points in the bottom panel plot are color coded by SMBH mass.

These $l - \theta$ measurements for our large sample of *NuSTAR*-observed AGN generally show sources to be widely distributed in both temperature and radiative compactness, in contrast to previous measurements for smaller samples of AGN where sources appeared to cluster near the pair production lines (e.g., Fabian et al., 2015; Kamraj et al., 2018). The results from Ricci et al. (2018), which mapped the $l - \theta$ plane for 211 unobscured *Swift*/BAT AGN, show a distribution of individual sources fairly similar to our results.

In general, the existence of AGN with low coronal temperatures is rather enigmatic, as the mechanisms behind coronal cooling in such sources are not well understood. Identification of AGN with low coronal temperatures is not uncommon, with findings of high energy cutoffs within the *NuSTAR* band reported in the literature in recent years (e.g., Kara et al., 2017; Xu et al., 2017; Kamraj et al., 2019). Various theories have been proposed for possible cooling mechanisms to account for such low temperatures within the corona. Weak coronal heating mechanisms are a possibility, considering that it has been a longstanding open problem of supplying energy to the corona when it is established that the cooling timescale is shorter than the light crossing timescale (e.g., Ghisellini et al., 1993; Merloni & Fabian, 2001). Low coronal temperatures could also be produced from a high optical depth within the corona. For optical depths exceeding unity, multiple inverse Compton scatterings of photons originating from the accretion disk could lead to effective coronal cooling (Kara et al., 2017). However, we have thus far assumed the corona is homogeneous, fully thermal, and at a single temperature, whereas in reality the corona is a dynamic structure and can have a range of temperatures (Fabian et al., 2015). It is possible that the corona is a hybrid plasma, containing both thermal and non-thermal particles (e.g., Zdziarski et al., 1993; Ghisellini et al., 1993). Fabian et al. (2017) have shown through hybrid plasma simulations that a small fraction of non-thermal electrons with energies above 1 MeV can reduce the temperature of the corona, as electron-positron pairs redistribute their energy and reduce the mean energy per particle.

Our $l - \theta$ measurements improve over previously reported studies by combining both a large sample size of AGN with high quality *NuSTAR* broadband X-ray data with improved spectral modeling for determination of coronal temperatures. By using the *XILLVERCP* spectral model, we obtain more accurate estimates of kT_e , since the high energy turnover in the intrinsic continuum is modeled as a Comptonized spectrum instead of the common exponential power law cutoff. Past works such as

Zdziarski et al. (1993) and Fabian et al. (2015) have shown that a simple exponential cutoff approximation produces a slower break in the X-ray spectrum compared to a Comptonized continuum, which retains a power law shape to higher X-ray energies before more rapidly turning over. Thus, an exponential cutoff approximation can lead to overestimates of the coronal temperature.

We note that higher order effects can affect the precise location of sources on the $l - \theta$ plane. Most notably, general relativistic effects such as gravitational redshift and light bending can affect estimates of l and θ . For example, light bending can boost intrinsic values of l and enhance Compton cooling, thereby moving pair lines to lower θ . However, such corrections are highly dependent on properties such as disk inclination and coronal geometry, both of which are highly uncertain. Hence, we do not attempt to model general relativistic effects in this work due to the large uncertainties associated with such corrections.

Optical Depth of the Coronal Plasma

In this final section, we report on the investigation of other AGN parameters derived from broadband X-ray spectral fit results for our full sample. Specifically, we focus on determining the optical depth of the plasma in the corona (τ) and its relation to the Eddington ratio. The optical depth is not a parameter that is directly determined from X-ray spectral fitting, but it can be derived from Γ and kT_e according to the following equation given in Petrucci et al. (2001) for a plane-parallel corona and formally valid for $\tau \gtrsim 1$:

$$\Gamma = \sqrt{\frac{9}{4} + \frac{511 \text{ keV}}{\tau kT_e (1 + \tau/3)}} - \frac{1}{2}. \quad (4.4)$$

We use best-fit values of kT_e found from the XILLVERCP reflection model to solve for τ according to Equation 4.4. We find that the median and mean optical depths for our entire sample are $\tau = 3.04 \pm 1.73$ and $\tau = 4.84 \pm 1.80$, respectively. We note that a large number of sources in our sample have only a lower limit on kT_e , so the values of τ presented in this work should be viewed as upper limits. We also note that parameter degeneracies, particularly in the kT_e - Γ plane, can lead to very high values of τ . Spectral fits that produce very low values of kT_e accompanied by low values of Γ do not correspond to physically realistic conditions within the coronal plasma (e.g., Stern et al., 1995; Poutanen & Svensson, 1996). In Figure 4.9, we show best-fit values of kT_e and Γ along with curves of constant τ defined using

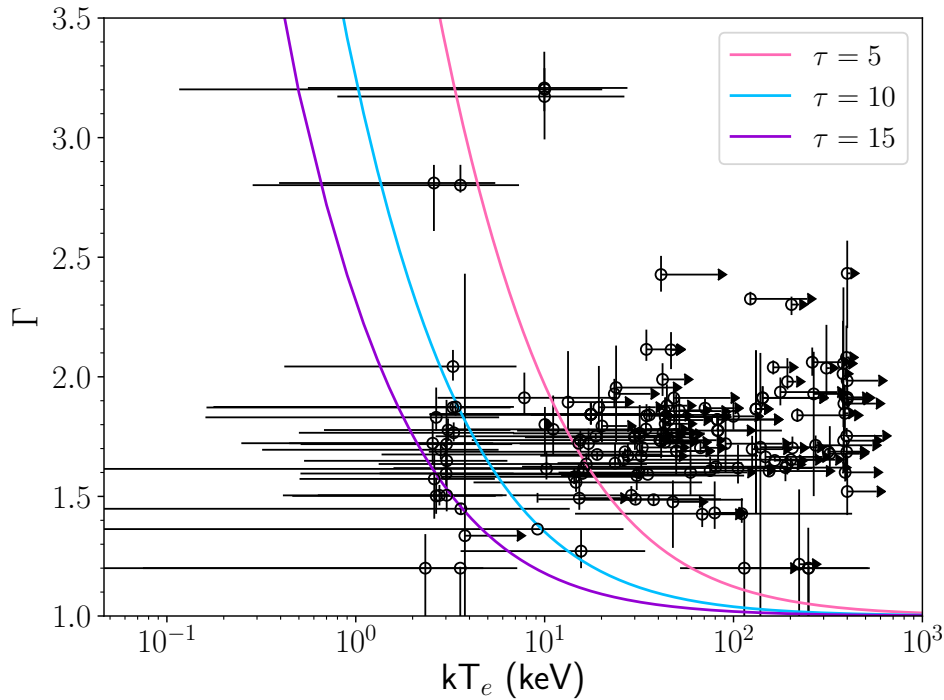


Figure 4.9: kT_e and Γ values obtained from the XILLVER spectral model fit to the data. Solid colored lines correspond to theoretical constraints from Petrucci et al. (2001) for different values of coronal plasma optical depth τ .

Equation 4.4. We observe that while there is some degree of degeneracy present in the kT_e – Γ plane, the majority of sources lie above the line roughly corresponding to the mean value of τ for our sample.

For sources with full constraints on kT_e , we performed Monte Carlo sampling as a rough estimate of the uncertainty in derived values of τ . We drew 1000 random samples of kT_e and Γ , assuming a mean and variance of the random sample taken from the observed respective distributions. We found no difference in the distributions of τ determined from the randomly sampled values of kT_e and Γ when assuming different underlying types of distribution (e.g. Gaussian vs. Poissonian).

In Figure 4.10 we present results for τ against the Eddington ratio, with each source color-coded by its best-fit value of kT_e . We do not find a statistically significant correlation between τ and L/L_{Edd} for individual data points or when binning the data by L/L_{Edd} , similar to results from Ricci et al. (2018). From Figure 4.10 we also observe a trend of increasing optical depth with decreasing coronal temperature. Tortosa et al. (2018) also found a negative correlation between the plasma optical

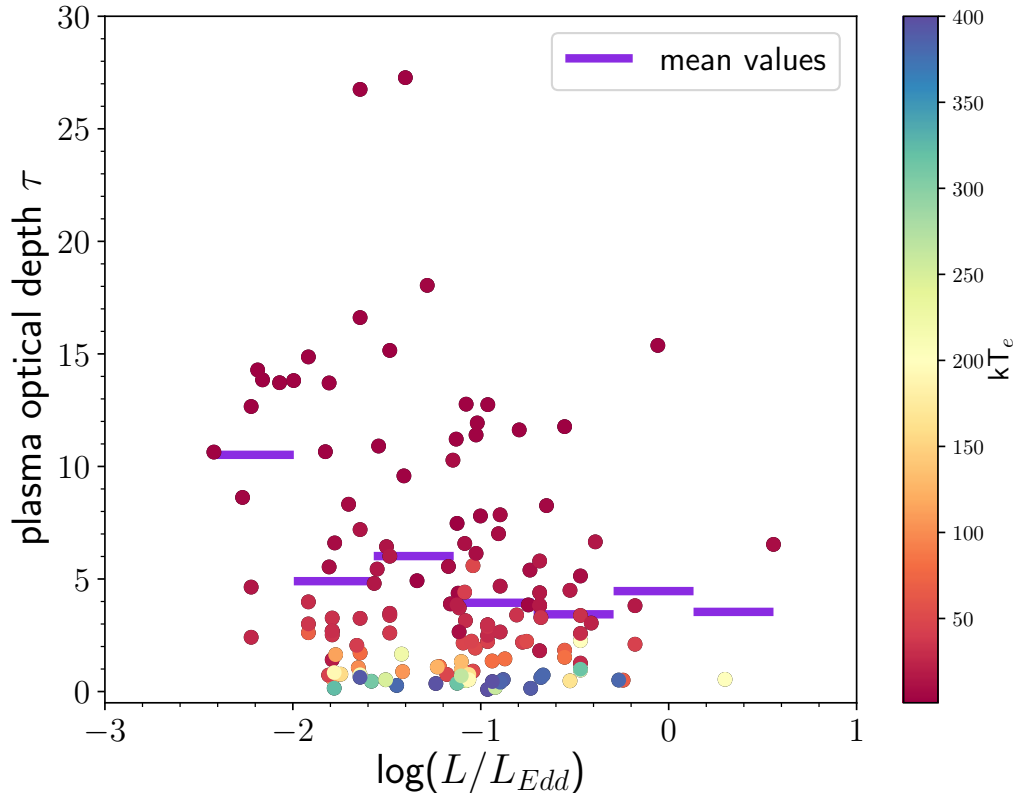


Figure 4.10: Coronal plasma optical depth τ versus the Eddington ratio L/L_{Edd} for our entire sample. Optical depth was derived from kT_e and Γ values obtained from the XILLVER spectral model fit to the data. Horizontal purple lines correspond to mean values of τ for different bins of Eddington ratio. Data points are color-coded by their corresponding kT_e value found from X-ray spectral fitting.

depth and coronal temperature for their sample of 19 *NuSTAR*-observed Seyfert 1 galaxies. This observed trend in τ with L/L_{Edd} supports the hypothesis mentioned in Section 4.4 for low temperature coronae possibly possessing high optical depths, thus enhancing coronal cooling.

4.5 Summary

In this work, we have compiled a large sample of Seyfert 1 AGN with high quality broadband X-ray spectra taken with the *NuSTAR* observatory and studied fundamental properties of the coronal plasma that powers the continuum X-ray emission in AGN. We performed detailed broadband X-ray spectral modeling for all sources in our sample from which we obtained constraints on the temperature of the corona. From fitting a more physically accurate advanced reflection model, we find the mean coronal temperature to be $kT_e = 84 \pm 9$ keV, which is generally consistent with other

measurements of high energy cutoffs for unobscured AGN reported in the literature.

When investigating the relationship between the coronal temperature and accretion parameters such as the Eddington ratio and AGN SMBH mass, we do not find any strong correlations. We also examined the well-known $\Gamma - L/L_{\text{Edd}}$ relation, and found no statistically significant correlation, with little variation in the slope of the relation with the choice of X-ray spectral model used to determine Γ . We thus caution on the use of such relations previously presented in the literature to derive distributions of L/L_{Edd} or M_{BH} .

We studied the distribution of sources in our sample across the compactness–temperature plane and find that AGN span a wide range of coronal temperatures and are not strictly confined to the boundary lines corresponding to runaway pair production. A number of sources appear to have fairly low coronal temperatures, which may arise from large optical depths of the coronal plasma, as we observe the optical depth of sources in our sample to increase with decreasing values of the coronal temperature. Another possibility is that the corona is a hybrid plasma system, where the presence of a population of non-thermal electrons can act to reduce the temperature of the plasma. Future studies that can apply advanced hybrid plasma models to high quality broadband AGN X-ray spectral observations performed with *NuSTAR* or concept X-ray missions such as *HEX-P* (Madsen et al., 2019), may be able to robustly test the possibility of such a physical scenario producing a low temperature corona.

4.6 Acknowledgments

We have made use of data from the *NuSTAR* mission, a project led by the California Institute of Technology, managed by the Jet Propulsion Laboratory, and funded by the National Aeronautics and Space Administration. We thank the *NuSTAR* Operations, Software and Calibration teams for support with the execution and analysis of these observations. This research has made use of the following resources: *NuSTAR* Data Analysis Software (NuSTARDAS) jointly developed by the ASI Science Data Center (ASDC, Italy) and the California Institute of Technology (USA); online *Swift* data processing services provided by the SSC; the High Energy Astrophysics Science Archive Research Center Online Service, provided by the NASA/Goddard Space Flight Center; NASA’s Astrophysics Data System; and Astropy, a community-developed core Python package for Astronomy (Astropy Collaboration et al., 2013, 2018). Some of the optical spectra used for determining black hole masses used in

this work were taken with the Doublespec (DBSP) instrument at Palomar via Yale (PI M. Powell, 2017-2019, 16 nights) as well as Caltech (PI F. Harrison) and JPL (PI D. Stern) from programs from 2013-2020.

M. Baloković acknowledges support from the Black Hole Initiative at Harvard University, which is funded in part by the Gordon and Betty Moore Foundation (grant GBMF8273) and in part by the John Templeton Foundation, as well as support from the YCAA Prize Postdoctoral Fellowship. M.K. acknowledges support from NASA through ADAP award NNH16CT03C. K.O. acknowledges support from the National Research Foundation of Korea (NRF-2020R1C1C1005462). C.R. acknowledges support from the CONICYT+PAI Convocatoria Nacional subvencion a instalacion en la academia convocatoria año 2017 PAI77170080.

Chapter 5

FUTURE STUDIES

5.1 Studies of X-ray Obscured Type 1 AGN in the *Swift*/BAT Survey

As outlined in Section 1.3 and studied in Chapter 3, the existence of AGN that show conflicting optical and X-ray classifications remain an enigmatic phenomenon, motivating further study of such rare classes of objects. A small number of AGN in the *Swift*/BAT catalog exhibit a mismatch between their X-ray and optical classifications, making such a sample a prime target for future studies aimed at understanding the nature of the complex obscuration present in these sources.

The BAT AGN Spectroscopic Survey (BASS, www.bass-survey.com) is a comprehensive, multi-wavelength effort to construct the most complete census of supermassive black hole activity in the local universe, through the analysis of over 850 unique *Swift*/BAT hard X-ray detected (14-195 keV) AGN including absorption and emission line measurements, black hole masses, and accretion rates (Koss et al., 2017). Optical spectroscopy and X-ray observations with facilities such as *NuSTAR* are key components of the BASS survey, with several hundred of the sources already observed by each of the facilities. In the BASS sample, there is excellent agreement between the optical and X-ray classifications for $> 95\%$ of sources. However, a number of exotic sources have been identified in the BASS survey that show disagreement between their optical and X-ray classification. In future work, I propose to study optically unobscured, Type 1 AGN from this sample that are X-ray obscured, of which there are approximately 20 such sources in the *Swift*-BAT 70-month hard X-ray catalog (see Figure 5.1). Shimizu et al. (2018) found that 14 % of Sy1 - 1.9 AGN in the BASS sample are X-ray absorbed, with the inferred columns determined from visual extinction (A_V) being orders of magnitude less than the column densities measured from fitting X-ray spectra (see Figure 5.2). However, their sample included a large number of Sy1.9 AGN ($\sim 70\%$), which are typically highly X-ray obscured in nature with large viewing angles and generally have spectra resembling those of Type 2 AGN. Hence we would limit our sample for study to Sy1-1.8 AGN, for which we would not typically expect high X-ray absorbing column densities.

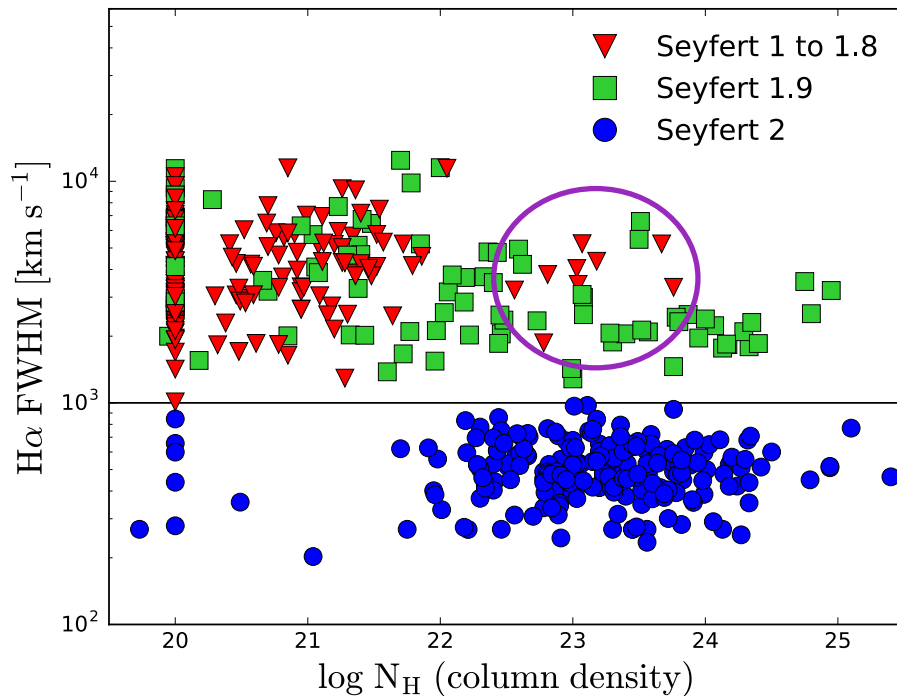


Figure 5.1: $H\alpha$ line width (FWHM) vs. Hydrogen column density (N_H), for AGN from the BASS survey (Koss et al., 2017). Colors represent the Osterbrock classification of AGN. Circled are some of the outlier Sy 1-1.8 sources in the sample (red triangles), that have high X-ray obscuration ($N_H \gtrsim 10^{23} \text{ cm}^{-2}$). Sources clustered along $N_H = 10^{20} \text{ cm}^{-2}$ correspond to upper limits on the column density.

5.2 Spectropolarimetry of X-ray Obscured Type 1 AGN

One idea proposed for the nature of the X-ray obscuration in optically unobscured AGN, and is indeed likely to be the case in the source 2MASX J19301380+3410495 studied in this thesis, is the presence of dust-free gas within the sublimation radius of the BLR contributing to the extra X-ray obscuration. Another possible simple explanation from a geometrical viewpoint, is scattering of the broad line region photons into our line of sight through a region of lower column density than what obscures the X-ray emission (Hogg et al., 2012). In future studies, I propose to test such a physical scenario for the BASS sample of obscured Type 1 AGN using spectropolarimetric observations. By obtaining polarization spectra of such exotic objects, it will be possible to confirm whether scattering in the BLR is a likely mechanism for explaining the discrepancy between X-ray and optical classifications in these sources. Specifically, we expect that a strong polarization signal will be seen at wavelengths corresponding to broad lines, whereas no significant polarization

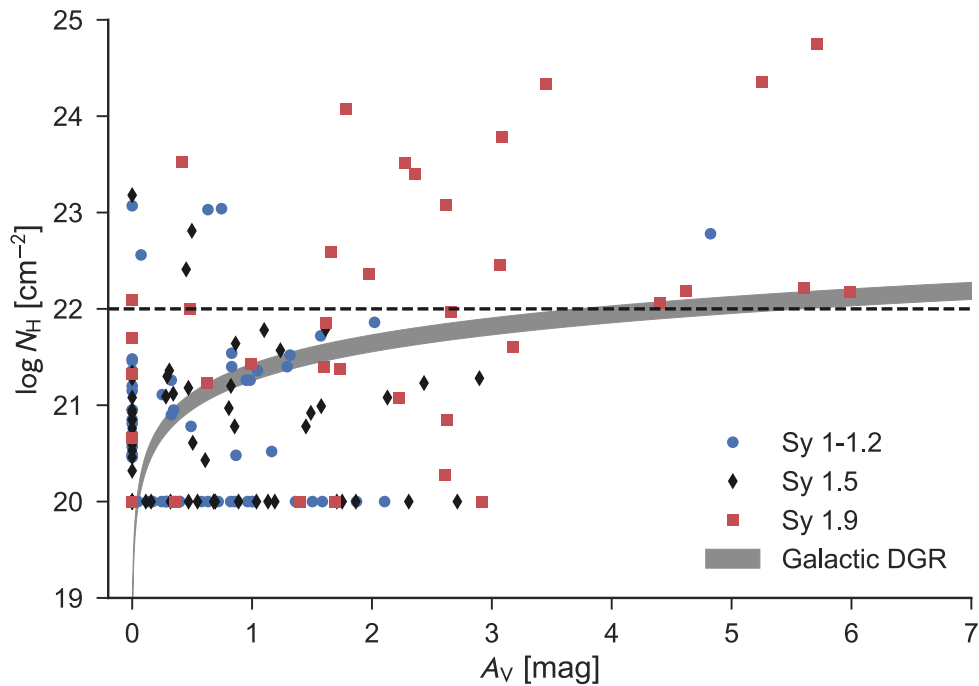


Figure 5.2: X-ray absorbing column density (N_{H}) vs optical extinction (A_V) for Sy1 - 1.9 AGN in the BASS survey, taken from Shimizu et al. (2018). The gray shaded line corresponds to the expected relation for Galactic dust-to-gas ratios. The black dashed line indicates the dividing line between X-ray obscured and unobscured AGN.

would be detected for the narrow lines due to dilution of the polarized continuum by the narrow line photons (Schmid et al., 2003). Measurements of the position angle of polarized light can also reveal the orientation of the torus in these AGN, thereby placing constraints on inclination and torus geometry.

While there have been extensive polarization studies of Seyfert 2 galaxies, showing the appearance of hidden broad lines in polarized light (e.g., Miller & Goodrich, 1990; Tran et al., 1992; Moran et al., 2000; Lumsden et al., 2004; Ramos Almeida et al., 2016), spectropolarimetry of Seyfert 1 galaxies has been limited. Furthermore, such polarimetry studies have predominantly been focused on optical polarimetry; near-IR polarimetry of AGN has been incredibly limited, with only a handful of Seyfert 2 galaxies observed with near-IR spectropolarimeters (Young et al., 1996; Watanabe et al., 2003). To date, near-IR spectropolarimetry of Type 1 AGN has not been reported in the literature. This has motivated the development of my own observing program at Palomar Observatory using the WIRC+Pol instrument

Table 5.1: List of X-ray obscured Type 1 AGN observed with the WIRC+Pol near-IR spectropolarimeter (J and H bands) at Palomar Observatory during 2019–2020. These exposure times do not include reference star exposures or overheads.

Object	RA (J2000)	Dec (J2000)	<i>J</i> Mag	<i>H</i> Mag	<i>J</i> exp (mins)	<i>H</i> exp (mins)
KUG1208+386	12h 10m 44.3s	+38d 20m 10.3s	12.156	11.45	24	24
2MASXJ22041914+0333511	22h 04m 19.2s	+03d 33m 51.3s	13.253	12.314	89	55
Mrk 376	07h 14m 15.1s	+45d 41m 55.9s	12.71	11.724	55	30
MCG+04-06-043	02h 26m 54.6s	+23d 47m 58.8s	12.277	11.523	30	20
Mrk 975	01h 13m 51.0s	+13d 16m 18.2s	12.182	11.583	30	24
CGCG031-072	08h 14m 25.3s	+04d 20m 32.8s	12.289	11.189	30	15
2MASXJ18305065+0928414	18h 30m 50.6s	+09d 28m 41.9s	11.208	10.501	8	8
MCG-01-30-041	11h 52m 38.2s	-5d 12m 25.3s	11.706	10.918	20	12

(Tinyanont et al., 2019), which is a near-IR spectropolarimeter operating in the J and H wavelength bands. WIRC+Pol observations have been completed for our sources from the BASS sample that have prominent, broad $H\alpha$ and $H\beta$ lines (Sy1 - 1.2) with column densities $N_{\text{H}} \gtrsim 10^{23} \text{ cm}^{-2}$, that are visible from the Palomar Observatory. Table 5.1 lists the sources observed under this WIRC+Pol program. Data reduction with the currently developed WIRC+Pol pipeline and preliminary analysis is ongoing.

Probing the near-IR properties of these enigmatic X-ray obscured Type 1 AGN may help elucidate whether the mismatching classifications can also be linked to dust properties in the host galaxies of these sources. We aim to also utilize multi-wavelength information, namely the IR through X-ray SEDs of these objects, in order to investigate whether there are unusual features in the SED that are possibly linked to the conflicting X-ray and optical classifications. For example, Hogg et al. (2012) found that the SED of one of the sources in our sample, 2MASXJ19301380+3410495, shows it to be very red. This is another unusual property not generally observed in *Swift*/BAT AGN as a whole and may be connected to the X-ray/optical mismatch, if seen in other X-ray obscured Type 1 sources. In general, the study of such exotic AGN with conflicting X-ray and optical classifications will lead to important insights into the geometry of the circumnuclear material and test the validity of unified models of AGN.

5.3 Future X-ray Missions and Prospects for Studies of AGN Coronae

Pivotal to the advancement of studies of AGN in the X-ray band is the development of new X-ray instruments and missions with greater broadband coverage and higher energy resolution. The *X-ray Imaging and Spectroscopy Mission* (XRISM Science Team, 2020), expected to be launched in the next year, will offer unprecedented spectral resolution in the soft X-ray band (7 eV FWHM) through microcalorimeter technology. With a substantially increased collecting area and spectral resolution that is 20-40 times greater than the CCD instruments aboard current soft X-ray missions such as *Chandra* and *XMM-Newton*, *XRISM* will greatly improve our understanding of AGN structure. The Fe K α line is a key diagnostic of the circumnuclear environment, and detailed characterization of its line profile will enable acquisition of information such as distance from the SMBH and precise measurements of black hole spin. Particularly relevant to extensions of this thesis work are studies of fluorescent emission lines in soft X-ray spectra from various elements such as O, Mg, Si, and S. High resolution X-ray spectroscopy will enable such lines to be detected and characterized, which has been presently incredibly difficult due to limitations in the energy resolution of current X-ray grating spectrometers (see Figure 5.3). Examination of these soft X-ray line profiles can reveal whether material is outflowing, which is not only important in the context of AGN feedback, but can also explain mismatches between X-ray and optical classifications. For example, the broad-line radio galaxy 3C 445 is classified as Type 1 from its optical spectrum, however *Suzaku* and *Chandra* observations show 3C 445 to be heavily X-ray absorbed and the soft X-ray spectrum is dominated by ionized emission lines (Braiton et al., 2011). High resolution spectroscopy is generally needed to confirm strong emission associated with a high column density of outflowing gas.

While the launch of *NuSTAR* has catapulted the ability to study AGN coronal temperatures more robustly, much is still unknown about the nature and origin of the corona. Constraints on the geometry, size and location of the corona remain difficult to obtain, as they rely on methods such as X-ray reverberation mapping and relativistic reflection modeling. These methods require very long observations of bright AGN in order to monitor for changes in continuum flux and the corresponding reverberation lag it produces. In addition, testing general relativistic ray-tracing models for different coronal geometries and applying advanced relativistic reflection models requires very high signal-to-noise data, thereby limiting observations to the brightest AGN.

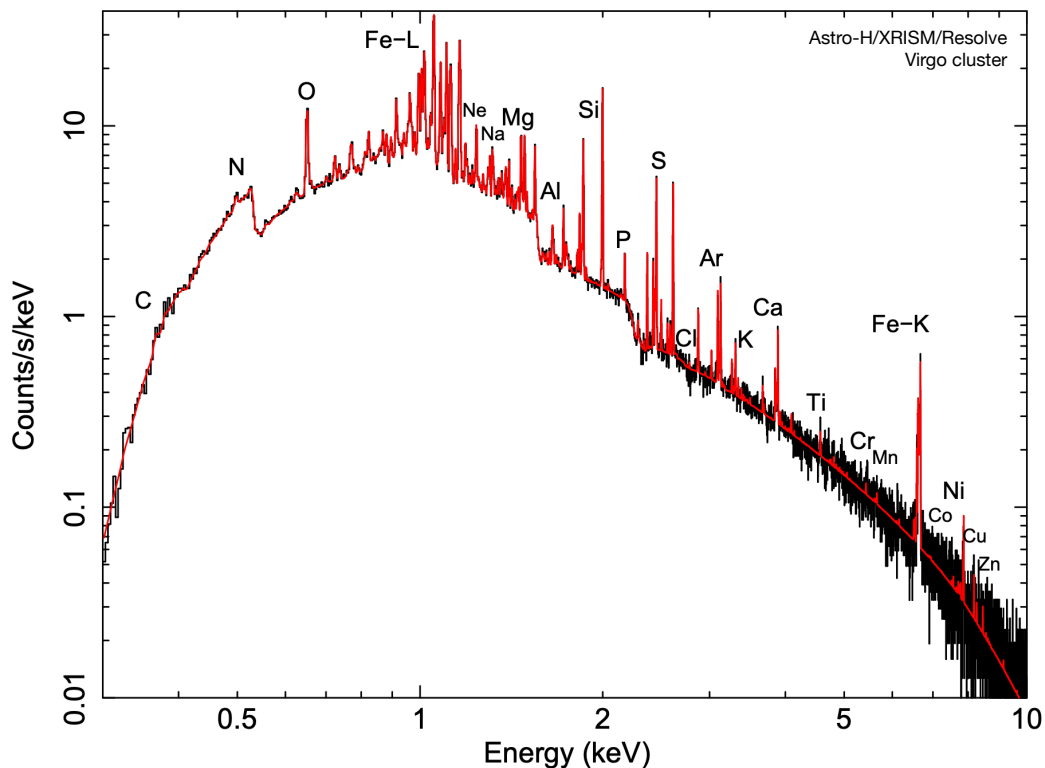


Figure 5.3: Simulated *XRISM* spectrum of the core of M87 for a 100 ks exposure, where data is shown in black and best-fit model in red. Figure taken from Kitayama et al. (2014).

Another promising technique to study the corona is X-ray polarimetry. While X-ray polarimetry has remained mostly unexplored in the past few decades, mainly due to the lack of sensitive polarization detectors, a new dedicated polarimetry mission has been approved for launch in the next year. The *Imaging X-ray Polarimetry Explorer* (IXPE, Weisskopf et al. 2016) will have imaging, timing and energy-resolved polarimetry capabilities in the 2–8 keV band, thereby opening studies of the polarimetric properties of AGN coronae. X-ray polarimetry can be a powerful tool to probe the geometry of the coronal plasma and possibly even the magnetic field that permeates it.

The likely hybrid nature of the coronal plasma brings to question the fraction of non-thermal particles present. Whether the corona is a hybridized system containing a non-thermal electron population can be tested through observation of a hard, non-thermal tail in the X-ray spectrum and an annihilation line at 511 keV (e.g., Lubiński

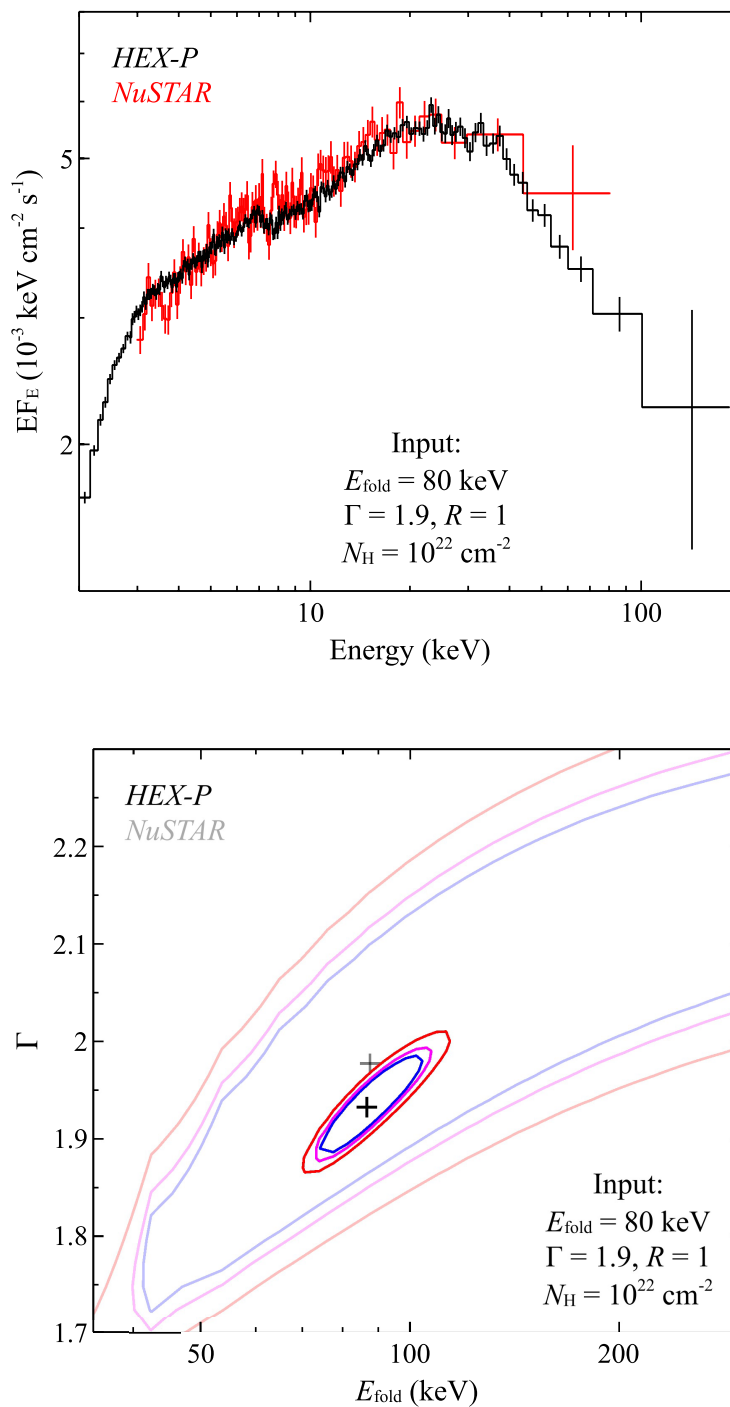


Figure 5.4: *Top*: Simulated *HEX-P* spectrum of a typical AGN with a 2–10 keV luminosity of $10^{-11} \text{ erg s}^{-1} \text{ cm}^{-2}$, compared against a *NuSTAR* spectrum of the same source. *Bottom*: Simulated *HEX-P* contour plot of the same AGN in the Γ – E_{cut} plane, compared against *NuSTAR*. Figure credit: Kristin K. Madsen (2020).

et al., 2010; Siegert et al., 2016). In order to elucidate the full nature of the corona and robustly test hybrid plasma models, next-generation hard X-ray observatories with high sensitivity at energies beyond 100 keV will be essential. One such concept broadband X-ray instrument is the *High-Energy X-ray Probe* (HEX-P, Madsen et al. 2019). The *HEX-P* mission proposes to provide broadband hard X-ray spectral coverage up to 200 keV with over 40 times the energy sensitivity of any previous mission in the 10–80 keV band. Currently, coronal temperature measurements made using *NuSTAR* are based on subtle downturns in continuum spectra near ~ 50 keV, which are used to infer cutoff energies that may exceed 100 keV. With its wide bandpass and large collecting area, *HEX-P* will not only be able to detect many more AGN in the hard X-ray band, but also measure coronal temperatures with unprecedented precision (see Figure 5.4). As a successor to *NuSTAR*, and currently the only concept X-ray mission to provide high energy X-ray focusing capabilities above 100 keV, *HEX-P* would lead to ground-breaking advances in our understanding of the corona.

Chapter 6

SUMMARY AND CONCLUSIONS

This thesis work has focused on elucidating the properties of the enigmatic corona in AGN, which acts as the powerhouse driving the luminous X-ray emission we observe from these objects. A critical tool used in my thesis research to achieve this goal is broadband X-ray spectroscopy. This work particularly draws on X-ray data taken with the *NuSTAR* telescope, which has transformed studies of AGN coronae. With its unique focusing capabilities at hard X-ray energies, *NuSTAR* has provided broadband X-ray spectra for large samples of AGN with unprecedented energy sensitivity above 10 keV. This has allowed significant progress to be made in understanding key properties of the corona and the structure of the circumnuclear material in AGN.

In the first study of this thesis (presented in Chapter 2), I examined coronal high-energy cutoffs in a sample of 46 Seyfert 1 AGN selected from the *Swift*/BAT hard X-ray all-sky survey. I performed spectral modeling of short, ~ 20 ks *NuSTAR* observations of each source using simple phenomenological models. From fitting the *NuSTAR* spectra, I obtained constraints on the coronal cutoff energy, which I used to map out the compactness-temperature plane for all AGN in my sample. My findings showed AGN to be clustered near the boundary for runaway pair production, indicating that annihilation and pair production act to regulate the temperature of the corona. Some AGN in the sample are located far away from the pair lines and thus likely possess low coronal temperatures, which has important implications for the possible cooling mechanisms within the corona. Low coronal temperatures are not typically found in a fully thermal plasma, suggesting that the corona may be hybridized in nature, composed of a mixture of thermal and non-thermal particles.

From the sample used in my first paper, I had identified a source with a very low coronal temperature from fitting spectra of the short ~ 20 ks *NuSTAR* exposure. A longer ~ 50 ks follow-up *NuSTAR* observation was completed of this source, and I performed a detailed broadband X-ray spectral analysis of the source using multi-epoch soft X-ray data taken with *Swift*/XRT and *XMM-Newton* in addition to the two *NuSTAR* observations. This work is described in Chapter 3. I found that the source was unusual not only for its low coronal temperature, but also showed strong

X-ray obscuration ($N_{\text{H}} > 10^{23} \text{ cm}^{-2}$) across all epochs, despite being classified as an optically unobscured Type 1 AGN. In addition to the X-ray data, I investigated the multi-wavelength properties of this source in order to understand the mismatch between X-ray and optical classifications. From comparing the ratio of reddening to X-ray absorbing column density (E_{B-V}/N_{H}), I found that the source has a much lower dust-to-gas ratio relative to the Galactic ISM, strongly suggesting that the Broad Line Region itself provides the source of extra X-ray obscuration, being composed of dust-free gas that forms an inner extension of the dusty molecular torus.

In the final part of my thesis, which is presented in Chapter 5, I undertook a detailed systematic study of 195 *NuSTAR* observations of Seyfert 1 AGN selected from the *Swift*/BAT survey. This work presents the first systematic study of the coronal properties of one of the largest samples of unobscured AGN with high quality broadband X-ray data. I included complementary simultaneous soft X-ray data taken with *Swift*/XRT or *XMM-Newton* in order to robustly model the X-ray spectra. I modeled the broadband spectra of each observation using several different spectral models, including more advanced reflection models that more accurately characterize the coronal emission compared to previous studies. In addition to obtaining more robust constraints on the temperature of the corona for a large sample of AGN, I also explored possible relations between coronal parameters and fundamental SMBH accretion properties. Contrary to some studies presented in literature for samples of AGN observed with pre-*NuSTAR* data, I do not find evidence for a strong correlation between the coronal high energy cutoff and accretion parameters such as the Eddington ratio and black hole mass. I also do not find a statistically significant correlation between the X-ray photon index, Γ , and Eddington ratio. This calls into question the robustness of such correlations previously reported in the literature and thus one should proceed with caution in the usage of such relations for deriving properties of accreting SMBH systems.

Looking towards the future, there is much promise for deeper studies of AGN coronae with the prospect of next generation X-ray observatories such as *HEXP* being launched, providing highly sensitive broadband X-ray coverage beyond the bandpass of *NuSTAR*. The corona is an incredibly important yet enigmatic component of luminous accreting black hole systems, and our understanding of its nature will continue to grow and evolve over time.

Bibliography

- Akylas, A., & Georgantopoulos, I. 2021, A&A, arXiv:2108.11337
- Ananna, T. T., Treister, E., Urry, C. M., et al. 2019, ApJ, 871, 240
- Antonucci, R. 1993, A&A, 31, 473
- Antonucci, R. R. J., & Miller, J. S. 1985, ApJ, 297, 621
- Aretxaga, I., Joguet, B., Kunth, D., Melnick, J., & Terlevich, R. J. 1999, ApJL, 519, L123
- Arnaud, K. 1996, in ASP Conf. Series, Vol. 101, Astronomical Data Analysis Software and Systems, ed. G. H. Jacoby & J. Barnes, 17
- Assef, R. J., Kochanek, C. S., Brodwin, M., et al. 2010, ApJ, 713, 970
- Astropy Collaboration, Robitaille, T. P., Tollerud, E. J., et al. 2013, A&A, 558, A33
- Astropy Collaboration, Price-Whelan, A. M., Sipőcz, B. M., et al. 2018, AJ, 156, 123
- Awaki, H., Koyama, K., Inoue, H., & Halpern, J. P. 1991, PASJ, 43, 195
- Ballantyne, D. R., Ross, R. R., & Fabian, A. C. 2002, MNRAS, 336, 867
- Ballantyne, D. R., Bollenbacher, J. M., Brenneman, L. W., et al. 2014, ApJ, 794, 62
- Baloković, M., Comastri, A., Harrison, F. A., et al. 2014, ApJ, 794, 111
- Baloković, M., Matt, G., Harrison, F. A., et al. 2015, ApJ, 800, 62
- Baloković, M., Brightman, M., Harrison, F. A., et al. 2018, ApJ, 854, 42
- Baloković, M., Harrison, F. A., Madejski, G., et al. 2020, ApJ, 905, 41
- Barcons, X., Nandra, K., Barret, D., et al. 2015, in Journal of Physics Conference Series, Vol. 610, Journal of Physics Conference Series, 012008
- Baumgartner, W. H., Tueller, J., Markwardt, C. B., et al. 2013, ApJS, 207, 19
- Beckmann, V., Soldi, S., Ricci, C., et al. 2009, A&A, 505, 417
- Braito, V., Reeves, J. N., Sambruna, R. M., & Gofford, J. 2011, MNRAS, 414, 2739
- Brandt, W. N., Mathur, S., & Elvis, M. 1997, MNRAS, 285, L25
- Brenneman, L. W., Madejski, G., Fuerst, F., et al. 2014, ApJ, 781, 83
- Brightman, M., & Nandra, K. 2011, MNRAS, 413, 1206
- Brightman, M., Silverman, J. D., Mainieri, V., et al. 2013, MNRAS, 433, 2485

- Bruzual, G., & Charlot, S. 2003, MNRAS, 344, 1000
- Burbidge, E. M., Burbidge, G. R., & Prendergast, K. H. 1959, ApJ, 130, 26
- Burrows, D. N., Hill, J. E., Nousek, J. A., et al. 2005, Space Sci. Rev., 120, 165
- Burtscher, L., Meisenheimer, K., Tristram, K. R. W., et al. 2013, A&A, 558, A149
- Cash, W. 1979, ApJ, 228, 939
- Chartas, G., Rhea, C., Kochanek, C., et al. 2016, Astronomische Nachrichten, 337, 356
- Dadina, M. 2007, A&A, 461, 1209
- Davies, R. I., Burtscher, L., Rosario, D., et al. 2015, ApJ, 806, 127
- De Marco, B., Ponti, G., Cappi, M., et al. 2013, MNRAS, 431, 2441
- Edge, D. O., Shakeshaft, J. R., McAdam, W. B., Baldwin, J. E., & Archer, S. 1959, Mem. R. Astron. Soc., 68, 37
- Elitzur, M., & Ho, L. C. 2009, ApJL, 701, L91
- Elvis, M., Maccacaro, T., Wilson, A. S., et al. 1978, MNRAS, 183, 129
- Emmanoulopoulos, D., Papadakis, I. E., Dovčiak, M., & McHardy, I. M. 2014, MNRAS, 439, 3931
- Evans, I. N., Ford, H. C., Kinney, A. L., et al. 1991, ApJL, 369, L27
- Evans, P. A., Beardmore, A. P., Page, K. L., et al. 2009, MNRAS, 397, 1177
- Fabian, A. C. 1994, ApJS, 92, 555
- Fabian, A. C., Celotti, A., & Erlund, M. C. 2006, MNRAS, 373, L16
- Fabian, A. C., Lohfink, A., Belmont, R., Malzac, J., & Coppi, P. 2017, MNRAS, 467, 2566
- Fabian, A. C., Lohfink, A., Kara, E., et al. 2015, MNRAS, 451, 4375
- Fabian, A. C., Rees, M. J., Stella, L., & White, N. E. 1989, MNRAS, 238, 729
- Fabian, A. C., Zoghbi, A., Ross, R. R., et al. 2009, Nature, 459, 540
- Fiore, F., Puccetti, S., Brusa, M., et al. 2009, ApJ, 693, 447
- Fürst, F., Müller, C., Madsen, K. K., et al. 2016, ApJ, 819, 150
- Gabriel, C., Denby, M., Fyfe, D. J., et al. 2004, in Astronomical Society of the Pacific Conference Series, Vol. 314, Astronomical Data Analysis Software and Systems (ADASS) XIII, ed. F. Ochsenbein, M. G. Allen, & D. Egret, 759

- Gandhi, P., Hönig, S. F., & Kishimoto, M. 2015, *ApJ*, 812, 113
- Gandhi, P., Horst, H., Smette, A., et al. 2009, *A&A*, 502, 457
- García, J., & Kallman, T. R. 2010, *ApJ*, 718, 695
- García, J., Dauser, T., Lohfink, A., et al. 2014, *ApJ*, 782, 76
- García, J. A., Dauser, T., Steiner, J. F., et al. 2015, *ApJL*, 808, L37
- García, J. A., Kara, E., Walton, D., et al. 2019, *ApJ*, 871, 88
- Gehrels, N., Chincarini, G., Giommi, P., et al. 2004, *ApJ*, 611, 1005
- Ghisellini, G., Haardt, F., & Fabian, A. C. 1993, *MNRAS*, 263
- Giacconi, R., Gursky, H., Paolini, F. R., & Rossi, B. B. 1962, *Phys. Rev. Letters*, 9, 439
- Gilli, R., Comastri, A., & Hasinger, G. 2007, *A&A*, 463, 79
- Greene, J. E., & Ho, L. C. 2007, *ApJ*, 670, 92
- Guilbert, P. W., Fabian, A. C., & Rees, M. J. 1983, *MNRAS*, 205, 593
- Haardt, F., & Maraschi, L. 1993, *ApJ*, 413, 507
- Harrison, F. A., Craig, W. W., Christensen, F. E., et al. 2013, *ApJ*, 770, 103
- Hinkle, J. T., & Mushotzky, R. 2021, *MNRAS*, 506, 4960
- Hogg, J. D., Winter, L. M., Mushotzky, R. F., Reynolds, C. S., & Trippe, M. 2012, *ApJ*, 752, 153
- Hopkins, P. F., & Elvis, M. 2010, *MNRAS*, 401, 7
- Jansen, F., Lumb, D., Altieri, B., et al. 2001, *A&A*, 365, L1
- Kaastra, J. S. 2017, *A&A*, 605, A51
- Kalberla, P. M. W., Burton, W. B., Hartmann, D., et al. 2005, *A&A*, 440, 775
- Kamraj, N., Harrison, F. A., Baloković, M., Lohfink, A., & Brightman, M. 2018, *ApJ*, 866, 124
- Kamraj, N., Baloković, M., Brightman, M., et al. 2019, *ApJ*, 887, 255
- Kamraj, N., Harrison, F. A., Brightman, M., et al. 2021
- Kara, E., Fabian, A. C., Cackett, E. M., Miniutti, G., & Uttley, P. 2013, *MNRAS*, 430, 1408
- Kara, E., García, J. A., Lohfink, A., et al. 2017, *MNRAS*, 468, 3489

- Kitayama, T., Bautz, M., Markevitch, M., et al. 2014, arXiv e-prints, arXiv:1412.1176
- Kormendy, J., & Ho, L. C. 2013, *ARA&A*, 51, 511
- Koss, M., Trakhtenbrot, B., Ricci, C., et al. 2017, *ApJ*, 850, 74
- Krolik, J. H., & Begelman, M. C. 1988a, *ApJ*, 329, 702
- . 1988b, *ApJ*, 329, 702
- Landi, R., Masetti, N., Morelli, L., et al. 2007, *ApJ*, 669, 109
- López-Gonzaga, N., Burtscher, L., Tristram, K. R. W., Meisenheimer, K., & Schartmann, M. 2016, *A&A*, 591, A47
- Lubiński, P., Zdziarski, A. A., Walter, R., et al. 2010, *MNRAS*, 408, 1851
- Lumsden, S. L., Alexander, D. M., & Hough, J. H. 2004, *MNRAS*, 348, 1451
- Lusso, E., & Risaliti, G. 2016, *ApJ*, 819, 154
- Lusso, E., Comastri, A., Vignali, C., et al. 2010, *A&A*, 512, A34
- Lusso, E., Hennawi, J. F., Comastri, A., et al. 2013, *ApJ*, 777, 86
- Lutz, D., Maiolino, R., Spoon, H. W. W., & Moorwood, A. F. M. 2015, *A&A*, 418, 465
- Madsen, K., Hickox, R., Bachetti, M., et al. 2019, in *Bulletin of the American Astronomical Society*, Vol. 51, 166
- Madsen, K. K., Harrison, F. A., Markwardt, C. B., et al. 2015, *ApJ*, 220, 8
- Madsen, K. K., Harrison, F., Broadway, D., et al. 2018, in *Society of Photo-Optical Instrumentation Engineers (SPIE) Conference Series*, Vol. 10699, *Space Telescopes and Instrumentation 2018: Ultraviolet to Gamma Ray*, ed. J.-W. A. den Herder, S. Nikzad, & K. Nakazawa
- Magdziarz, P., & Zdziarski, A. A. 1995, *MNRAS*, 273, 837
- Maiolino, R., Marconi, A., Salvati, M., et al. 2001, *A&A*, 365, 28
- Malizia, A., Molina, M., Bassani, L., et al. 2014, *ApJL*, 782, L25
- Marinucci, A., Matt, G., Miniutti, G., et al. 2014, *ApJ*, 787, 83
- Marinucci, A., Bianchi, S., Matt, G., et al. 2016, *MNRAS*, 456, L94
- Massaro, E., Giommi, P., Leto, C., et al. 2009, *A&A*, 495, 691
- Matt, G., Baloković, M., Marinucci, A., et al. 2015, *MNRAS*, 447, 3029

- McHardy, I. M., Gunn, K. F., Uttley, P., & Goad, M. R. 2005, *MNRAS*, 359, 1469
- Merloni, A., & Fabian, A. C. 2001, *MNRAS*, 321, 549
- Merloni, A., Bongiorno, A., Brusa, M., et al. 2014, *MNRAS*, 437, 3550
- Miller, J. S., & Goodrich, R. W. 1990, *ApJ*, 355, 456
- Molina, M., Malizia, A., Bassani, L., et al. 2019, *MNRAS*, 484, 2735
- Moran, E. C., Barth, A. J., Kay, L. E., & Filippenko, A. V. 2000, *ApJ*, 540, L73
- Murphy, K. D., & Yaqoob, T. 2009, *MNRAS*, 397, 1549
- Nicastro, F., Piro, L., De Rosa, A., et al. 2000, *ApJ*, 536, 718
- Niedźwiecki, A., Szanecki, M., & Zdziarski, A. A. 2019, *MNRAS*, 485, 2942
- Oh, K., Sarzi, M., Schawinski, K., & Yi, S. K. 2011, *ApJS*, 195, 13
- Oh, K., Yi, S. K., Schawinski, K., et al. 2015, *ApJS*, 219, 1
- Oh, K., Koss, M., Markwardt, C. B., et al. 2018, *ApJS*, 235, 4
- Osterbrock, D. E. 1978, *Proceedings of the National Academy of Science*, 75, 540
- . 1981, *ApJ*, 249, 462
- Packham, C., Radomski, J. T., Roche, P. F., et al. 2005, *ApJ*, 618, L17
- Panessa, F., & Bassani, L. 2002, *A&A*, 394, 435
- Panessa, F., Bassani, L., Cappi, M., et al. 2006, *A&A*, 455, 173
- Perri, M., Puccetti, S., Spagnuolo, N., et al. 2017, *The NuSTAR Data Analysis Software Guide v1.7*
- Petrucci, P. O., Haardt, F., Maraschi, L., et al. 2001, *ApJ*, 556, 716
- Piconcelli, E., Bianchi, S., Guainazzi, M., Fiore, F., & Chiaberge, M. 2007, *A&A*, 466, 855
- Pounds, K. A., Done, C., & Osborne, J. P. 1995, *MNRAS*, 277, L5
- Poutanen, J., & Svensson, R. 1996, *ApJ*, 470, 249
- Ramos Almeida, C., Martínez González, M. J., Asensio Ramos, A., et al. 2016, *MNRAS*, 461, 1387
- Ramos Almeida, C., & Ricci, C. 2017, *Nature Astronomy*, 1, 679
- Ricci, C., Paltani, S., Ueda, Y., & Awaki, H. 2013, *MNRAS*, 435, 1840

- Ricci, C., Walter, R., Courvoisier, T. J. L., & Paltani, S. 2011, *A&A*, 532, A102
- Ricci, C., Trakhtenbrot, B., Koss, M. J., et al. 2017a, *Nature*, 549, 488
- . 2017b, *ApJS*, 233, 17
- Ricci, C., Ho, L. C., Fabian, A. C., et al. 2018, *MNRAS*, 480, 1819
- Risaliti, G., & Elvis, M. 2004, in *Supermassive Black Holes in the Distant Universe*, ed. A. J. Barger, Vol. 308, 187
- Risaliti, G., Elvis, M., Fabbiano, G., Baldi, A., & Zezas, A. 2005, *ApJL*, 623, L93
- Rothschild, R. E., Mushotzky, F. R., Baity, W. A., et al. 1983, *ApJ*, 269, 423
- Rybicki, G. B., & Lightman, A. P. 1979, *Radiative processes in astrophysics* (Wiley-Interscience, New York)
- Salpeter, E. E. 1964, *ApJ*, 140
- Sánchez, S. F., García-Lorenzo, B., Jahnke, K., et al. 2006, *Astronomische Nachrichten*, 327, 167
- Sandage, A. 1965, *ApJ*, 141, 1560
- Schmid, H. M., Appenzeller, I., & Burch, U. 2003, *A&A*, 404, 505
- Schmidt, M. 1963, *Nature*, 197, 1040
- Seyfert, C. K. 1943, *ApJ*, 97, 28
- Shakura, N. I., & Sunyaev, R. A. 1973, *A&A*, 500, 33
- Shemmer, O., Brandt, W. N., Netzer, H., Maiolino, R., & Kaspi, S. 2006, *ApJL*, 646, L29
- . 2008, *ApJ*, 682, 81
- Shimizu, T. T., Davies, R. I., Koss, M., et al. 2018, *ApJ*, 856, 154
- Siegert, T., Diehl, R., Vincent, A. C., et al. 2016, *A&A*, 595, A25
- Sobolewska, M. A., & Papadakis, I. E. 2009, *MNRAS*, 399, 1597
- Stalevski, M., Ricci, C., Ueda, Y., et al. 2016, *MNRAS*, 458, 2288
- Stern, B. E., Poutanen, J., Svensson, R., Sikora, M., & Begelman, M. C. 1995, *ApJL*, 449, L13
- Stern, D. 2015, *ApJ*, 807, 129
- Storchi-Bergmann, T., Wilson, A. S., & Baldwin, J. A. 1992, *ApJ*, 396, 45

- Strüder, L., Briel, U., Dennerl, K., et al. 2001, *A&A*, 365, L18
- Svensson, R. 1982, *ApJ*, 258, 335
- . 1984, *MNRAS*, 209, 175
- Tinyanont, S., Millar-Blanchaer, M. A., Nilsson, R., et al. 2019, *Publications of the Astronomical Society of the Pacific*, 131, 025001
- Titarchuk, L. 1994, *ApJ*, 434, 570
- Titarchuk, L., & Lyubarskij, Y. 1995, *ApJ*, 450, 876
- Tombesi, F., Cappi, M., Reeves, J. N., & Braito, V. 2012, *MNRAS*, 422, L1
- Tortosa, A., Bianchi, S., Marinucci, A., Matt, G., & Petrucci, P. O. 2018, *A&A*, 614, A37
- Tortosa, A., Marinucci, A., Matt, G., et al. 2017, *MNRAS*, 466, 4193
- Trakhtenbrot, B., Ricci, C., Koss, M. J., et al. 2017, *MNRAS*, 470, 800
- Tran, H. D., Lyke, J. E., & Mader, J. A. 2011, *ApJ*, 726, L21
- Tran, H. D., Miller, J. S., & Kay, L. E. 1992, *ApJ*, 397, 452
- Treister, E., Krolik, J. H., & Dullemond, C. 2008, *ApJ*, 679, 140
- Trippe, M. L., Reynolds, C. S., Koss, M., Mushotzky, R. F., & Winter, L. M. 2011, *ApJ*, 736, 81
- Tristram, K. R. W., Meisenheimer, K., Jaffe, W., et al. 2007, *A&A*, 474, 837
- Turner, M. J. L., Abbey, A., Arnaud, M., et al. 2001, *A&A*, 365, L27
- Ueda, Y., Akiyama, M., Hasinger, G., Miyaji, T., & Watson, M. G. 2014, *ApJ*, 786, 104
- Urry, C. M., & Padovani, P. 1995, *PASP*, 107, 83
- Uttley, P., Cackett, E. M., Fabian, A. C., Kara, E., & Wilkins, D. R. 2014, *Astronomy and Astrophysics Review*, 22, 72
- Vasudevan, R. V., & Fabian, A. C. 2009, *MNRAS*, 392, 1124
- Verner, D. A., Ferland, G. J., Korista, K. T., & Yakovlev, D. G. 1996, *ApJ*, 465, 487
- Walton, D. J., Tomsick, J. A., Madsen, K. K., et al. 2016, *ApJ*, 826, 87
- Watanabe, M., Nagata, T., Sato, S., Nakaya, H., & Hough, J. H. 2003, *ApJ*, 591, 714

- Weisskopf, M. C., Ramsey, B., O'Dell, S., et al. 2016, in Society of Photo-Optical Instrumentation Engineers (SPIE) Conference Series, Vol. 9905, Space Telescopes and Instrumentation 2016: Ultraviolet to Gamma Ray, ed. J.-W. A. den Herder, T. Takahashi, & M. Bautz, 990517
- Wilms, J., Allen, A., & McCray, R. 2000, *ApJ*, 542, 914
- Wilms, J., Allen, A., & McCray, R. 2000, *ApJ*, 542, 914
- Winter, L. M., Lewis, K. T., Koss, M., et al. 2010, *ApJ*, 710, 503
- XRISM Science Team. 2020, arXiv e-prints, arXiv:2003.04962
- Xu, Y., Baloković, M., Walton, D. J., et al. 2017, *ApJ*, 837, 21
- Yang, Q.-X., Xie, F.-G., Yuan, F., et al. 2015, *MNRAS*, 447, 1692
- Young, S., Hough, J. H., Axon, D. J., Ward, M. J., & Bailey, J. A. 1996, *MNRAS*, 280, 291
- Zdziarski, A. A. 1985, *ApJ*, 289, 514
- Zdziarski, A. A., Johnson, W. N., & Magdziarz, P. 1996, *MNRAS*, 283, 193
- Zdziarski, A. A., Poutanen, J., & Johnson, W. N. 2000, *ApJ*, 542, 703
- Zdziarski, A. A., Zycki, P. T., & Krolik, J. H. 1993, *ApJL*, 414, L81
- Zdziarski, A. A., Jourdain, E., Lubiński, P., et al. 2021, *ApJL*, 914, L5
- Zel'dovich, Y. B. 1964, *Soviet Physics Doklady*, 9, 195
- Zensus, J. A., Unwin, S. C., Cohen, M. H., & Biretta, J. A. 1990, *AJ*, 100, 1777